Teleconnection between Northern Polar Climate and South Asian Monsoon during Mid Pliocene Warm Period and since Late Quaternary

A THESIS SUBMITTED IN PARTIAL FULFILMENT FOR THE DEGREE OF

DOCTOR OF PHILOSOPHY

IN THE SCHOOL OF EARTH, OCEAN AND ATMOSPHERIC SCIENCES

GOA UNIVERSITY

By

Padmasini Behera

School of Earth, Ocean and Atmospheric Sciences
Goa University
Taleigao Plateau, Goa, India-403206

April 2022

DECLARATION

I, Padmasini Behera hereby declare that this thesis represents work which has been carried out by me and that it has not been submitted, either in part or full, to any other University or Institution for the award of any research degree.

Padmasini Behera

Place: Goa University
Date: 25-04-2022

Padmasini Behera

CERTIFICATE

I hereby certify that the above Declaration of the candidate, Padmasini Behera is true and the work was carried out under my supervision.

Manish Tiwari

Dr. Manish Tiwari
Scientist-F and Incharge (Paleoceanography Section)
National Centre for Polar and Ocean Research
Vasco da Gama, Goa, India

Acknowledgement

The last five years has been a long journey for me. It was full of challenges, excitement and fun. I would like to acknowledge many people who have helped me immensely during this time. First of all, I would like to express my gratitude to my supervisor, Dr. Manish Tiwari, whose constant guidance, encouragement and support has been critical throughout. He has been instrumental in helping me to learn how to write good research papers. He has taught me with great patience.

I acknowledge the staff at the National Centre for Polar and Ocean Research for administrative and academic support and assistance. I also express my gratitude to Dr. Thamban Meloth (Group Director) and Dr. M Ravichandran (Secretary MoES) for their support and encouragement during this journey.

I am also grateful to the support of my DRC members Dr. Rajeev Saraswat, Prof. H.B Menon and Prof. V.M Matta who have given valuable feedback and ideas which further improved the thesis.

I would like to thank Vikash Kumar who guided me in many ways during this journey. His constant support and encouragement helped me to complete this work. I would like to thank Viola Rodrigues for staying by my side always. She was always there for any kind of support. On the same note I want to thank the other members of my lab and the Plaeoceanography division for their help in this journey.

I made many new friends here at NCPOR in the last five years, Nibedita, Pooja, Pallavi, Pinky, Rahul and Priyesh. I am grateful for having such a supportive friend circle that helped me in countless ways. They made this journey easier. I want to give my heartfelt thanks to them. I would like to specially thank my friend Jyoti, who was very patient and helpful during the difficult times.

As a last note, I convey my utmost regards to my family who were constant support at each and every step of my life.

Padmasini Behera

To

My Parents, Brothers, Sisters and niece

Contents

Abstract

The current global warming causes major changes in the high latitude climate including unprecedented reduction of sea ice extent (SIE) in the Arctic. The South Asian Monsoon (SoAM) precipitation is also projected to increase chiefly because of the atmosphere's enhanced moisture carrying capacity as per the latest IPCC report. A few short time series based studies have proposed a link between the Arctic SIE and south Asian monsoon; a reduction of the Arctic SIE is linked to the extreme precipitation events in central India. But such studies span only a few decades and hence are uncertain. To fully understand the connection between these two far-off regions in the current global warming scenario, we have to study the past periods with similar warmth and greenhouse gases concentrations. Late Pliocene including the Mid Pliocene Warm Period (MPWP; around 3 Ma, million years ago) is considered the nearest analogue to the modern climate with similar CO_2 concentration. Likewise, another important period of warmth was the last interglacial (Marine Isotope Stage 5e, ~125 kyr BP, thousand years before present). Previous paleoclimatic studies on teleconnection between northern high latitude climate and the SoAM variability mostly cover till last glacial period only (since 40 to 60 kyr BP). The present study goes beyond this and focuses on the teleconnection between these two regions during the MPWP (~ 3 Ma), last interglacial (~ 125 kyr BP), and the Holocene (last ~11.7 kyr).

To fill in the above gaps, the specific objectives of the study are (i) Reconstruction of paleoenvironmental condition during Mid Pliocene Warm Period at Atlantic-Arctic Gateway (Yermak Plateau), (ii) Reconstruction of high-resolution South Asian monsoon variability during Mid Pliocene Warm Period, (iii) Quantification of oceanic temperature and salinity from North Atlantic since Late Quaternary, (iv) Explore the possible links between northern high latitude climate change and South Asian monsoon system. To achieve these objectives, multiple isotopic and geochemical proxies were analysed in the present study. These include Total organic carbon (TOC) and total nitrogen (TN) content and isotopes ($\delta^{13}C$ and $\delta^{15}N$) of sedimentary organic matter, oxygen and carbon

isotopes ($\delta^{18}O$ and $\delta^{13}C$) of planktic and benthic foraminifera species. The quantification in terms of SST is carried out using trace element ratio (Mg/Ca) of planktic foraminifera. The findings from the present work are summarised below.

In the Arctic Ocean, sediment from the ODP Hole 910C near the Atlantic–Arctic Gateway region are used to reconstruct the water column stratification during the late Pliocene period including MPWP. The sea ice variability in the Arctic is studied by a few workers during this period, however little is known about the Arctic stratification, which is one of the major controlling factors for the sea ice melt. In this study, the Arctic stratification is reconstructed based on the surface relative nutrient utilization. It shows that the Arctic stratification is stronger during the warmer intervals of MPWP while weaker during the colder or glacial periods. The enhanced stratification during these warm intervals could be due to the enhancement of warm North Atlantic Current to the Arctic and the orbitally induced solar insolation, which increased the sea ice melt and river influx. The stronger stratification stores more heat and accelerates the sea ice melting.

The South Asian Monsoon variability is studied during the late Pliocene period. To reconstruct the SoAM variability during the late Pliocene, the sediment from the Site U1456 (IODP Expedition 355) from the eastern Arabian Sea were analyzed. This study presents a high-resolution record of SoAM variability during late Pliocene using surface productivity, denitrification, weathering and terrestrial influx. We found two distinct intervals of monsoon intensification - during MPWP, and at 2.9 Ma. The monsoon variability is the result of an interplay between thermodynamic and dynamic effects. The SoAM variability is further compared with the recently reconstructed sea ice extent in the Arctic during the late Pliocene. We find that lower (higher) Arctic SIE leads to stronger (weaker) SoAM during the late Pliocene via asymmetric interhemispheric energy export and through modulating jet stream flow and meridional circulation.

In the Atlantic Ocean, the sediment from the Lofoten Basin is analyzed to quantify the climate change during the two recent warm periods i.e., last interglacial and the Holocene. Due to the current global warming, the surface freshening at the Norwegian Sea affects the deep-water formation and the AMOC

strength. This study quantifies the surface hydrography in terms of SST and salinity anomalies, and the bottom water ventilation is observed from the carbon isotopes of benthic foraminifera. We find that during the last interglacial, the early warm (~6°C) and saline phase was disrupted by a cold event at around 124 kyr. This cold event is marked by the reduction of surface temperature (~3°C), surface salinity and the bottom water ventilation. It suggests the large influx of fresh water to the core site could have reduced the heat transport to the high latitude by declining the thermohaline circulation. During the early Holocene, the decrease in temperature (< 2°C), salinity and bottom water ventilation also represents the catastrophic freshwater release in to the Nordic Seas, which reduced the heat to the northern high latitude and lead to a major cooling event at ~8.6 kyr BP. The Holocene attains its thermal maxima at around 8 kyr BP and lasted up to 4kyr BP.

List of Figures

List of Tables

List of Publications from Thesis

1. **Padmasini Behera,** Manish Tiwari, Vikash Kumar, T. Sarathchandraprasad, and Shubham Tripathi. South Asian Monsoon variability and Arctic sea ice extent linkages during late Pliocene - a modern-like warm period. ***Paleoceanography and Paleoclimatology,*** 37(9), e2022PA004436, 2022.

2. **Padmasini Behera,** Manish Tiwari, and Jochen Knies. Enhanced Arctic stratification in a warming scenario: Evidence from the Mid Pliocene warm period. ***Paleoceanography and Paleoclimatology***, 36(6), e2020PA004182, 2021.

List of other Publications

3. T. Sarathchandraprasad, Manish Tiwari, and **Padmasini Behera**. South Asian Summer Monsoon precipitation variability during late Pliocene: Role of Indonesian Throughflow. ***Paleoceanography, Paleoclimatology, Paleoecology***, v 574, 2021.

4. Shubham Tripathi, **Padmasini Behera,** and Manish Tiwari. Evolution and dynamics of the denitrification in the Arabian Sea on millennial to million-year timescale. ***Current Science***, 119(2), 282, 2020.

5. Alexander Matul, Max S. Barash, Tatyana A. Khusid, **Padmasini Behera,** and Manish Tiwari. Paleoenvironment Variability during Termination I at the Reykjanes Ridge, North Atlantic. ***Geosciences***, 8(10), 375, 2018.

6. Manish Tiwari, Sidesh Nagoji, Vikash Kumar, Shubham Tripathi, and **Padmasini Behera.** Oxygen isotope-salinity relation in an Arctic fjord (Kongsfjorden): Implications to hydrographic variability. ***Geoscience Frontiers***, 9(6), 1937-1943, 2018.

Conferences in which the findings from the thesis research were presented

1. Oral presentation in 7th National conference of the Ocean Society of India (OSICON 2021) at NCPOR,Goa during 12-14 August **2021**. Presented "Denitrification record from Eastern Arabian Sea indicating South Asian Monsoon Variability during late Pliocene"

2. vPICO presentation in European Geosciences Union (EGU-2021) during 19-30 April **2021**. Presented "Monsoon variability during Mid Pliocene Warm Period: Evidence from Oceanic denitrification at eastern Arabian Sea"

3. Poster presentation in the National Conference on Polar Sciences (NCPS-2019) at NCPOR, Goa during 19-22 August **2019**. Presented "Relative nutrient Utilization indicates Atlantification at Atlantic –Arctic Gateway during Mid-Pliocene Warm Period "

4. Oral presentation in " National Seminar cum Workshop on Recent Advances in the Indian earth Science" held in Department of Geology, Kumaun University, Nainital, from 25th -26th March **2019**. Presented "Climatic Linkages between Arctic and Tropical Region during Mid-Pliocene Warm Period"

5. Poster presentation in the National Conference on Polar Sciences (NCPS-2017) in NCAOR, Goa during 16-17 May **2017**. Presented "A Quantitative Reconstruction of Large Scale Teleconnections between Arctic Climate and South Asian Monsoon System during Mid-Pliocene"

Chapter 1

Introduction

1.1 General Introduction

Earth's climatic system consists of various components such as ocean, atmosphere, cryosphere, land, and vegetation. The cryosphere is the frozen component of the earth's climate system. It includes seasonal snow, lake and river ice, sea ice, glaciers, the continental ice sheet, icebergs, permafrost, and seasonally frozen ground. The ice-albedo feedback is a key aspect of global climate change. In the polar regions, the decrease in snow and ice cover results in a decrease in surface albedo, and less reflection of the long-wave solar radiation, which further reduces the snow and ice area by increasing the temperature (Schneider et al., 1974; Kapsch et al., 2016). Recent observations revealed that the Arctic sea ice has declined at a rate of 12.4 % per decade from 1979 to 2012, which has resulted in the disappearance of nearly half of the sea ice coverage (Stroeve et al., 2011; IPCC 2013). It has been also projected that the Arctic Ocean will be sea ice-free by 2050 (Massonnet et al., 2012; Overland and Wang, 2007, 2013). The reduction of ice cover in the Arctic is aggravated by the Arctic amplification (higher temperature rise in the Arctic compared to lower latitudes) due to albedo, temperature, and energy transport related feedbacks. In addition to the ice-albedo effect, the influx of a large amount of freshwater by snow and ice melting, and rivers from the hinterland to the adjacent seas also adds to climate change. The freshwater influx causes enhanced stratification leading to the trapping of more heat in the surface layers that further melts the sea ice and thus generates positive feedback. The freshwater influx can also reduce heat transport to higher latitudes by slowing down the thermohaline circulation.

Oceans are another major component in the earth's climatic system, influencing the climate through their high heat capacity than the surrounding land and ability to transfer heat from one location to another. Based on the oceanic potential temperature and motion, the vertical structure is divided into three different zones; the mixed (surface) layer, the thermocline layer, and the deep ocean. The first two zones are found in the upper layer, while the third zone encompasses the intermediate, deep, and bottom layers. The surface currents within 100 m are wind driven, while the oceanic currents at depths greater than 1000 m are density driven, which is controlled by the temperature and salinity. Thus, thermohaline circulation (THC) is the global meridional overturning circulation associated with surface temperature and salinity gradient and involves the deep ocean. In high latitude regions, the surface water cools by releasing heat into the atmosphere, resulting in an increase in its density and a tendency for it to sink. The sea ice formation also helps in deep water formation through the process of brine rejection. It increases the salinity of the cold water beneath the ice and makes it denser, which sinks to the bottom. In the Atlantic, the differential solar heating between the high and low latitude region and the deep-water formation causes the water to move towards the pole. The current THC is responsible for much of the poleward oceanic heat transfer of about 1.2 ± 0.3 PW (1 PW = 1015 watts) (Ganachaud et al., 2000).

Another major part of the earth's climatic system is the atmospheric circulation. It encompasses all the physical processes including global and regional-scale circulations. It also includes the atmospheric convection, tropical, and extra-tropical cyclones, jet streams, and so on. The atmospheric circulation occurs mainly due to the formation of the pressure gradient in the atmosphere. Based on the pressure differences there are three different cells present in the troposphere i.e., the Hadley cell (tropical cell), Ferrell cell (subpolar cell), and the Polar cell. The pressure is low at the equator and high at the poles causing the air to move from the equator to the poles. Due to the Coriolis force, the westerly jets are formed (jet stream) at high altitude. These are the narrow bands of strong winds at the boundary between hot and cold air in the upper levels of the atmosphere. These jet streams are the major component of the atmospheric circulation causing extreme weather conditions at remote areas.

Since these climatic components are coupled, several teleconnection patterns are operating within the climate system. In the earth's general atmospheric circulation the tropics, mid-latitudes, and high latitudes are considered as separate components with distinct dynamics and sources of variability. However, the mutual interactions between these components are well studied on seasonal and longer time scales. These different components can be linked through the atmospheric and oceanic process in which the atmosphere acts like a bridge between different parts of the ocean and the ocean acts as a tunnel to different atmospheric regions (Liu & Alexander, 2007; Stan et al., 2017). Thus, teleconnection describes the climatic links between geographically separated regions. The atmospheric teleconnection acts via atmospheric circulation i.e., east-west overturning circulation (Walker circulation; Bjerknes, 1969) and north south overturning circulation (Hadley circulation). The heat associated with the ascending branches of these overturning circulations can also influence the far off climates through the planetary scale wave trains such as jet streams (Goswami and Chakravorty, 2017). Hence, part of the variance of climate phenomenon such as the South Asian monsoon can arise from remote ocean-atmosphere-land processes and their teleconnection via atmospheric and oceanic pathways. Hence, to understand the regional climate variability, it is necessary to identify the local interactions, the feedbacks, and remote teleconnections.

1.2 South Asian Monsoon

Etymologically, the word "monsoon" is derived from the Arabic word "mausam" meaning season as Arabian sailors used these winds that reverse seasonally to travel to and from India for trade. Monsoon is a planetary-scale phenomenon that occurs wherever a tropical continent is situated poleward of an equatorward ocean. It includes the Asian (South Asian and East Asian), African (North African and South African), American (North American and South American), and the northern Australian monsoon (Ramage, 1971). The monsoon, basically, is the redistribution of energy. It is manifested by the movement of the ITCZ (Inter Tropical Convergence Zone) in response to the asymmetric interhemispheric heating (Schneider et al., 2014; Gadgil, 2018). The ITCZ, also known as 'equatorial trough', is formed due to the convergence of moist and warm easterly winds that ascend and form deep convective clouds where maximum precipitation takes place when averaged temporally (Waliser and Gautier, 1993; Philander et al., 1996). This air mass, in the upper troposphere, moves away from the ITCZ position zonally and descends over subtropics. Once on the surface, it returns to the ITCZ position and thus forms the meridional Hadley circulation. Overall, mean position of the ITCZ is in the warmer of the two hemispheres; northern in the Atlantic and the Pacific Ocean due to northward heat transport by thermohaline circulation in the Atlantic and zonal transport of this heat by winds in the Pacific while ITCZ is south of the equator in the Indian Ocean due to local processes (Schneider et al., 2014). There is a widespread misconception that the monsoon is driven by the land-ocean temperature contrast, which reduces it to a gigantic land-sea breeze. This hypothesis essentially implies that higher land-ocean temperature contrast shall result in a stronger monsoon. In contrast, recent studies on South Asian summer monsoon have shown that the land temperature and the land ocean contrast are lower during higher monsoon precipitation (Kothawale and Rupa Kumar, 2002; Walker et al., 2015; Gadgil, 2018). India is, in fact, more hot before the summer monsoon season than during it and the hottest northwestern part of India receives the lowest precipitation (Gadgil, 2003, 2018). This hypothesis, therefore, shall be abandoned in favour of the ITZC migration and subsequent interpretations need to be carried out in its light.

Of all the various monsoons occurring over different continents, the South Asian monsoon is the most pronounced. It can be divided into summer or southwest (SW) monsoon occurring between June and September, and winter or northeast (NE) monsoon from mid-October to January. A low-pressure system (as low as 994 mbar) develops over the northwest Indian subcontinent during summer called as 'Indian Low'. In the Southern hemisphere, high pressure (up to 1025 mbar) exists over the southern subtropical Indian Ocean (~25°S) (Rao, 1976) around the so-called "Mascarene High" region off the southeast coast of Madagascar. The southeasterlies from the southern hemisphere move towards the low-pressure region and become south-westerly after crossing the equator due to the Coriolis force and hence are called the "SW or summer monsoon". The "Findlater jet", also called as "Somali jet" forms the core of the summer monsoon winds. It is a narrow, low-level (1 to 1.5 km high) cross-equatorial jet stream with wind speeds up to 15 m/s (Hastenrath and Lamb, 1979). The origin of the Findlater Jet is near the Mascarene High region. It reaches the African coast at 15°S and moves parallel to the eastern African coast causing Ekman transport leading to upwelling. It leaves the African coast between 5 to 10°N. Near ~55°E, it separates into two branches; the first goes towards the western coast of India while the second branch traverses around the southern tip of India and over southern Sri Lanka into the Bay of Bengal (Findlater, 1981). These winds carry abundant moisture causing rainfall over India during the summer season (June, July, August, September). The precipitation also releases latent heat of condensation that further increases the pressure gradient resulting in a stronger flow (Webster, 1987). In the case of NE or winter monsoon, the pressure conditions reverse with high pressure (up to 1035 mbar) in the East Asian continent south of the Lake Baikal and low pressure (~1110 mbar) over the southern subtropical Indian Ocean (Rao, 1976). The direction of the wind, therefore, reverses and now it moves southward from a northeast direction thus constituting the NE monsoon.

1.3 South Asian monsoon variability and its forcing factors across different time scales

The monsoon exhibits variability on various timescales that include intra-seasonal, inter-annual, decadal, centennial, millennial, orbital, and tectonic timescales. To understand the monsoon variability, it is important to decipher its driving forces i.e., forcing factors. Various external (changes in the Earth-Sun orbital geometry i.e., Milankovitch cycles, solar activity changes) and internal (e.g., coupled ocean atmosphere phenomenon, volcanism, greenhouse gases abundance, cloud and ice cover, land-use change, etc.) forcings are proposed to influence the monsoon variability on different timescales. The leading cause of intra-seasonal variability is the Madden-Julian Oscillation (MJO), which is an eastward propagating disturbance of tropical convection in the Indian and Pacific Oceans with a periodicity of 40 to 60 days (Robertson and Vitart, 2018). Monsoon variability on interannual to multi decadal timescales predominantly arises from the internal processes within the interacting ocean-land-atmosphere-cryosphere system. It has been found that summer monsoon is strongly associated with ENSO (Pant and Parthasarathy, 1981; Rasmusson and Carpenter, 1983). El Niño years are associated with the below-normal rainfall while La Niña years are associated with the above-normal rainfall though it has been shown to weaken in recent years and exhibits better relation with central equatorial Pacific heating - the El Niño Modoki (Kumar et al., 2006; Ashok et al., 2007). This relation is further affected by the Indian Ocean Dipole (IOD) with a stronger monsoon reported during positive IOD (warmer temperatures in western equatorial Indian Ocean) (Ashok et al., 2001). Further, on interannual to decadal and multi-decadal timescale, the monsoon variability shows a linkage with the North Atlantic Oscillation (NAO) and related Atlantic Multidecadal Oscillation (AMO). The AMO is the SST anomaly over the North Atlantic Ocean on a multi-decadal time scale. It can modulate the amplitude of El Niño as well as the Indian monsoon (Kucharski et al. 2007). The AMO can affect the monsoon seasonal rainfall by changing the tropospheric temperature (TT) gradient significantly. It has been shown that the warm AMO phase is strongly correlated with the large-scale positive TT anomaly over Eurasia, which thereby increases the meridional gradient of TT. This enhances the monsoonal rainfall over the south Asian region and delays the withdrawal of rainfall (Goswami et al., 2006; Krishnamurthy and Krishnamurthy, 2016; Srivastava et al. 2002). On multi-decadal to centennial to multi-centennial timescale, the changes in the Total Solar Irradiance due to variations in solar activity caused by sunspot cycles (11-year Schwabe cycle, 22-year Hale cycle, 33-year Bruckner cycle, 88-year Gleissberg cycle, 208-year Suess cycle) are considered a major factor (Agnihotri et al., 2002; Tiwari et al., 2015).

On millennial time scale, the monsoon variability corresponds to the millennial scale events identified in North Atlantic (Bond cycles; Bond et al., 1997) and Greenland ice cores such as Dansgaard–Oeschger (D/O) oscillations (Dansgaard et al., 1993; Grootes et al., 1993). The North Atlantic marine records also revealed several episodes of cold events known as Heinrich events (Heinrich, 1988; Bond and Lotti, 1995). Similar millennial-scale oscillations are also found in the monsoon variability (Wang et al., 2001, 2008; Cheng et al., 2006). The northern hemisphere summer monsoon is weakened abruptly during millennial-scale cold events (Schulz et al., 1998; Singh et al., 2011). It has been shown that when the cold event occurs in the North Atlantic region, the polar jet stream shifts more towards the south, modulating the position of the winter storm track, and in turn winter precipitation increases (Asmerom et al., 2010). The meridional thermohaline circulation (THC) transfers heat between the high latitudes of the northern and southern hemispheres causing asynchronicity between them on the millennial timescale (Barker et al., 2009; Kawamura et al., 2007). Recent studies have opined that the Southern Hemisphere and Antarctica also play an important role in governing summer monsoon precipitation with weaker monsoon observed during warm episodes in Antarctica (Gebregiorgis et al., 2018; Tiwari et al., 2021 and references therein). Kumar et al., 2021 have shown, using reconstructed SST and paleo-model data that cold SSTs in the southern mid-latitude region of the Indian and Southern Ocean were associated with intense monsoon intervals and warm spells were associated with weak monsoon intervals on the millennial to multi-millennial timescale. They proposed that instead of solely ascribing all the millennial-scale variability to the influence of northern high latitude climate, we should consider it in the context of bipolar coupling facilitated by the THC. This coupled climatic anomaly is transferred to the southern mid-latitude region, which also possesses independent regional climatic changes. The combined effect is then propagated northward to the Mascarene High region and the northern Indian Ocean, which affects the cross-equatorial pressure gradient and the millennial-scale South Asian summer monsoon variability (Kumar et al., 2021).

On orbital time scales, the monsoon variability corresponds to the glacial-interglacial cycles (global ice volume) and follows the insolation modulated by Milankovitch cycles (mostly precession), and the atmospheric greenhouse gases (mostly CO_2) abundance changes (Molfino and McIntyre, 1990; McIntyre and Molfino, 1996; Cheng et al., 2016; Kathayat et al., 2016). Increased CO_2 concentration produces the thermodynamic effect as enhanced warmth leads to higher moisture carrying capacity resulting in more precipitation. On the other hand, precession causes a dynamical effect by changing the meridional distribution of insolation resulting in changing meridional temperature gradient, which influences the cross-equatorial pressure gradients and the flow of monsoon circulation. The monsoon variability is thus a combined effect of thermodynamical and dynamical effects (Han et al., 2021). The greenhouse gases abundance variability is an important factor even on shorter than orbital timescales. The longest time scale is 'tectonic' and is considered to be 106 years or longer. The monsoon evolution on this time scale, as the name suggests, is linked with mountain building, and ocean closures. At this time scale the monsoon history traces beyond Quaternary and deals with the origin of the monsoons. Several studies have tried to understand monsoon variability on this timescale based on the eolian deposits, marine and terrestrial sediment, and recent scientific drilling in the Arabian Sea and Bay of Bengal (Quade et al., 1989; Rea, 1994; Kroon et al., 1991; Gupta et al., 2015; Huang et al., 2007; Betzler et al., 2016; Tripathi et al., 2017; Clemens et al., 2021). The origin and strengthening of the South Asian monsoon are related to the uplift of the Himalayas and the Tibetan Plateau (Kutzbach et al., 1989, 1993; Ruddiman and Kutzbach, 1989; Ruddiman et al., 1989; Prell and Kutzbach, 1997; Clift et al., 2008). The barrier effect of the Himalayas i.e., stopping the cold, dry northerly wind and not allowing the warm, moist monsoon winds to escape is now considered more important than the Tibet Plateau's role as an elevated heat source (Molnar, 2010). The Indian Plate collided with the Eurasian Plate at ~50 Ma resulting in the Himalayan orogeny. Though a few studies provide evidence for an Eocene proto-monsoon, the major monsoon intensification took place in the early Miocene (~24 Ma) and middle Miocene (~15 Ma) when the Himalayas attained critical heights (Clift and Webb, 2018). Thereafter, major monsoon intensification has been reported during the Mid-Pliocene Warm Period (MPWP) and at ~1 Ma corresponding to the mid-Pleistocene Transition (Tripathi et al., 2017). Changes in Indonesian Throughflow at ~3 Ma (Sarathchandraprasad et al., 2021) and Panama Gateway closure at 5 Ma (Thomson et al., 2021) have strengthened the summer monsoon. Overall, the SASM variability is a combination of the influences due to orography, precession, atmospheric CO_2, ice volume, and ocean gateways (Thomson et al., 2021).

1.4 Significance of the present study

Despite the above advances in understanding the monsoon variability, the teleconnection with Arctic climate variability is sparsely explored especially on longer timescales. The immense reduction of sea ice in the Arctic affects the polar and mid-latitude weather patterns significantly, which can influence the tropical climate and monsoon. The dominant climate mode, which changes the storm track (jet stream) and the mid and high latitude climate, is the North Atlantic Oscillation and Arctic Oscillation (NAO and AO). The NAO/AO represents the atmospheric pressure gradient between mid and high northern latitude. When the NAO/AO is in a positive phase, the atmospheric pressure is low at the pole and that causes the storm track to concentrate more towards the poles. Thus, the winters are mild across northern Eurasia but cold in the Arctic. However, during the negative phase of NAO/AO, the storm track shifts equatorward bringing more cold winds toward the mid-latitude region. It results in prominent winters across the mid-latitude region and mild conditions in the Arctic region (Cohen et al., 2014; Vihma, 2014; Liu et al., 2012). The Arctic warming and the reduction of sea ice weaken the zonal flow of the jet stream and increase its meridionality. This process induces favourable conditions for the anomalous high pressure in northwest Europe and increases the surface air temperature. Thus, the Rossby wave propagation towards East Asia influences the subtropical high over there and modulates the rainfall event in East Asia (Chatterjee et al., 2021).

In the current global warming scenario, the rapid reduction of the Arctic sea ice is the centre of focus. The sea ice variability and its effect on the mid-latitude region have been well studied (e.g., Cohen et al., 2014; Vihma, 2014; Jaiser et al., 2011). However, the impact of Arctic sea ice variability on the Indian summer monsoon and the underlying mechanisms have been studied by only a few workers (Krishnamurthy and Krishnamurthy, 2016; Chatterjee et al., 2021; Krishnamurti et al., 2015). Such studies are based on short time series data hence need to be validated on longer timescales during periods with similar climatic conditions as expected in near future. It will help to explore teleconnections between low-frequency variabilities, if present, and can provide new insights into the underlying mechanism. Also, models provide invaluable tools for predicting the future climate but they need to be evaluated against past climate reconstructions similar to what is expected in the near future. Such an opportunity is provided by the Mid-Pliocene Warm Period (MPWP), which possesses similar temperatures as expected in the next couple of centuries (IPCC AR6). Other significant warm periods in recent geological history are the last interglacial and the Holocene. These warm periods, studied in the present thesis, are discussed in detail below.

1.5 Time periods studied in the present thesis

1.5.1 Mid-Pliocene Warm Period (MPWP)

The mid-Pliocene Warm Period (MPWP) spans from 3.264 to 3.025 Ma (Dowsett et al., 2010; Haywood et al., 2010) and occurs within the Piacenzian Stage of the Late Pliocene period (Gradstein et al. 2004). The recent redefinition of the base of the Pleistocene, the MPWP is also referred to as mid Piacenzian warm period

(Dowsett et al., 2012). This warm interval is believed to have been the last episode when the global average temperatures were significantly warmer than the present and also characterized by climatic stability. In this interval, the air temperature was 10°C higher than today in the high latitude region, while the mid-latitude sea surface temperature was up to 3-4 °C warmer than present (Dowsett et al., 1996; Wara et al., 2005; Lawrence et al., 2006). The sea level is estimated to have been higher by 22 ±10m than the present sea level (Dowsett and Cronin, 1990; Miller et al., 2012). This interval was accompanied by a substantial reduction of the Arctic sea ice (e.g. Cronin et al., 1993; Polyak et al., 2010; Moran et al., 2006) and strong North Atlantic Deep Water formation (Raymo, 1994; Kim and Crowley, 2000). This warm interval is characterized by the negative excursion of $\delta^{18}O$ of benthic foraminifera indicating the Antarctic or Greenland ice volume could have been reduced (Lunt et al., 2008; Hill et al., 2010; Naish et al., 2009; Pollard and DeConto, 2009; Dolan et al., 2011). The warming during the MPWP is explained by the increase in atmospheric pCO_2, which was higher by 35% than the preindustrial. This is observed from the counting of stomatal leaf density (Van der Burgh et al., 1993), $\delta^{13}C$ ratio of the marine organic matter (Raymo et al., 1996), and general circulation modelling (Haywood et al., 2005). In addition to pCO_2 variability, the THC was also strong which drew heat from the equator to the high latitude region (Crowley, 1996; Dowsett et al., 1992).

1.5.2 Last Interglacial

The last interglacial period (MIS 5e) represents an interval of warm climate between 128 to 116 kyr BP. During this interval, the ice core record suggests that the greenhouse gas concentrations were slightly higher than the preindustrial (Petit et al., 1999), and the summer insolation was higher by ~10%. These small changes in the climatic parameter were sufficient to increase the polar temperature and it is estimated to be around 3-4°C higher than today (Otto-Bliesner et al., 2006) and the global mean temperature was higher by 1.5°C (Turney and Jones, 2010; Lunt et al., 2013). The ice sheets declined during this interval suggesting an increase in relative sea level by +5 and +9.4 m above modern sea level (Kopp et al., 2009; Dutton and Lambeck 2012; Rovere et al., 2016).

1.5.3 Holocene

The Holocene, known to be the current interglacial, spans from 11.7 kyr BP to the present. After the end of the last glacial period, the global average temperature increased in the early Holocene and reached its maximum during mid-Holocene thermal maxima, an exceptionally warm period from 8000 to 5000 yr BP (Otto-Bliesner et al., 2016). The Holocene global temperature was reconstructed from 73 globally distributed records, which shows that the Holocene thermal maxima was 0.4°C higher than the average period of 1961-1999 (Marcott et al., 2013). After the last glacial period, the sea level raised to 60 m from 11,650 to 7000 yr BP (e.g. Fairbanks, 1989, Bard et al., 1996). The early Holocene sea-level rise was largely driven by the meltwater release from the melting of ice masses and the breakup of coastal ice streams (Smith et al., 2011). By 7000 yr BP, the relative sea-level reached the global mean sea level (Fleming et al., 1998, Milne et al., 2005). During the Holocene, the atmospheric partial pressure of CO_2 is typically near 280 ppmv (Sigman and Boyle, 2000).

1.6 Objectives

The overarching aim of this thesis is to reconstruct the SASM and northern polar climate variabilities during the past significantly warm periods and explore the linkages between them. To achieve this aim, we have reconstructed the climatic variability from the Arctic and Atlantic during MPWP, the last interglacial, and the Holocene. Further, we have reconstructed the south Asian monsoon variability during the MPWP from the eastern Arabian Sea.

This study has the following specific objectives:

1. Reconstruction of paleoenvironmental condition during Mid Pliocene Warm Period at Atlantic-Arctic Gateway (Yermak Plateau)

2. Reconstruction of high-resolution South Asian monsoon variability during Mid Pliocene Warm Period

3. Quantification of oceanic temperature and salinity from North Atlantic since Late Quaternary

4. Explore the possible links between northern high latitude climate change and the South Asian monsoon system

1.7 Thesis Outline

There are six chapters in the present thesis. The Chapter 1 provides a general introduction to the different components of the Earth's climatic system and an overview of climatic teleconnection. This chapter also reviews the existing studies and discusses our understanding of monsoon's features, dynamics, and variability. The significance and objectives of the present study are also discussed here. Chapter 2 comprises the materials and methodology used in the present study including the sampling sites. This chapter reviews the stable isotope systematics, and different proxies used in this study. The basic principles of the instruments used are also discussed in this chapter. Chapters 3, 4, and 5 cover the major findings of this thesis work. Chapter 3 discusses the reconstruction of stratification using relative nutrient utilization at the Yermak Plateau, Atlantic-Arctic Gateway during the late Pliocene including the different forcing factors regulating the stratification variability. A modified version of this chapter is published as a research paper in the American Geophysical Union's (AGU) journal Paleoceanography and Paleoclimatology in the year 2021. Chapter 4 covers the reconstruction of South Asian Monsoon variability from the eastern Arabian Sea and discusses the teleconnection with Arctic sea ice variability during the late Pliocene period, which encompasses the MPWP. A modified version of this chapter is published as a scholarly article in the AGU journal Paleoceanography and Paleoclimatology. Chapter 5 outlines the climatic variability in the Norwegian Sea during the last interglacial period and during the Holocene. It mainly emphasizes the quantification of climatic parameters like sea surface temperature and sea surface salinity. Chapter 6 provides the synthesis of the major findings of this thesis work and is followed by a recommendation for future work.

Chapter 2

Materials and Methods

2.1 Sample details

To reconstruct the teleconnection between northern polar climate and the SoAM, the sediment core samples have been used from polar region and from monsoon dominated area i.e., Arabian Sea. The details of the sample used in this study are discussed below.

(a) ***Atlantic - Arctic gateway***

In order to understand the paleoclimatic conditions of the Arctic region during MPWP, sediment core samples were collected from the Atlantic-Arctic gateway region. The sediment core was retrieved during ODP expedition 151 from Site 910 and Hole ‘C’ (Fig. 2.1). The core site 910C is located at 80°15.896′N, 6°35.430′E in the eastern flank of Yermak Plateau, NW Spitsbergen, at a water depth of 556.4 m. The core length is 507.4 m long, out of which 199.2 - 276.2 m is used in the present study. The Hole 910C provides a complete Pliocene sequence (Myhre et al., 1995). The present study mainly focuses on the late Pliocene sequence that spans from 2.6 to 3.4 Ma (million years ago), including the MPWP.

(b) ***Eastern Arabian Sea***

In order to reconstruct the SoAM variability during the late Pliocene, sediment samples from the eastern Arabian Sea were used. The sediment core was drilled in the Laxmi Basin situated in the eastern part of the Arabian Sea (16°37.28′N, 68°50.33′E) during the IODP expedition 355 at a water depth of 3640 m (Fig. 2.1; Pandey et al., 2016). A total of five holes were cored at Site U1456 (U1456A-U1456E), with the deepest (Hole U1456E) reaching 1109.4 m below seafloor (Pandey et al., 2016). A core composite depth below seafloor (CCSF) was constructed to develop a common depth scale for all the holes using stratigraphic correlation during the expedition (Pandey et al. 2016). We used samples from 378.53 to 430.3 m (CCSF) pertaining to the late Pliocene. The age of the samples ranges from around 2.7 to 3.4 Ma, which spans the MPWP. The site's chronology is based on calcareous microfossil biostratigraphy and magnetostratigraphy and is discussed in detail in Routledge et al., 2019.

(c) ***Atlantic region***

In order to quantify the climate of the northern Atlantic region, sediment core collected from the Lofoten Basin in the Norwegian Sea was investigated. The sediment core was drilled by the Russian research vessel (RV) "Akademik Mstislav Keldysh" during its 62nd cruise named AMK-5188. The core AMK-5188 is located at 69°02.667′N, 02°06.595′E in the southern Lofoten Basin at a water depth of 3206 m (Fig. 2.1). The sediment core length is 417 cm, out of which 0 to 80 cm encompasses the Holocene and from 180 to 270 cm section comprises the Marine Isotope Stage 5 (MIS 5). The core is subsampled at 1cm for both sections.

Table 2.1: Details of the sediment core samples and their age spans (chronology construction is discussed in detail in the respective chapters)

Core name	Location	Temporal coverage	Latitude and Longitude	Water Depth (m)
ODP-151, 910C	Yermak Plateau	2.6 to 3.4 Ma	80°15.896′N, 6°35.430′E	556.4
IODP-355, U1456A	Arabian Sea	2.7 to 3.4 Ma	16°37.28′N, 68°50.33′E	3640
AMK-5188	Norwegian Sea	1 to 14 kyr BP and 89 to 145 kyr BP	69°02.667′N, 02°06.595′E	3206

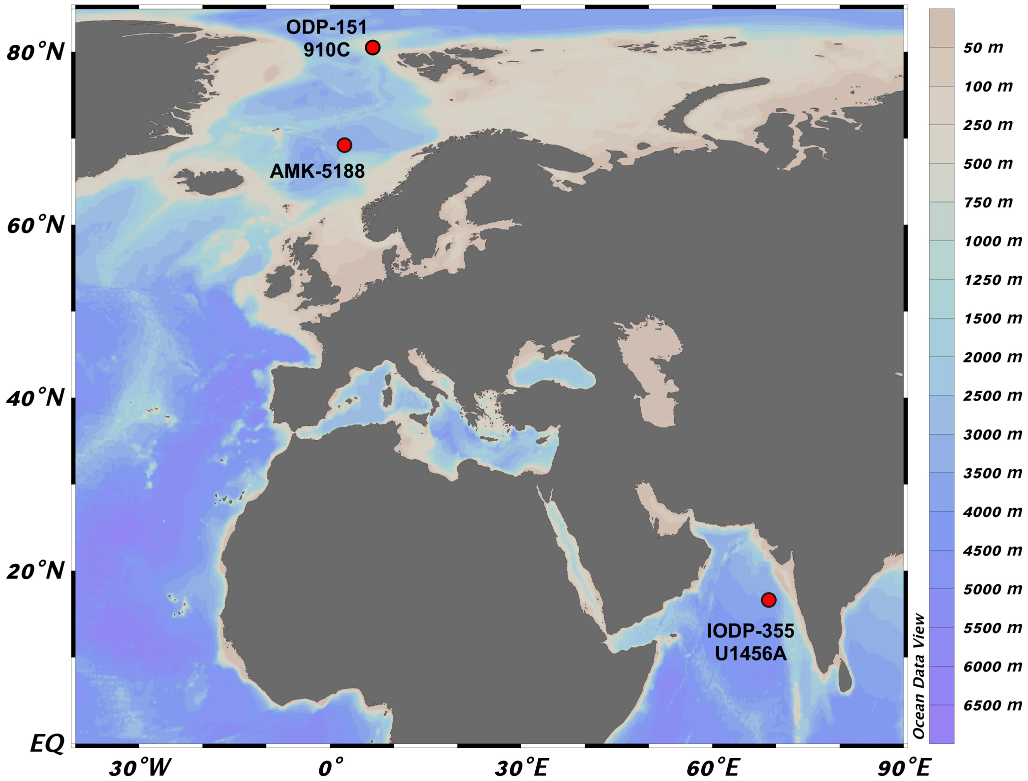

Figure 2.1: The sampling locations used in the present study. The core sites are shown by red dots.

2.2 Stable isotope systematics

The isotopes are the atoms with the same number of protons and position in the periodic table and differ in the mass number due to the different number of neutrons in the nuclei. The isotopes with long half-lives or no disintegration are considered stable isotopes, while those that disintegrate spontaneously and have measurable half-life are called radioactive isotopes. The stable isotopes form due to the counterbalance between the repulsive force produced by the positively charged proton and the neutrons; however, the repulsive force increases with increasing protons. The isotopes of a given element have the same chemical properties but different physical properties due to different atomic masses. The properties like density, boiling point, melting point and viscosity are more for the heavier compounds than the lighter compound. The different mass also influences the vibrational frequency of the molecule. The lighter isotope molecule has a higher vibrational frequency and higher vibrational energy than a molecule containing the heavier isotope. Thus, less energy is required to break the bond formed by the lighter isotopes than the bond formed by the heavier isotopes. It suggests that the molecule with lighter isotopes can more readily participate in the chemical processes than those with heavier isotopes. It leads to isotopic fractionation. The isotopic fractionation is the relative partitioning of the heavier and lighter isotope between two coexisting phases in a natural system. In equilibrium fractionation, the isotopes exchange takes place between the reactant and product but the net reaction is zero. The equilibrium constant (K) in an equilibrium reaction is expressed as heavier to lighter isotope ratio in the solid and liquid phase; for example, the calcitic shell of foraminifera precipitate in equilibrium with the ambient seawater. $K = (^{18}O/^{16}O)_{calcite}/(^{18}O/^{16}O)_{water}$. Thus, the isotopic fractionation factor (α) for this reaction is $\alpha = (^{18}O/^{16}O)_{calcite}/(^{18}O/^{16}O)_{water}$. In kinetic fractionation, the reaction is incomplete and unidirectional. Thus, the lighter isotope and heavier isotope have two different rate constants i.e., k_L and k_H respectively. When k_L/ k_H is greater than 1, the reactant with lighter isotope reacts more rapidly than the heavier isotope, which is normal. However, when the ratio is less than 1 it is called as inverse, where the heavier isotope reacts more rapidly than the lighter isotope.

It is difficult to measure the absolute isotopic abundance, thus the isotopic ratio determines the ratio of the number of heavier isotopes to the number of lighter isotopes. The Isotope Ratio Mass Spectrometer (IRMS) is used for the isotopic analysis. However, the IRMS measures the difference between isotopic ratios of two compounds as both of them experience the same conditions during the analysis. The isotopic abundance is reported in the delta (δ) value. It is the relative difference between the isotopic ratio of sample and the international standard.

$$\delta = \left(\frac{R_{sample}}{R_{standard}} - 1\right) \times 1000$$

Where R_{Sample} and $R_{Standard}$ are the ratios of the heavier to lighter isotope in the sample and standard. δ–value is dimensionless as it is the ratio of two quantities of the same kind. It is multiplied by 10^3 and expressed in per mil (‰).

2.3 Theoretical background of the proxies used in the present study

2.3.1 Nitrogen isotope ($\delta^{15}N$) of the sedimentary organic matter

Nitrogen has two stable isotopes, i.e., ^{14}N and ^{15}N, with 99.64% and 0.36% abundance, respectively. The nitrogen isotopes are discriminated by the physical, chemical, and biological processes occurring in the oceans. Nitrogen in the form of nitrate (NO_3-) is one of the major nutrients required by the phytoplankton for their growth. The nitrogen isotopes variation is mostly dominated by "kinetic fractionation" in the marine nitrogen cycle. The isotopic fractionation (ε) of a given reaction can be defined as the deviation of the ratio of rate coefficients with which the two nitrogen isotopes (^{14}N and ^{15}N) are converted from reactant to product:

$$\varepsilon\ (‰) = (^{14}K/^{15}K - 1) \times 1000$$

Where, the ^{14}K is related to the ^{14}N reactant and ^{15}K is related to ^{15}N reactant.

The isotopic fractionation during the nitrogen fixation, which is the reduction of nitrogen to NH_4^+ and oxidation to NO_3^- and NO_2^-, is less than 2‰. Thus, the $\delta^{15}N$ of the particulate nitrogen slightly decreases and that reflects in the $\delta^{15}N$ of the organic matter. In case of the nitrate utilization by the phytoplankton, the fractionation is small ($\varepsilon = \sim 5$‰) and a slight increase in $\delta^{15}N$ values. During nutrient utilization process the $\delta^{15}N$ values of the organic matter depend on the nitrate concentration at the surface (Altabet and Francois, 1994). The high nitrate concentration and replenishment of nutrients at the surface result in more availability of ^{14}N nitrate, which shows low nutrient utilization and low $\delta^{15}N$ values of the organic matter (Altabet and Francois, 1994; Sigman et al., 2009). The link between the nitrate consumption and the sediment $\delta^{15}N$ provides an opportunity to reconstruct the past nitrate utilization by the phytoplankton. The nitrogen isotopic fractionation is large during the denitrification process, which occurs in the water column depth of ~250-1250 m. During denitrification, the nitrate acts as an electron acceptor in an oxygen minima zone and is reduced to any gaseous nitrogen (N_2 and N_2O) by the anaerobic bacteria for the decomposition of the organic matter. The isotope fractionation during denitrification is around 25‰ resulting in very high $\delta^{15}N$ values (more than

15‰). Thus, denitrification provides information about the change in surface productivity and the associated processes.

2.3.2 Carbon isotope of sedimentary organic matter and the foraminifera

Carbon contains two stable isotopes, ^{12}C and ^{13}C with atomic masses of 12 and 13, respectively. ^{12}C is the more abundant of the two, comprising 98.89 %, while ^{13}C of 1.11 % is found in nature (Craig, 1953). In an organic system, the photosynthesis process preferentially uptake ^{12}C via kinetic fractionation. In an inorganic carbon system, the atmospheric CO_2 converts to dissolved bicarbonate, and then it precipitates into the solid carbonate, e.g., shells of the marine organisms (foraminifera). The equilibrium fractionation in the inorganic carbon system enriches the heavier isotope (^{13}C) in the carbonates. The fractionation factors are different in different stages of carbonate formation. The $\delta^{13}C$ of the planktic foraminifera varies at different depths due to the presence of the vertical gradient in the dissolved CO_2. In the photic zone, the high surface productivity uses the lighter isotope more (^{12}C) for photosynthesis and enriches the surface water with the heavier isotope (^{13}C). The planktic foraminifera calcifying their tests in isotopic equilibrium with the seawater has higher $\delta^{13}C$. The $\delta^{13}C$ value is low for the mixed layer, thermocline, and deep-water species due to lower photosynthesis and decay of organic matter that releases ^{12}C. The $\delta^{13}C$ of benthic foraminifera indicates the bottom water ventilation related to the age of the water. The older water mass has a low $\delta^{13}C$ value due to respiration, which releases lighter isotope (^{12}C) into the water.

The carbon isotope of the organic matter is used to understand the provenance of the organic matter in a marine environment. The $\delta^{13}C$ of atmospheric CO_2 is ~ -8 ‰ (Hoefs, 2009). The plant preferably takes the ^{12}C during the photosynthesis via kinetic fractionation. There are two steps of the kinetic fractionation involved in the photosynthesis of the terrestrial plant. (1) The fractionation occurs during the uptake of CO_2 gas by the stomata of the leaves and (2) then the fractionation occurs during the carbon fixation by the respective enzymes for C3 and C4 plants. The $\delta^{13}C$ values of the C3 plant range from -20 ‰ to -36 ‰ with a mean value of -27 ‰ (Farquhar et al., 1989). While the $\delta^{13}C$ value of the C4 plant range from -9 ‰ to -17 ‰ with a mean value of -13 ‰. The $\delta^{13}C$ values of the marine phytoplankton/ plants are higher in comparison to the C3 plants and range from -11 to -39 ‰ with a mean value of -21 ‰ (Farquhar et al., 1989).

2.3.3 Total organic carbon and total nitrogen

The unicellular organisms like phytoplankton and zooplankton largely contribute to the source of organic carbon in the marine environment. Primary production in the marine environment is an important factor in the climate system as it draws down the CO_2 from the atmosphere to the ocean. The largest part of the organic matter produced in the photic zone of the ocean is however recycled back to the inorganic carbon and some part is consumed by the benthic organism after settling down to the bottom. Finally, less than 1% of the overhead surface productivity is preserved in the sediment called sedimentary organic matter. Thus, the organic carbon and nitrogen concentration of the sedimentary organic matter is used as a proxy for the surface productivity. The high/low TOC and TN represent high/low productivity.The C/N ratio in combination with the $\delta^{13}C$ values of the organic matter is also used to determine the provenance of the organic matter. The elemental composition of the marine organic matter was given by Redfield (1934, 1958) as carbon:nitrogen:phosphorus :: 106:16:1, which is called as Redfield ratio. Thus, the C/N ratio is 6.6 for marine organic matter. The C/N ratio of the marine sediment ranges from 8 to10. However, the land plants have a higher C/N ratio that varies between 20 and 100 due to the presence of carbon rich compound like lignin, cellulose, etc., (Premuzic et al., 1982). In the present study, the provenance of the marine organic matter is established using cross-plots of $\delta^{13}C$ and C/N ratio of the sedimentary organic matter.

2.3.4 Oxygen isotope of foraminifera

Oxygen has three stable isotopes namely, ^{16}O, ^{17}O, and ^{18}O with abundances of 99.763%, 0.0375%, and 0.1995% respectively. For the paleoclimate reconstruction, the ratio of $^{18}O/^{16}O$ is determined as ^{18}O has a higher abundance than ^{17}O and a greater mass difference with ^{16}O. The $\delta^{18}O$ of the seawater varies with the change in ambient temperature. Therefore, studies have been conducted to construct the empirical equation for the temperature and the seawater $\delta^{18}O$

(Shackleton, 1974; Erez and Luz, 1983; Bemis et al., 1998). The following empirical equation has been proposed for temperature determination:

$$T\ °C = 17.0 - 4.52\ (\delta^{18}Oc - \delta^{18}O\ w) + 0.03\ (\delta^{18}Oc + \delta^{18}Ow)^2$$

Where T is sea surface temperature in °C, $\delta^{18}O_c$ and $\delta^{18}O_{sw}$ are $\delta^{18}O$ of carbonate and seawater, respectively. However, the limitation in this equation is the $\delta^{18}O$ of the seawater as it depends on the amount of ice stored on the continent, which is called the ice volume effect. During the glacial conditions, a large portion of the ocean water is locked in the continent as polar ice sheets. These ice sheets are depleted in heavier oxygen isotope (^{18}O) and thus, the result is the enrichment of ^{18}O in the seawater. The foraminifera calcifying their shells in isotopic equilibrium with the seawater during glacial times reflect high $\delta^{18}O$ values than those calcifying during the interglacial period. Thus, the $\delta^{18}O$ of the foraminifera is also used to reconstruct the glacial-interglacial cycles i.e., the change in ice volume. The $\delta^{18}O$ values of the benthic foraminifera are mostly preferred to reconstruct glacial interglacial fluctuation, as the short-term change in temperature and salinity does not affect them.

2.3.5 Trace element ratio (Mg/Ca) of foraminifera

The Mg^{2+} is the divalent cation, which substitute Ca during the formation of the biogenic $CaCO_3$. The incorporation of the Mg^{2+} into the foraminiferal calcite is influenced by the temperature of the surrounding water during their growth. Thus, the Mg/Ca ratio increases with increase in temperature; hence the ratio is used to reconstruct the sea surface temperature. Since the oceanic residence time of Ca and Mg are relative long i.e., 10^6 and 10^7 years, respectively, therefore the Mg/Ca ratio of the seawater may consider to be constant over glacial and interglacial periods. From the culture experiment and core top studies provides an exponential relationship between temperature and foraminiferal Mg/Ca for most planktic foraminifera. The empirical equation is Mg/Ca = B (exp AT), where A and B are different for various foraminiferal species (Elderfield and Ganssen, 2000; Anand et al., 2003; Regenberg et al., 2009). The temperature is the primary control on Mg/Ca, however, the pH and salinity has additional influence on the incorporation of Mg^{2+} into the calcite. Mg/Ca positively varies with the salinity and that requires attention when there is a large-scale salinity changes with the time (Nürnberg et al., 1996; Kisakürek et al., 2008). The seawater pH is, however, negatively correlated to the Mg^{2+} uptake and both effects are assumed to cancel each other. This method has unique advantage as compared to the other paleothermometry proxies because Mg/Ca is measured from the same foraminiferal species that yielded the $\delta^{18}O$ data. Thus, it avoids the seasonality, habitat, and transport of ex-situ material effect on SST reconstruction.

2.4 Instrumental analysis

2.4.1 Inductively Coupled Plasma-Optical Emission Spectrometry (ICP-OES)

ICP-OES is widely used and has versatile method of inorganic analysis. It is used in the present work to measure the trace element ratio of foraminifera.

Principles of ICP-OES:

The ICP-OES is a technique, which uses plasma as a source and relies on the optical emission for the analysis. The plasma, which has high electron density and temperature up to 10000 K excites the atom and ions into higher energy levels. When the atoms return to lower energy levels, they release emission rays (spectrum) corresponding to its specific wavelength. The element type is determined based on the position of the photon rays on the detector and the concentration of each element is determined from the ray’s intensity.

***Analysis process*:**

The liquid sample drawn by the peristaltic pump goes into the nebulizer, where the liquid gets converted into fine aerosol particles. In the spray chamber (nebulizer) the larger water droplets drain away and the fine droplets are directed into the hot plasma. In the plasma, the aerosol vaporizes and its atoms and ions are excited to high energy level, so their characteristic wavelength light is emitted during its transition to lower energy states. The emitted light is transferred to high-resolution optical system, which separates the light into specific wavelength for the element to be measured. The light falls on the detector system, which measures the intensity of the emitted wavelengths. Each individual wavelength is detected and an integrated software converts them into concentration unit. In the present study, ICP-OES is used to measure the concentration of Mg and Ca in the test of foraminifera. The known standards are used to calibrate the results.

2.4.2 Elemental Analyzer

The elemental analysis determines the amount of an element in a compound, mainly the weight percentage. A CN analyzer determines the elemental composition of the samples. The name CN derives from the primary elements i.e., carbon (C) and nitrogen (N).

***Basic principle*:**

The sample capsule is injected into a high temperature (950°C) combustion tube and there it combust completely in pure oxygen. Toward the end of the combustion, a high supply of oxygen is added to ensure the completion of combustion of all organic and inorganic substances. The combustion products pass through specific reagents to produce CO_2, H_2O and N_2 and oxides of nitrogen. These reagents also remove interferences like halogen, sulfur and phosphorous. The gasses are then passed over to the copper in the reduction tube, where it reduces the oxides of nitrogen to elemental nitrogen. Then it mixes homogeneously in the mixing chamber at constant temperature and pressure. The gas mixture passes through high precession thermal conductivity detector.

2.4.3 Isotope Ratio Mass Spectrometer (IRMS)

The Isotope Ratio Mass Spectrometer (IRMS) is used to measure the isotopic abundances. It separates the charged molecules and atoms according to their masses in the electromagnetic field. Basic principle of this instrument is discussed below:

There are four main parts in the mass spectrometer i.e., (1) the inlet system, (2) the ion source, (3) the mass analyzer, and (4) the ion detector.

(1) *The inlet system:* The inlet system has a changeover valve, which allows the rapid and consecutive analysis of two different gas samples (sample and standard gases). The gases enter the system through thin capillaries of around 0.1mm in diameter and about 1m in length.

(2) *The ion source:* The ions are formed in this part of the mass spectrometer. Thereafter it is accelerated and focused into a narrow beam. The gas flow is molecular in the ion source and it converts into ions due to the bombardment from electron beam emitted by a heated filament. The emitted electron accelerates by electrostatic potential to an energy level between 50-150 eV. The ionized molecules are drawn out of the electron beam by an electric field and it accelerated by several kV. Thus, the positive ions enters the magnetic field with same kinetic energy i.e., $\frac{1}{2} Mv^2 = eV$.

(3) *The mass analyzer:* It separates the ion beams coming from the ion source based on their mass/charge (m/e) ratio. The ion beam is deflected to the circular path after entering into the magnetic field. The radii are proportional to the square root of the m/e. Thus, the beams are characterized by a particular m/e ratio.

(4) The ion detector: After the magnetic field the separated ions are collected in ion detector. These ions are converted into an electric impulse and then fed in to an amplifier, which measures the current.

Chapter 3

Enhanced Arctic Stratification in a Warming Scenario: Evidence From the Mid Pliocene Warm Period

3.1 Introduction

Global warming is expected to be most pronounced in the polar regions, which is seen most dramatically in the Arctic Ocean with significant sea ice loss over the last few decades (Cavalieri & Parkinson, 2012). The sea ice regulates various factors such as surface albedo, ocean-atmosphere heat exchange, and potential freshwater export to the North Atlantic. This in turn influences the deep-water formation in the North Atlantic and global ocean circulation (Sévellec et al., 2017). Recent studies using mooring data and models suggest the oceanic heat input via advective inflow of warm North Atlantic Current (NAC) and Pacific waters into the Arctic Ocean plays a major role in sea ice melting (Pnyushkov et al., 2015). This scenario is seen in the eastern Eurasian Basin, where the NAC interacts with surface waters and weakens the stratification, thereby contributing to the sea ice melt (Onarheim et al., 2014). However, the enclosed Arctic Ocean receives a huge amount of freshwater from the Circum-Arctic river discharge (11% of the global river discharge, Gleick, 2000) and precipitation (Rudels et al., 1991). This large volume of freshwater influx contributes to additional heat input by strengthening the upper water column stratification, which reduces the sea ice cover (Carmack et al., 2015). Alternatively, the stratified water column also prevents the sea ice from melting by inhibiting the vertical mixing of warm Atlantic water with the surface layer (Aagaard et al., 1981). Hence, knowledge of past variability of stratification during analogous warm periods may help in understanding the significance of stratification in the melting of sea ice in the Arctic Ocean.

To improve our understanding of the impact of a warmer climate on Arctic stratification, past climates with similar boundary conditions need to be examined. Such an opportunity is presented by the Mid-Pliocene Warm Period (MPWP, 3.264 – 3.025 Ma, million years ago; Dowsett et al., 2009; Dowsett et al., 2019; Haywood et al., 2020), which is the most recent such event when the conditions were similar to the present with similar CO_2 concentration (365 – 415 ppmv, Berends et al., 2019; Bartoli et al., 2011), a sea-level higher by approximately 20 m than the present (Rohling et al., 2014), and annual mean surface temperature higher by 2.7°C - 4.0°C (Haywood et al., 2013).

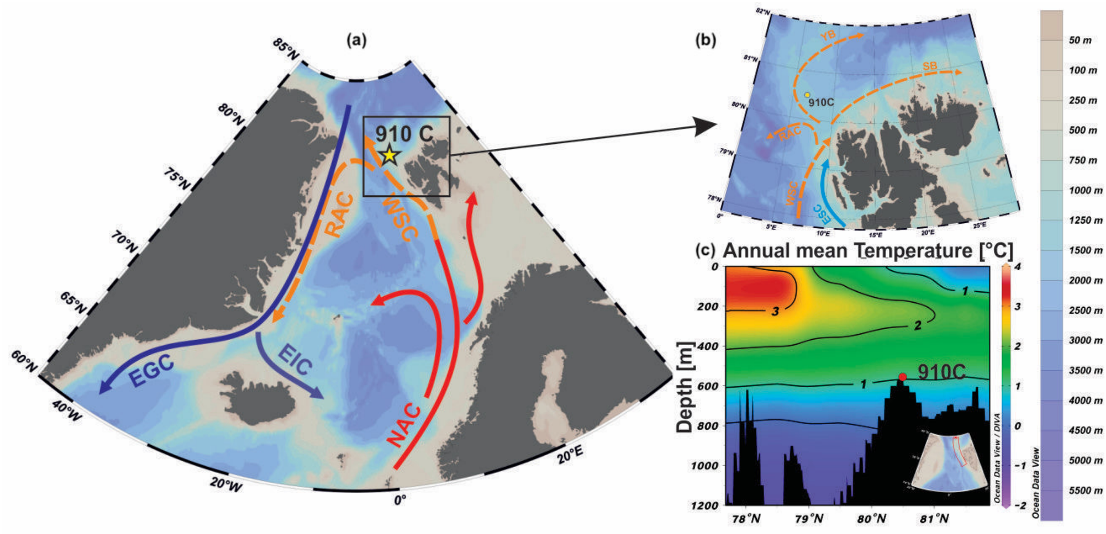

Figure 3.1: Sampling location. (a) Location of sampling site 910C (80°15.896'N°, 6°35.430′E) shown as a star. The Norwegian Current transports North Atlantic warm water from 60° N to the Arctic region. RAC - Return Atlantic Current, WSC - West Spitsbergen Current, NAC - North Atlantic Current, EIC - East Icelandic Current, EGC - East Greenland Current. Surface and subsurface water are shown by solid and dotted lines respectively; (b) The warm and saline NAC circulation at the Yermak Plateau. ESC - East Spitsbergen Current, YB - Yermak Branch, SB - Svalbard Branch; (c) Profile of mean annual temperature at the Yermak Plateau; the core location is marked as red dot and the inset shows the transect.

Earlier studies on MPWP have shown that the sea ice coverage at the Atlantic-Arctic Gateway (AAG) region reduced considerably (Cronin et al., 1993; Rahaman et al., 2020). Other studies, though at a coarser resolution or spanning only a few glacial-interglacial cycles, noted that the oceanic circulation/ventilation at the AAG reduced (enhanced) during colder (warmer) periods (Dowsett et al., 1992; Ravelo & Andreasen, 2000). The model simulations also observed that the Atlantic Meridional Overturning Circulation (AMOC) was stronger with enhanced oceanic heat transport to the polar region during the MPWP (Otto-Bliesner et al., 2017; Zhang et al., 2020). Despite the above advances, high-resolution (multi-millennial scale) studies on various facets of circulation at the AAG including water column stratification for the MPWP are lacking. Here, we aim to understand changes in Arctic stratification during glacial and interglacials of MPWP by studying the relative nutrient utilization and productivity from the Yermak Plateau, AAG (Fig. 3.1).

Water column stratification in higher latitudes can be constructed using the relative nutrient utilization variability inferred from the nitrogen isotopic composition ($\delta^{15}N$) of sedimentary organic matter (Thibodeau et al., 2017). In polar and subpolar regions, the nitrogen isotopic value of the settling organic matter is controlled by the degree of nutrient utilization (Schubert & Calvert, 2001). In the photic zone, the phytoplankton preferentially uptake the lighter ^{14}N-nitrate over the heavier ^{15}N-nitrate, provided nitrate uptake is incomplete. Under nitrate replete conditions (low relative nutrient utilization), the settling particulate organic matter is depleted in the heavy isotope (low $\delta^{15}N$). While under nitrate poor conditions (high relative nutrient utilization), the phytoplankton consumes a relatively higher amount of ^{15}N-nitrate resulting in high $\delta^{15}N$ (Altabet & Francois, 1994). In the Arctic Ocean, the nutrient concentration at the surface is controlled by the mixed layer thickness and thus by the stratification of the upper water column (Codispoti et al., 2013). The stronger stratification in the Arctic Ocean during spring and summer (growth season) limits the nitrate to the photic zone, resulting in maximum consumption of nutrients at the surface. This leads to high relative nutrient utilization and thus the settling organic particles are isotopically heavier (high $\delta^{15}N$) (Thibodeau et al., 2017). The major nutrient source to the Arctic Ocean is advective nutrient input via Atlantic and Pacific entrances (Torres-Valdes et al., 2013). Nutrient inputs from the river and sea ice melt are small (1.46 – 1.7 kmol nitrate s^{-1}) in comparison to the advective inputs (~52 kmol nitrate s^{-1} through Fram Strait) (Torres-Valdes et al., 2013). The $\delta^{15}N$ values can indicate relative nutrient utilization related to mixed layer depth and hence, the mixing of nutrient-rich Atlantic water with the surface. We use this approach of temporal variation in nitrate utilization to study the past stratification at the Ocean surface at Fram Strait.

3.2 Modern Oceanography at the Study Site

ODP Hole 910C is located at 80°15.896'N°, 6°35.430′E in southern Yermak Plateau at a water depth of 556.4 m. The NAC feeds the Norwegian Current, which in turn supplies water to the West Spitsbergen Current (WSC) (Fig. 3.1a and 3.1b). The WSC transports the relatively warm (>3°C) and saline (>35.0) North Atlantic water into the Arctic Ocean (Fig. 3.1b and 3.1c; Beszczynska-Mller, 2012). The WSC sup- plies heat to the eastern Fram Strait making it the northernmost perennially ice-free sea area in the world (Haugan, 1999). Cold and relatively low salinity water, carrying on an average approximately 1,300 km3 of freshwater, annually outflows from the Arctic Ocean via the East Greenland Current (EGC) (de Steur et al., 2009). The heat transport to the Arctic Ocean through NAC along eastern Fram Strait varies season- ally. The core site experiences ~2°C warmer temperature during the summer period than during the winter period (Fig. 3.2c and 3.2f). The sensitivity of the seawater density to the temperature reduces in the polar region as it reaches the freezing point and thus, the stratification in the Arctic Ocean is primarily due to the salinity gradient in the water column (Adkins et al., 2002). Based on salinity distribution, the Arctic Ocean water column is separated into three different layers (Rudels et al., 1991). The polar surface layer extends from ~0 to 250 m depth, which consists of the Polar Mixed Layer (PML) and the halocline. The PML comprises fresh and cold water from the Pacific Ocean, river runoff, an excess of precipitation over evaporation, and sea ice melt (Nummelin et al., 2016). The cold halocline (~50 – 250 m depth), which has an advective origin, separates the cold and fresh surface water from warm and saline intermediate Atlantic water (Rudels et al., 1991; Rudels, 2015). In the Eurasian Basin, this layer is formed by the advection of higher saline Atlantic water along the shelves to the deeper basin (Coachman & Barnes, 1962). The warm and saline water in the intermediate layer (~400 – 600 m depth) is advected from the north Atlantic to the Arctic Ocean and descends beneath the surface layer in the Nansen Basin, from where it supplies nutrient to the surface through diapycnal mixing (Rudels et al., 1991; Randelhoff et al., 2015).

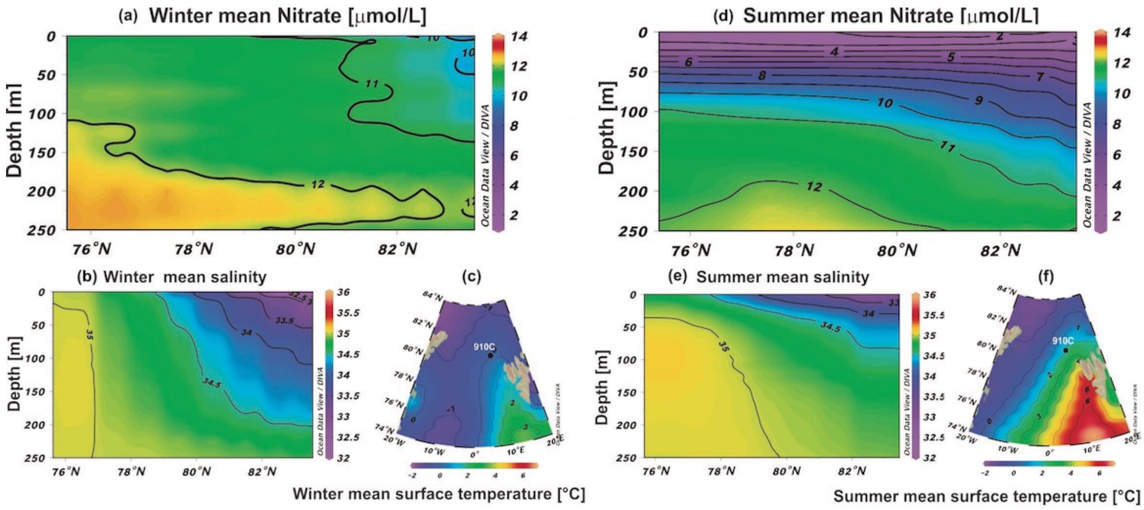

Figure 3.2: Modern oceanographic conditions (a), (d) Profile of nitrate concentration variability during modern winter and summer periods at the sample location; (b), (c), (e), and (f) profile of modern winter and summer mean salinity and temperature variability at the study site. The black dot shows the sampling location (c) and (f) and the section track is given in the Supplementary Information.

During summer, the surface water is well stratified with a mixed layer thinner than 30 m (Fig. 3.2d and 3.2e), which results in low nitrate concentration (2 – 4 μmol/L) at the polar mixed layer during this period (Fig. 3.2d). In winter, the sea ice formation, brine rejection, and haline convection promote the deeper mixing, which creates the PML thickness up to ~250 m depth (Fig. 3.2a and 3.2b). The deeper mixing allows for the replenishment of nutrients at the surface and thus, the nitrate concentration is higher ~11 μmol/L at the surface during winter in comparison to the summer period (Fig. 3.2a).

3.3 Materials & Methods

3.3.1 Study Site and Age-Depth Model

The 507.4 m long sediment core was raised from 556.4 m water depth in the southern part of Yermak Plateau (80°15.896'N°, 6°35.430′E) and out of which 199.2 – 276.2 m is used in the present study pertaining to the late Pliocene. The chronology of the core is constructed using the tie points as given in Table 3.1 (Fig. 3.3) and described in detail elsewhere (Rahaman et al., 2020). The age range of these samples is from 2.6 to 3.4 Ma that encompasses the MPWP.

Table 3.1: The tie-points for the chronology are from the Knies et al., 2014 and are derived using oxygen isotope stratigraphy (Lisiecki and Raymo, 2005), magnetostratigraphy (Lourens et al., 2005), and biostratigraphy (Sato and Kameo, 1996).

Age (Ma)	910C (mbsf)	Sedimentation rate (cm/kyr)	Datum	Source
2.438	153.38		MIS 96*	Lisiecki and Raymo, 2005
2.510	171.00	24.5	MIS 100 Top	Lisiecki and Raymo, 2005
2.540	175.70	15.7	MIS 100 Base	Lisiecki and Raymo, 2005
2.565	184.67	35.9	MIS 102*	Lisiecki and Raymo, 2005
2.645	204.48	24.8	MIS G2*	Lisiecki and Raymo, 2005
2.830	223.00	10.0	"Datum A"	Sato and Kameo, 1996
3.295	260.40	8.0	MIS M2	Lisiecki and Raymo, 2005
3.596	305.00	14.8	Gauss/Gilbert	Lourens et al., 2005

MIS denotes Marine Isotope Stage, and * means age of heaviest $\delta^{18}O$ value within respective MIS is considered

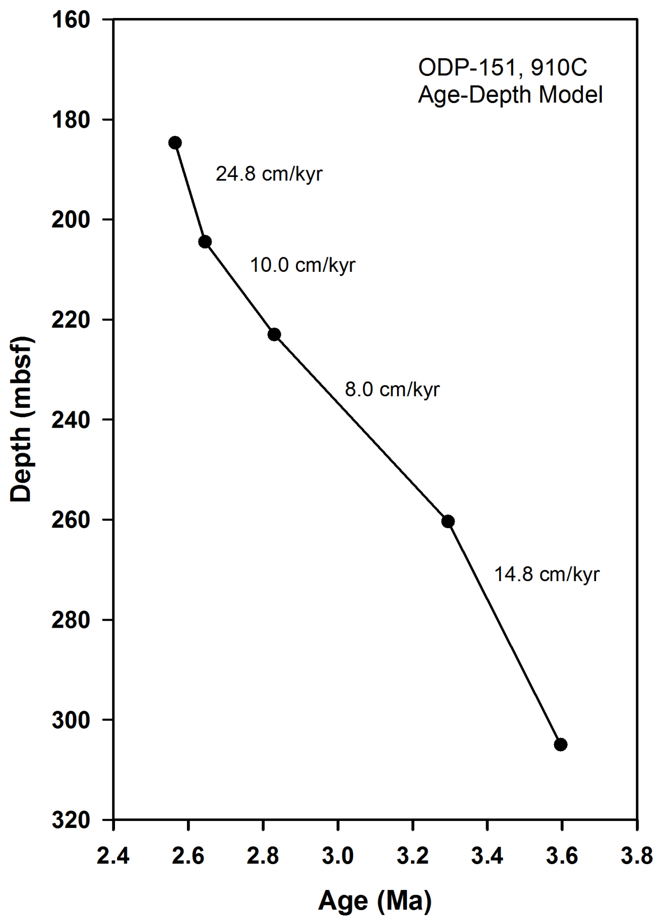

Figure 3.3: The Age-Depth model for the present study constructed using tie points in Table- 3.1 from depth 184.67 to 305.00 mbsf.

3.3.2. Relative Nutrient Utilization and Provenance

The relative nutrient utilization is determined from the nitrogen isotopic ratio of organic matter (δ^{15}N org). The provenance of organic matter is determined through a cross-plot between the total organic carbon to total nitrogen ratio (TOC/TN) and δ^{13}C values of organic matter (δ^{13}C org). We analyzed these parameters from sediments collected from Hole 910C. Around 3 g of freeze-dried sample was ground finely for the homogenization before nitrogen and carbon isotopic ratio (δ^{15}N and δ^{13}C) and total nitrogen and total organic carbon concentration analysis of the sedimentary organic matter. The homogenized samples were divided into two sub-samples for two different analyses - (a) samples were treated with 2N HCl for TOC and δ^{13}C measurement, and (b) untreated samples were used for TN concentration and δ^{15}N analysis because acid treatment has been reported to affect the nitrogen content and isotopic values of the sedimentary organic matter (SOM) (Brodie et al., 2011). The acid treatment removed inorganic carbon from the sediment allowing analysis of TOC and $\delta^{13}C$ of the organic matter. 20 ml of freshly prepared 2N HCl was added to 1-2 g finely ground sediment. The solution was shaken mechanically and kept overnight. After the full settlement of the sediments to the bottom of the beaker, the acid was decanted from the sample. The sample was washed with ultrapure demineralized water until its pH became neutral. Approximately, 5 mg of treated sediment sample was taken for the $\delta^{13}C$ and TOC measurement whereas for $\delta^{15}N$ and TN analysis, around 120 mg of bulk ground sediment was used. The isotopic analysis and elemental concentration were measured by an Isoprime Isotope Ratio Mass Spectrometer coupled with an Elemental Analyzer (Vario Isotope Cube) in Marine Stable Isotope Lab of National Center for Polar and Ocean Research, Goa, India. In the case of $\delta^{13}C$ and TOC, alternate samples were analyzed. The isotopic values are expressed in delta (δ) notation, which is the relative difference of isotopic ratios in the sample from an international standard. Thus, in the case of nitrogen isotopes: $\delta^{15}N = \{(15N/14N)sample/(15N/14N)standard\}-1$; where (15N/14N)sample and (15N/14N)standard are the ratios of the abundances of the less abundant (heavier, i.e., 15N) to more abundant (lighter, i.e., 14N) isotope in the sample and standard, respectively. The $\delta^{15}N$ and $\delta^{13}C$ values are multiplied by 103 and are expressed in per mil (‰). The uncertainties for the $\delta^{15}N$ and $\delta^{13}C$ analysis are ±0.24‰ and ±0.18‰, respectively, based on repeated measurement of the standard reference material IAEA-N1 (ammonium sulphate, n = 43) and IAEA-600 (Caffeine, n = 27). Similarly, the uncertainties for TN and TOC are ±0.81% (n = 81) and ±0.80% (n = 56), respectively, determined using Sulfanilamide as standard.

3.4 Results and Discussion

3.4.1 Provenance of Sedimentary Organic Matter and no Alteration of $\delta^{15}N$

The provenance of SOM is determined from both the C/N ratio and $\delta^{13}C$ values of the SOM. The average value of the marine and terrestrial (C3 plant) organic matter is −21‰ and −27‰, respectively (Ruttenberg & Goñi, 1997). Most of the

$\delta^{13}C$ values observed in the present study are near the marine end member. The C/N ratio of SOM is also widely used to determine the provenance of organic matter. The C/N ratio of marine organic matter ranges from 8 to 10 while it ranges from 20 to 100 in the case of terrestrial organic matter (Meyers, 1994). The higher values of C/N ratio in the terrestrial organic matter are due to the presence of low nitrogen and high carbon content compounds like lignin and cellulose found in the plant cell wall. In the present study, the C/N ratio of the SOM varies from 8 to 12. We further plotted $\delta^{13}C$ versus C/N ratio to determine the provenance (Fig. 3.4). It shows that most of the values are near the marine end-member, so the SOM appears to be mostly of marine origin with a little contribution from the terrestrial organic matter. Myhre et al., 1995, in the initial proceedings of ODP 151, have also shown that the origin of organic matter from 160 to 380 mbsf (meter below seafloor) is predominantly from the marine environment. Nevertheless, to check the effect of the terrestrial organic matter on the $\delta^{15}N$ of the SOM, we plotted $\delta^{15}N$ versus $\delta^{13}C$ (Fig. 3.5a).

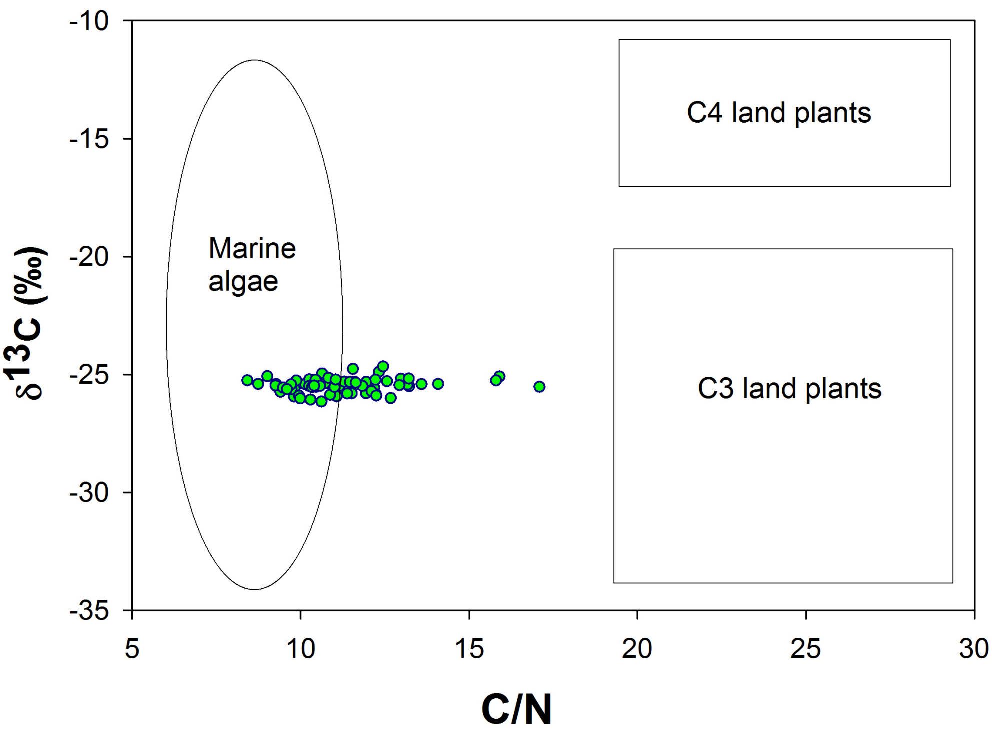

Figure 3.4: The provenance of the sedimentary organic matter determined from $\delta^{13}C$ vs C/N ratio.

The $\delta^{15}N$ values of the terrestrial and marine organic matter are ~4‰ and around 5 -7‰ respectively (Sigman et al., 2009). Thus, both the $\delta^{15}N$ versus $\delta^{13}C$ values of the terrestrial organic matter are lower than the marine counterpart. Hence, if there is any effect of the terrestrial contribution on the $\delta^{15}N$ of the SOM, it should yield a positive correlation between $\delta^{15}N$ and $\delta^{13}C$ of the SOM. In the present study, we do not find any correlation between $\delta^{15}N$ and $\delta^{13}C$ ($r^2 = 0.01$) of SOM (Fig. 3.5a) confirming that the terrestrial contribution does not affect the $\delta^{15}N$ values of SOM significantly. Additionally, the degree of sedimentary $\delta^{15}N$ alteration is a function of oxygen exposure time during the early burial stage (Robinson et al., 2012). The oxygen exposure time is linearly related to the water column depth and sedimentation rate. The time of exposure is generally prolonged in deep-sea due to the slow sedimentation rate. But, in the present study, the water depth is only 556.4 m with a high sedimentation rate (8 – 24 cm/kyr).

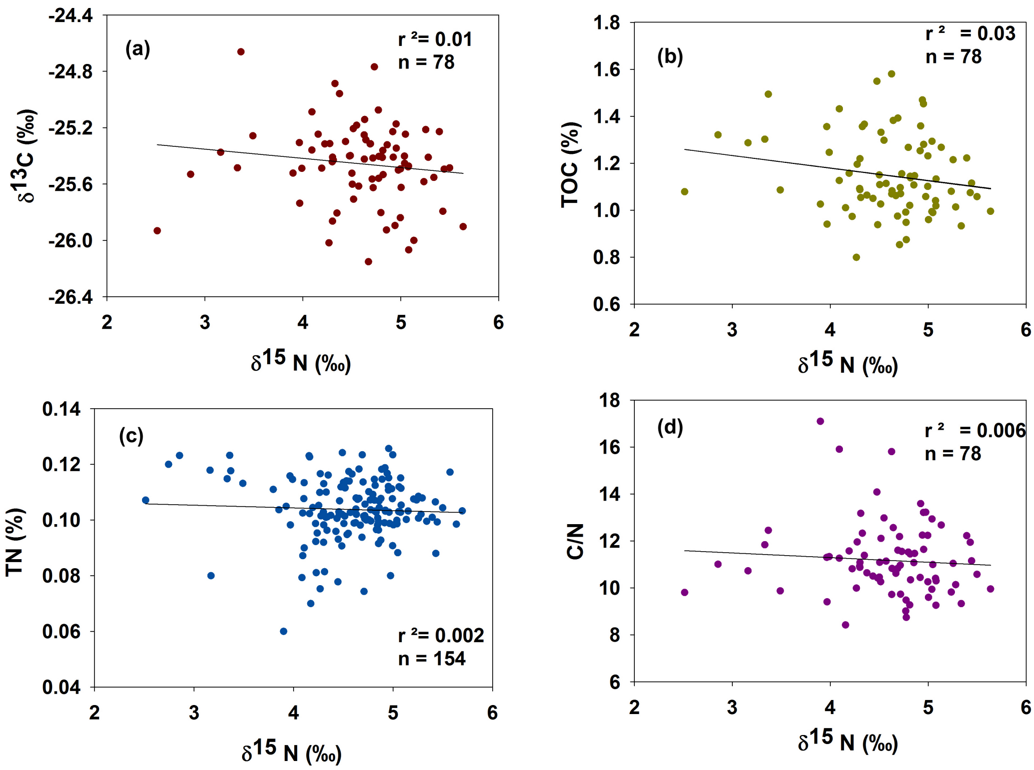

Figure 3.5: (a) The terrestrial contribution to the SOM is tested using $\delta^{15}N$ vs. $\delta^{13}C$. (b, c, and d) The diagenetic degradation on SOM examined using $\delta^{15}N$ vs. TOC, C/N, and TN, respectively.

So, no diagenetic alteration is expected. Still, we checked whether diagenesis has affected the $\delta^{15}N$, TOC, and TN values in the present study. Diagenetic activity increases the $\delta^{15}N$ values while reduces the TOC and TN concentration (Freudenthal et al., 2001). Therefore, if diagenesis has taken place then the $\delta^{15}N$ should exhibit anti-covariance with TOC and TN and covariance with C/N ratio (Tripathi et al., 2017). We do not find any correlation between $\delta^{15}N$ versus TOC, TN, and C/N (r^2 = 0.03, 0.002, and 0.006) (Fig. 3.5b-3.5d) implying there is no effect of diagenetic degradation on SOM in the sediment used in the present study.

3.4.2 Stratification During Mid-Pliocene Interglacial Periods

The MPWP spans 3.264 - 3.025 Ma, which has three major warm periods MIS KM5 (3.20 - 3.19), KM3 (3.18 - 3.16 Ma), and K1 (3.09 - 3.06 Ma) (Haywood et al., 2013; Lisiecki & Raymo, 2005, Fig. 3.6a). Two other interglacials i.e., MIS G7 (2.78 - 2.74 Ma) and MIS G3 (2.7 - 2.66 Ma) follow the MPWP. During these interglacials, the $\delta^{15}N$ values of the organic matter vary between 5.0‰ and 5.7‰ (Fig. 3.6b). The surface water productivity inferred from $CaCO_3$ content and the mass accumulation rate of $CaCO_3$ ($CaCO_3$ MAR) shows an increasing trend during these interglacial periods (Fig. 3.6d). The trace element Ba occurs as barite (BaSO4) in the marine environment related to the organic carbon flux. Barite has higher preservation compared to other productivity proxies like $CaCO_3$ and TOC (Dymond et al., 1992; Gingele et al., 1999). Therefore, Ba is considered as a good proxy for ocean productivity. However, usually, Ba-excess is used, which is the fraction of Ba that is not supplied by terrigenous material and is determined by normalizing Ba by Al.

During interglacials, the open surface water together with nutrient-rich meltwater supply and high river discharge led to higher productivity as recorded by an increase in Ba/Al ratio, the $CaCO_3$ content, and its MAR (Fig. 3.6c and 3.6d). However, the increase in $\delta^{15}N$ values during interglacials indicates high relative nutrient utilization suggesting higher consumption of the available nutrients (Altabet & Francois, 1994; Schubert & Calvert, 2001).

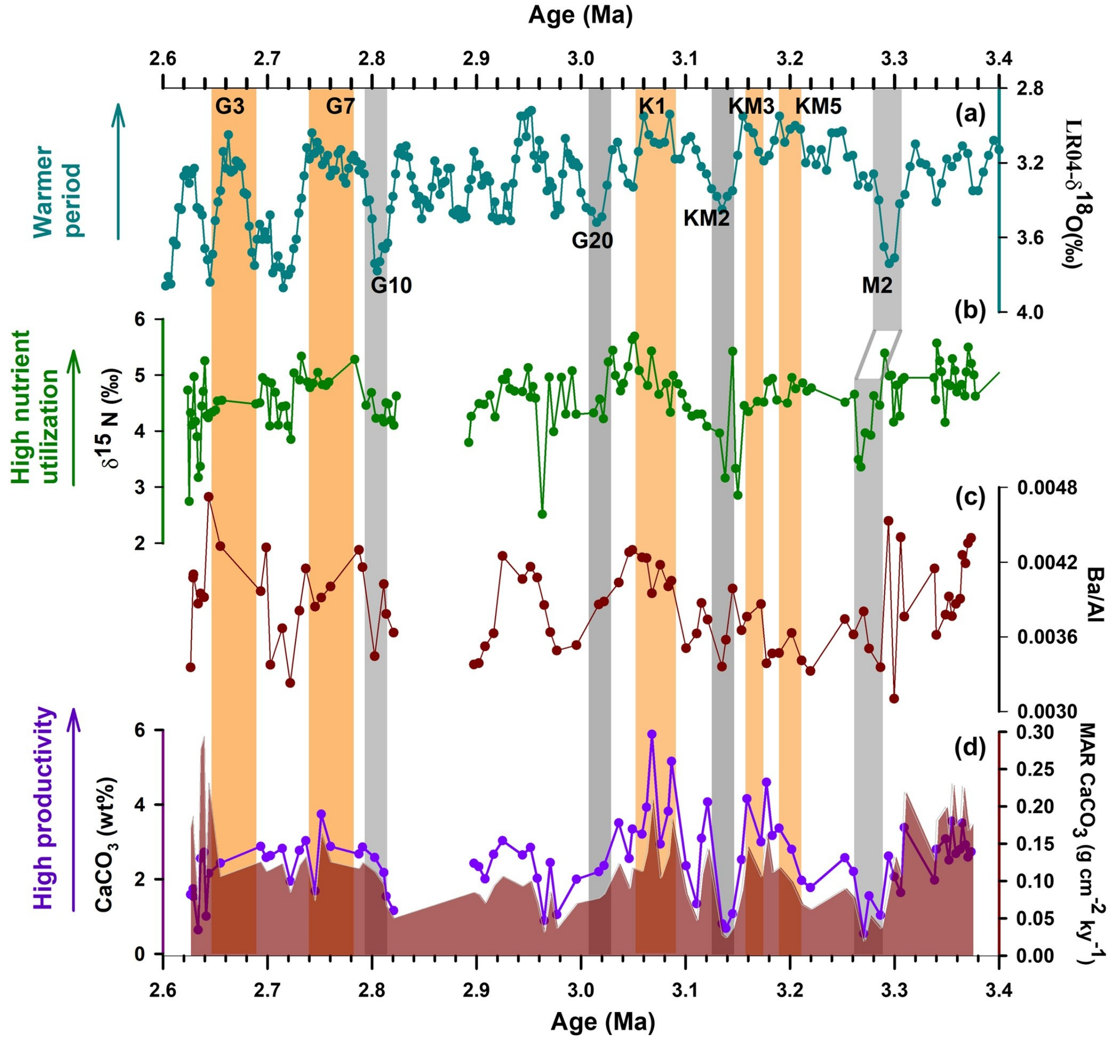

Figure 3.6: Relative nutrient utilization and productivity variability during late Pliocene. (a) LR04 stack of $\delta^{18}O$ (‰) of benthic foraminifera (Lisiecki & Raymo, 2005); (b) $\delta^{15}N$ (‰) representing the relative nutrient utilization during different periods; (c) and (d) Ba/Al, $CaCO_3$ (%) and Mass Accumulation Rate of $CaCO_3$ showing the paleoproductivity variability. Gray bands indicate colder periods while the colored bands show warmer periods. Positions of Marine Isotope Stages M2, KM3, KM2, K1, G20, G10, G7, and G3 are shown.

The enhanced productivity during the warmer periods due to sufficient light availability utilizes more of the available nutrient causing high relative nutrient utilization (high $\delta^{15}N$ values) (Knies et al., 2007; Randelhoff et al., 2015). Additionally, the high relative nutrient utilization suggests that mixing with the deeper nutrient-rich waters was reduced significantly. Similar enrichment of $\delta^{15}N$ values is found in both the central Arctic Ocean during the Holocene (5‰ - 6.8‰, Schubert et al., 2001) and the subpolar region during MIS 5e and MIS 11 interglacials (4.8‰ and 5.2‰, Thibodeau et al., 2017). This increase in relative nutrient utilization during warmer periods is attributed to lower nutrient conditions because of a thinner surface mixed layer due to enhanced stratification. This inference corroborates modern summer observations where the surface nitrate concentration appears to be low in the study region (Fig. 3.2d). The reduction of the surface mixed layer is supported by the instrumental data (30 years) from the Arctic Ocean, which indicates a shoaling of the mixed layer in the order of 0.5 - 1 m/year and thus increased water mass stratification (Peralta-Ferriz & Woodgate, 2015). The low saline surface waters are well separated from the deep waters causing a restriction in nutrient exchange (Fig. 3.2d and 3.2e) and thus high nutrient utilization manifested through high $\delta^{15}N$ (5‰ - 7‰) values in surface sediments (Knies et al., 2007; Schubert & Calvert, 2001). Hence, we propose that high $\delta^{15}N$ values during interglacials observed in Hole 910C likely suggest enhanced stratification during warmer periods during the MPWP in the AAG.

The factors that melt sea ice are both the summer solar heating (Perovich et al., 2011) and the inflow of warm water from both the Pacific and Atlantic Ocean (Carmack et al., 2015; Polyakov et al., 2017). Data from ODP holes 909A and 911A indicate that despite discrepancies in sea surface temperatures (SST) values ranging from 12°C to 18°C, both records show generally higher SSTs at Yermak Plateau during the late Pliocene compared to the present (Knies et al., 2014; Robinson, 2009). The data also corroborates observations from the North Atlantic region (ODP 982) suggesting an increase of SST during warmer periods of MPWP (Fig. 3.7d; Lawrence et al., 2009). The warmer and open water conditions during this period at the study site are also supported by summer sea ice-free conditions inferred from reduced abundance of sea ice proxy IP25, and open water proxy HBI III (Fig. 3.7c) as well as less influx of ice-rafted debris (Fig. 3.7f) (Knies et al., 2002, 2014; Rahaman et al., 2020). Another earlier study observed ice-free summers, and probably a perennially ice-free Arctic Ocean during the MPWP due to the inflow of warm Atlantic water into the Arctic Ocean through the Fram Strait (Cronin et al., 1993). A recent high-resolution study from the same site (910C, Yermak Plateau) found less radiogenic neodymium isotope (low εNd) during warmer periods of MPWP (Fig. 3.7b) indicating a significant inflow of warm and saline Atlantic water into the Arctic (Rahaman et al., 2020). Comparison of εNd and δ^{15}N org suggests that the enhanced NAC to the Arctic could have played a major role in strengthening the stratification, which led to high relative nutrient utilization (Fig. 3.7a and 3.7b).

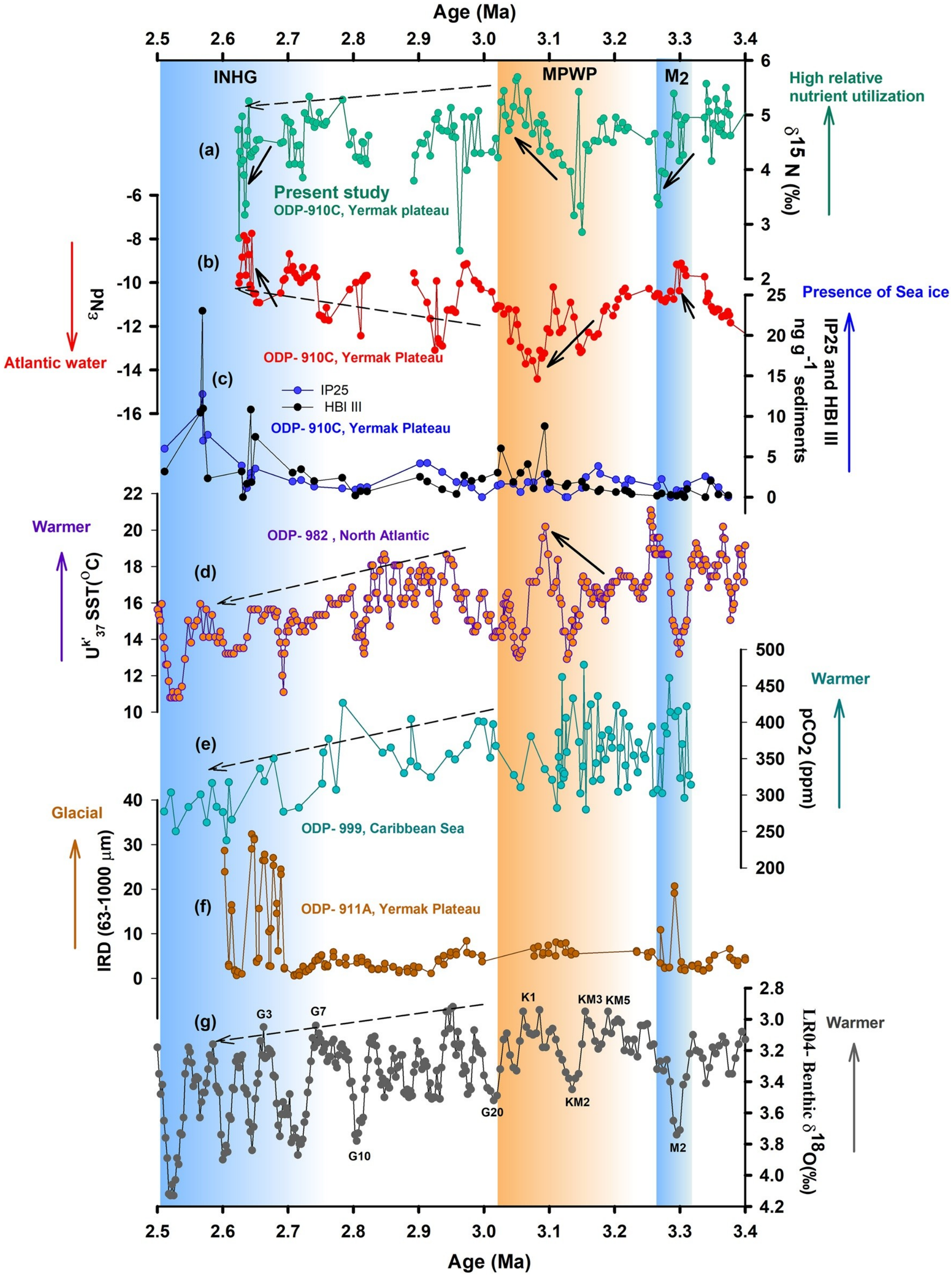

Figure 3.7: Comparison of relative nutrient utilization with sea surface temperature (SST), Atlantic water inflow, and sea ice extent. (a) $\delta^{15}N$ record from ODP-910C (present study) shows the relative nutrient utilization; (b) and (c) Authigenic εNd record and sea ice proxy (IP25) with open water biomarker Highly Branched Isoprenoid III from 910C (Rahaman et al., 2020); (d) SST record from the ODP Site 982 (North Atlantic) using Alkenone UK37 (Lawrence et al., 2009); (e) Atmospheric CO2 concentration reconstructed using $\delta^{11}B_{borate}$ of G. ruber from ODP site 999, Caribbean Sea (de la Vega et al., 2020); (f) IRD record from the ODP Site 911A (Yermak Plateau, Knies et al, 2014); (g) LR04 stack of $\delta^{18}O$ (‰) of benthic foraminifera (Lisiecki & Raymo, 2005). Dashed arrows show long term trend from 3.1 to 2.6 ma and solid arrow indicates glacial-interglacial trends.

This enhanced NAC transported heat to the polar region, which could have amplified the Arctic temperature during MPWP (Dowsett et al., 1992). The warmth caused an increase in the river runoff, sea ice melt, and precipitation during interglacials, which could have strengthened the stratification during MPWP further. We propose that the higher sea ice melt and freshwater influx along with enhanced NAC during warmer periods of MPWP including MIS G3 and G7 would have contributed to the enhanced stratification at the Yermak Plateau (shown pictorially in Fig. 3.9a).

3.4.3 Stratification During Mid-Pliocene Glacial Periods

The increase in $\delta^{18}O$ value from 3.1‰ to 3.7‰ (Lisiecki & Raymo, 2005) between 3.33 and 3.31 Ma marks the colder event termed as MIS M2 glacial period (Fig. 3.6a). It is a large global glaciation that lasted for 50 kyr and interrupted the trend of global warming at 3.3 Ma. One hypothesis to explain the cooling is that the opening of the Central American Seaway (CAS) resulted in the weakening of the AMOC and NAC leading to less heat transport towards the polar region causing the M2 glaciation (De Schepper et al., 2013). Tan et al., 2017, suggests that the opening of CAS helps in the reduction of northward heat transport but can not alone explains the onset of M2 glaciation. They proposed that the reasons for the M2 glaciation were the presence of the shallow open CAS with other factors like favorable orbital parameters, decrease in CO2 concentration (220 ppmv), vegetation albedo, and ice sheet feedback that led to the sea ice buildup in northern high latitudes. In the present study, the MIS M2 glacial period corresponds to the lower $\delta^{15}N$ value (shown by the tilted gray band in Fig. 3.6), which decreased from 5.4‰ to 3.4‰. An exact match at M2 is not observed, possibly, due to the different chronologies of the LR04 and our record and their inherent chronological errors. The high $\delta^{15}N$ values observed at 3.3 Ma could be the result of interglacial before M2 glacial period. Other glacial periods (i.e., KM2, G20, and G10) are also marked by the increase in $\delta^{18}O$ values and low $\delta^{15}N$ values (Fig. 3.6b). Surface water productivity indicators ($CaCO_3$, $CaCO_3$ MAR, and Ba/Al) decreased to a minimum during these colder periods (Fig. 3.6c and 3.6d). The enhanced sea ice cover during these colder periods could have caused light limitations and hence lower surface productivity com- pared to interglacial periods. The low $\delta^{15}N$ values during these colder periods represent low relative nutrient utilization at the Yermak Plateau implying eutrophic conditions and potentially a thickening of the polar mixed layer causing mixing with nutrient-rich water (Rudels et al., 1991). Schubert et al., 2001 also reported low relative nutrient utilization (low $\delta^{15}N$) and low productivity due to the perennial sea ice cover during the Last Glacial Maximum (LGM) in the central Arctic Ocean. It suggests the replenishment of nutrients at the surface is due to the low stratification and enhanced mixing of deep-water nitrate source. The high nitrate concentration in the surface water is also supported by the observations during the modern winter period where nitrate concentration reaches up to 11 µmol/L with a low salinity gradient at the study site (Fig. 3.2a).

Hence, we suggest that during the glacial periods of the MPWP, the reduction of Atlantic water inflow into the Arctic Ocean expressed by high εNd, values (Fig. 3.7b; Rahaman et al., 2020) are likely responsible for the weaker stratification of the surface waters. We postulate that the associated enhanced sea ice formation reduced the stratification and increased the mixing thickness of PML during the colder periods of MPWP leading to less nutrient utilization (shown pictorially in Fig. 3.9b).

On considering the long-term trends from ~3.0 to 2.6 Ma (dashed arrows in Fig. 3.7), we note a reduction of CO2 concentration (de la Vega et al., 2020, Fig. 3.7e) and SST at the Atlantic Ocean (Fig. 3.7d) representing a long-term cooling. This long-term cooling coincides with the reduction of NAC inflow to the Arctic Ocean as evident from the gradual increase in εNd values at the Yermak Plateau (Fig. 3.7b). The cooling matches with the modest decrease in $\delta^{15}N$ values of SOM towards INHG, which indicates the decrease in relative nutrient utilization and thus low stratification at AAG. Thus, the changes that occurred during the individual glacial periods match with the changes occurring during the long-term increase in glaciation.

3.4.4 Forcing Factor of the Arctic Stratification

Stratification in the Arctic Ocean is governed by both sea ice dynamics and river discharge. These could have been affected by both internal (i.e., Ocean-Atmosphere interactions, land-air interaction, and atmospheric internal dynamics) as well as external forcings (i.e., orbital). To identify the forcing factors of the Arctic stratification, we compared the relative nutrient utilization with the eccentricity as well as the solar insolation variability in the Northern hemisphere during the summer season (from 65°N and July month) (Fig. 3.8a). We find that strong stratification (high $\delta^{15}N$ values) coincides with strong solar radiation and high eccentricity. We also carried out the spectral analysis and the continuous wavelet transform to look at the major forcing factor of the nutrient utilization variability in the Arctic Ocean. The resolution of the $\delta^{15}N$ time series is uneven. To resolve this issue, we have used Piecewise Cubic Hermite Interpolation to make the data set evenly spaced. They show a significant periodicity of around 130 kyr (Fig. 3.8b and 3.8c). It matches closely with the eccentricity cycle, which possesses periodicities near 95 and 125 kyr (Laskar et al., 2004). The obliquity and precession cycles are also present though they are not significant (Fig. 3.8). The resolution of the data set ranges from 5 to 11 kyr with an average sampling resolution of ~8,000 years, which allowed us to capture the obliquity and precession cycles (Fig. 3.8). Thus, the dominant forcing factor is the eccentricity cycle. However, the same orbitally paced control (e.g. eccentricity cycle) is observed in oceanic heat inflow into the Arctic (Rahaman et al., 2020). It suggests that enhanced inflow of NAC to the Arctic and the high relative nutrient utilization during warmer periods including MPWP follows the eccentricity cyclicity. The cross wavelet analysis (Fig. 3.8e) shows the common highest power between these two time-series. We have multiplied the εNd data with -1 so that it follows the same trend with the $\delta^{15}N$ values without changing the interpretation of water mass circulation. The right-pointing arrows from 3.15 to 2.9 Ma at the eccentricity band show in-phase relation between the enhanced inflow of NAC and the strong stratification (Fig. 3.8e). This result implies that the interglacials with high eccentricity and strong solar insolation in Northern Hemisphere may have resulted in the reduction of sea ice cover. Further, the closure of Arctic gateways (Bering Strait and the Canadian Arctic Archipelago) during MPWP strengthened the AMOC (Otto-Bliesner et al., 2017; Zhang et al., 2020) that could have further enhanced the North Atlantic current to the Arctic that increased the heat transport and subsequent stratification and sea ice melt.

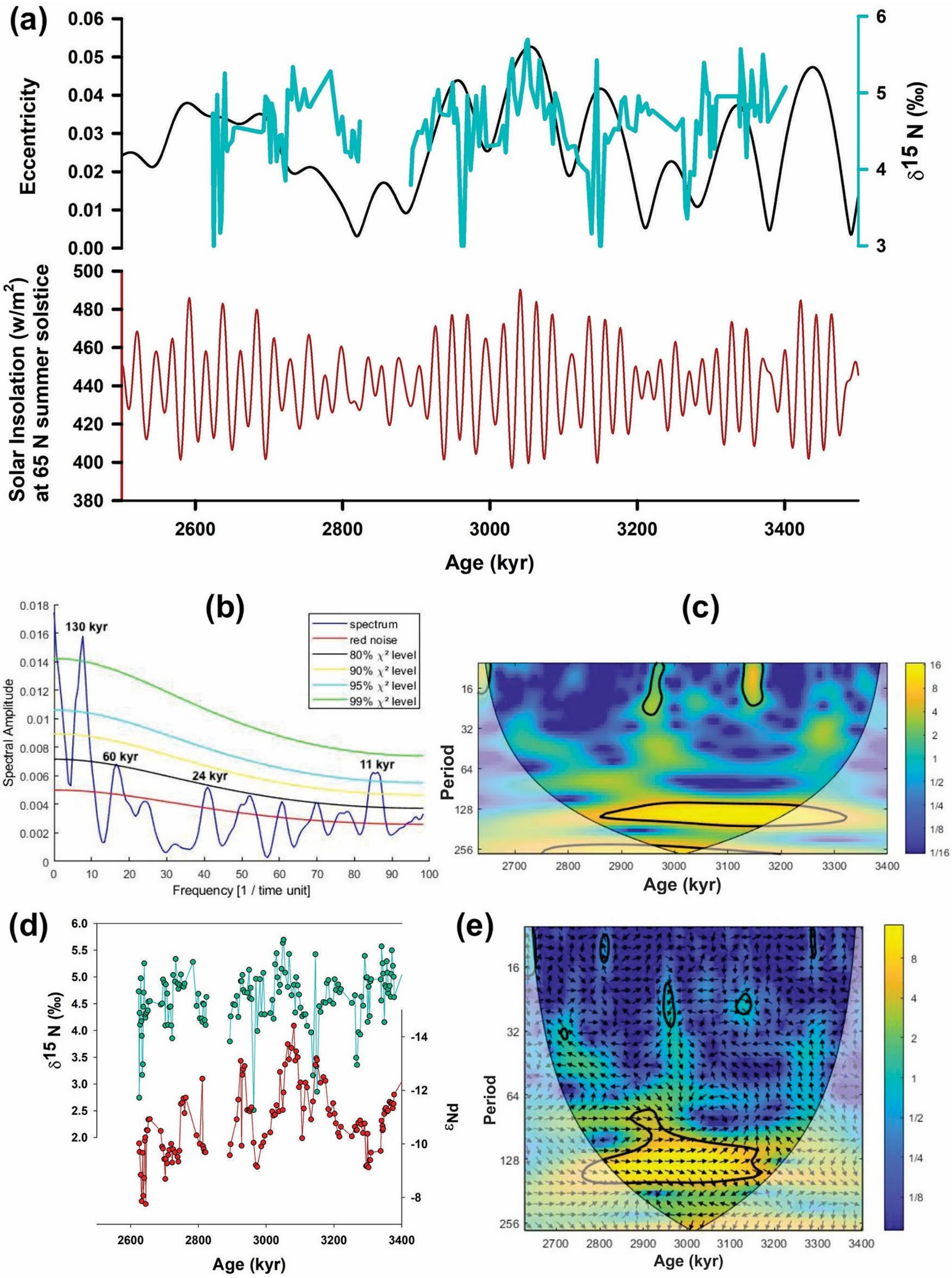

Figure 3.8: Correlation between orbital forcing and the relative nutrient utilization related to Arctic stratification. (a) Comparison of eccentricity and insolation cycles (Berger & Loutre, 1991) with relative nutrient utilization; (b) and (c) show spectral analysis and continuous wavelet transform for relative nutrient utilization; (d) Comparison between $\delta^{15}N$ (‰) values with authigenic εNd indicate that stratification increases during the episodes of enhanced inflow

of NAC to the Arctic Ocean; (e) Cross wavelet analysis of two time-series representing Arctic stratification and North Atlantic Current (NAC) inflow indicating the common highest power. The thick black contour represents the 5% significance level against red noise. The area between the black thin line and the time axis represents the cone of influence. Arrows pointing towards the right show in-phase relation.

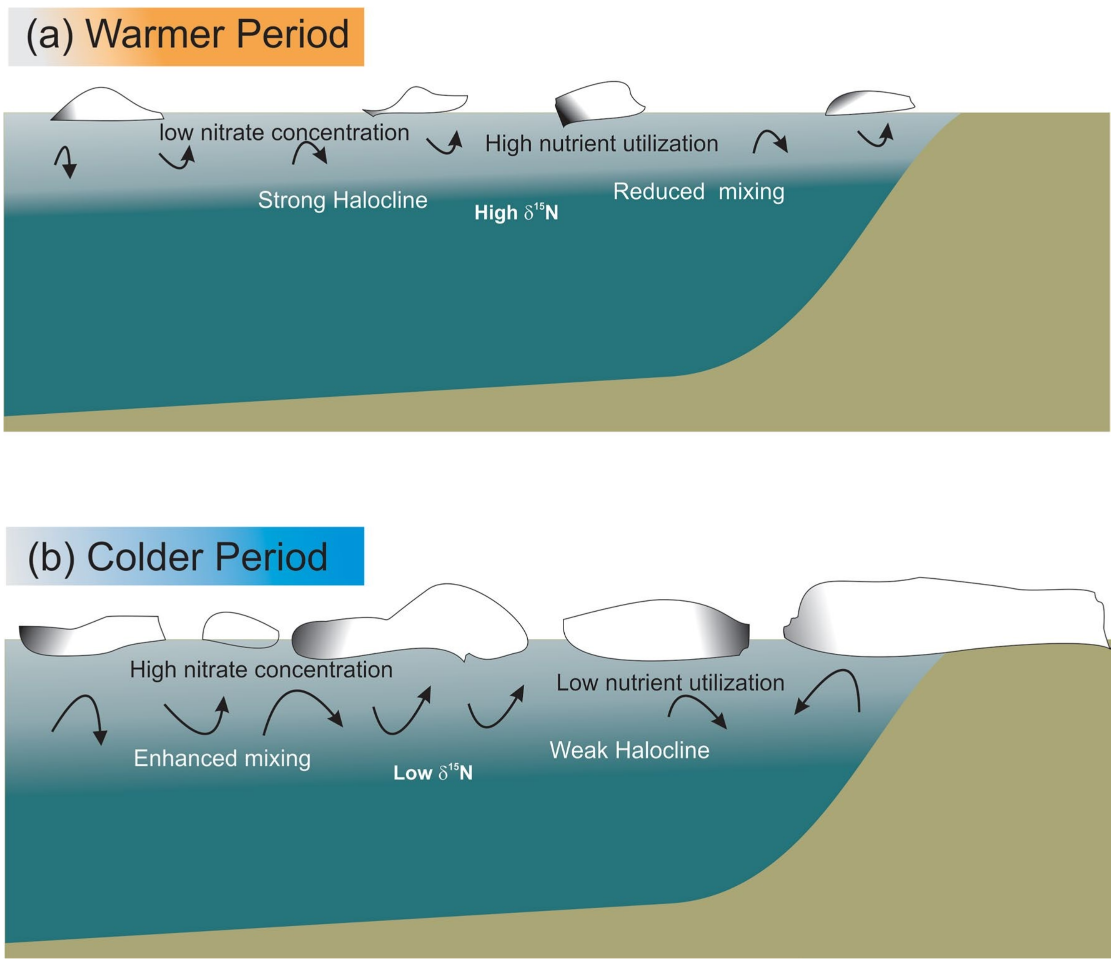

Figure 3.9: Conceptual representation of stratification at the core site during the late Pliocene. (a) The warmer period is characterized by less sea ice cover at the top (open ocean condition). Fresher surface water is separated from the more saline intermediate water. The reduced mixing is denoted by smaller arrow marks. The stronger stratification inhibits the supply of nutrients to the surface, which results in a high $\delta^{15}N$ value; (b) The colder period is having more sea ice cover at

the surface. The brine rejection during the formation of sea ice causes high saline upper surface water. It breaks the stratification formed due to the salinity gradient and causes deeper mixing. Enhanced mixing is represented by bigger arrow marks. It provides nutrients to the surface and which results in a low $\delta^{15}N$ value.

3.5 Conclusions

We find high relative nutrient utilization in the AAG region indicating low nutrient concentration in the mixed layer during the late Pliocene warm periods including the MPWP. Such oligotrophic conditions developed in response to maximum utilization of available nutrients with no replenishment due to enhanced stratification. The stratification strengthened due to the higher sea ice melt, river discharge, and NAC in- flow. Enhanced stratification parallels higher productivity because of sufficient light availability during relatively more ice-free conditions of interglacials. In contrast, low relative nutrient utilization occurred during late Pliocene glacial periods implying high nutrient supply due to reduced stratification and enhanced ocean mixing. The water column stratification variability is predominantly controlled by the eccentricity cycle. Our results imply that during the current scenario of global warming, the enhanced sea ice melt and its internal positive feedbacks can cause strong stratification and upper layer freshening in the near future.

Chapter 4

South Asian Monsoon variability and Arctic sea ice extent linkages during late Pliocene - a modern-like warm period

4.1 Introduction

The South Asian Monsoon (SoAM) forms the backbone of the economy of South Asia and is expected to change adversely due to global warming. Therefore, understanding its variability and forcing factors including various teleconnections on different timescales is important. Climate variability of northern high-latitudes has been proposed to influence the SoAM strength via various pathways. Earlier studies have mostly looked at the linkages between North Atlantic Oscillation/ Atlantic Multidecadal Oscillation using observational analysis (Goswami et al., 2006; Krishnamurthy and Krishnamurthy, 2016). However, the linkages of monsoon variability with the Arctic sea ice extent (SIE) are not explored fully yet. It attains special significance in the current scenario of global warming as the Arctic SIE is declining rapidly with an increase in the earth's temperature (Fox-Kemper et al., 2021). A few recent studies based on short time series analysis indicate a connection between the Arctic sea ice extent and SoAM (Krishnamurti et al., 2015; Grunseich and Wang, 2016; Chatterjee et al., 2021). But such studies are based on very short time series data spanning a few decades and, therefore, need to be ascertained on longer timescales. More insights into the teleconnection between Arctic SIE and SoAM can be had by studying past periods of warmth and CO_2 concentration as expected in near future. Most of the earlier paleoclimatic studies looking at teleconnection between the Indian monsoon and the high-latitude climate span only the last glacial period (Schulz et al., 1998; Altabet et al., 2002; Tiwari et al., 2006, 2021; Kumar et al., 2021 and references therein) primarily due to unavailability of longer records. They, therefore, do not cover the climate having similar temperature and greenhouse gasses concentration as expected in near future.

The mid-Piacenzian Warm Period (MPWP) from 3.264 to 3.025 Ma (million years ago) was warmer than present (Dowsett et al., 2009; Dowsett et al., 2019; Haywood et al., 2020) with similar or higher CO_2 concentration (365 to 415 ppmv; Bartoli et al., 2011; Berends et al., 2019) and annual global mean surface temperature higher by 2.7 - 4.0 ºC (Haywood et al., 2013). As per the IPCC AR6, this is similar to the range projected under the middle-of-the-road Shared Socioeconomic Pathway "SSP2-4.5" for the end of the 23rd century (2.3 - 4.6 °C).

During MPWP, the sea level was higher by approximately 20 m than the present (Rohling et al., 2014) with a similar land-sea distribution. Therefore, the MPWP is considered a climatic analog to the modern world and provides an opportunity to study the effects of global warming. This warm period is followed by a slow descent into lower global temperature known as the "Intensification of the Northern Hemisphere Glaciation" (INHG). The importance of understanding the Inter-Tropical Convergence Zone (ITCZ) variability and its forcings during MPWP is amply stressed in previous studies (e.g., Schneider et al., 2014; Douville and John, 2021). Studying the SoAM variability and its teleconnection with Arctic SIE during the late Pliocene including the MPWP can help to understand the future SoAM variability in a global warming scenario. Our study aims to reconstruct the SoAM variability from the eastern Arabian Sea during the late Pliocene using surface productivity and denitrification records and explore its teleconnections with the Arctic SIE.

4.2 Materials and Methods

4.2.1 Study Site and Chronology

Site U1456 (16°37.28′N, 68°50.33′E, water depth: 3640 m) is drilled in the Laxmi Basin located in the eastern part of the Arabian Sea during IODP expedition 355.

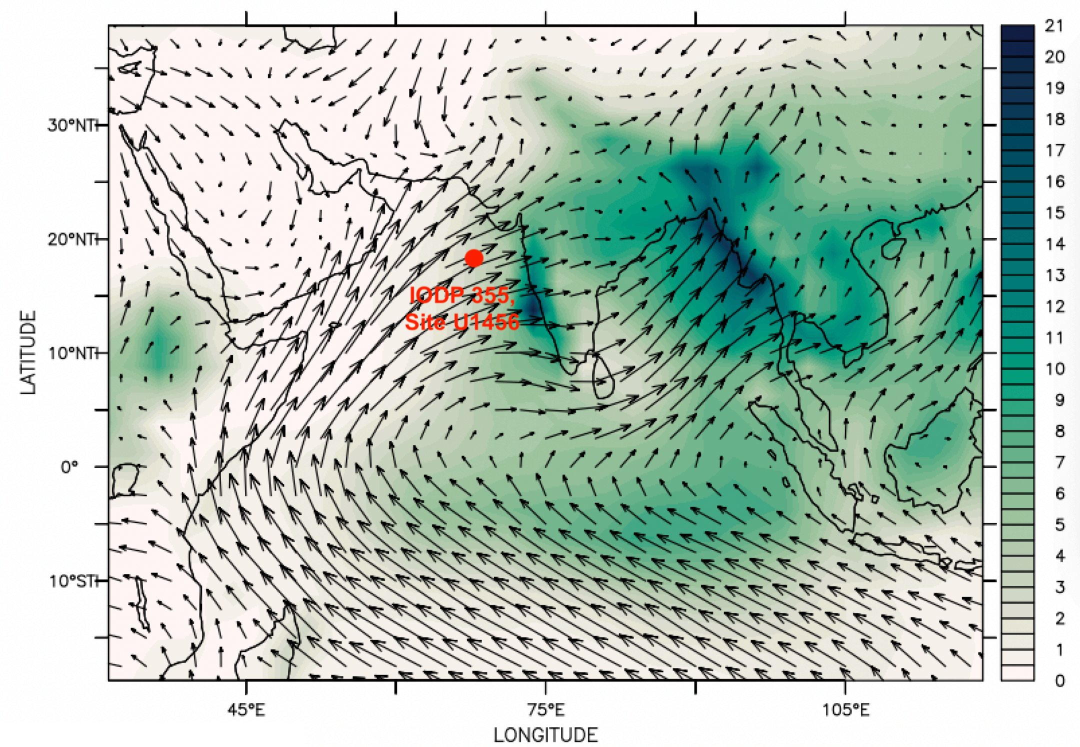

Figure 4.1: The location of IODP 355 Site U1456 (16°37.28´N, 68°50.33´E) is shown by a closed circle. The wind fields are plotted using NCEP/NCAR Reanalysis data. Vector shows the direction of prevailing winds and the color shading represents the intensity of monsoon during the summer season.

The site is located ~ 475 km west of the Indian coast and ~ 820 km south of the modern mouth of the Indus River (Fig. 4.1). A total of five holes were cored at Site U1456 (U1456A-U1456E), with the deepest (Hole U1456E) reaching 1109.4 m below seafloor (Pandey et al., 2016). A core composite depth below seafloor (CCSF) was constructed to develop a common depth scale for all the holes using stratigraphic correlation during the expedition (Pandey et al. 2016). We used samples from 378.53 to 430.3 m (CCSF). The age of the samples range from ~2.7 to 3.4 Ma that spans the late Pliocene including the MPWP. The chronology of the site is based on calcareous microfossil biostratigraphy and magnetostratigraphy and is discussed in detail in Routledge et al., 2019.

4.2.2 Nitrogen and carbon concentration and isotope ratio analysis

Around 4 g of sample was dried and powdered to analyze the nitrogen and carbon isotopic ratio ($\delta^{15}N$ and $\delta^{13}C$) alongside total nitrogen (TN) and total organic carbon (TOC) concentration of the sedimentary organic matter (SOM). The samples were sub-divided into two parts for further treatment. One batch of the sample was treated with 2N HCl to remove the inorganic carbon from the sediment. The other batch was kept untreated for $\delta^{15}N$ and TN concentration analysis because the acid treatment can influence the $\delta^{15}N$ values of the SOM (Brodie et al., 2011). Around 10 mg of the treated sample was used for $\delta^{13}C$ and TOC measurement and around 110 mg of untreated sediment sample was taken for $\delta^{15}N$ and TN concentration analysis. The isotopic analysis and elemental concentrations were measured by an Isoprime Isotope Ratio Mass Spectrometer (IRMS) coupled to an Elemental Analyzer (Vario Isotope Cube) in the Marine Stable Isotope Lab of National Centre for Polar and Ocean Research, Goa, India. The isotopic ratios are denoted by delta (δ) values, which represent the relative difference of isotopic ratios of the samples from the international standard. Thus, $\delta^{15}N = \{(15N/14N)_{sample}/(15N/14N)_{standard}\}-1$. The δ values are multiplied by 10^3 and are expressed in per mil (‰) for the ease of comprehension and readability. The uncertainties for $\delta^{15}N$ and $\delta^{13}C$ analysis are ± 0.16 ‰ and ± 0.28 ‰, respectively, based on the repeated analysis of international standards IAEA-N1 (ammonium sulfate, n = 49) and IAEA-600 (Caffeine, n = 70), respectively. Similarly, the analytical precision for TN and TOC are ± 0.89 (n = 76) and ± 0.69 (n = 84), respectively, determined using sulfanilamide as the standard.

4.3 Results and Discussion

4.3.1 Evaluating provenance and diagenesis of SOM

The C/N ratio and $\delta^{13}C$ values of the SOM can indicate its provenance. The SOM of marine origin has a C/N ratio from 8 to 10 and an average $\delta^{13}C$ value of -21‰ (Meyers et al., 1994; Ruttenberg & Goni, 1997). The terrestrial organic matter possesses a C/N ratio from 20 to 100 and an average $\delta^{13}C$ value of -27‰ (Meyers et al., 1994; Ruttenberg & Goni, 1997). We note that the C/N ratio varies from 5 to 15 and the $\delta^{13}C$ values range from 18‰ to 23‰ in the present study. We plotted the $\delta^{13}C$ versus C/N ratio to determine the provenance of the SOM (Fig. 4.2).

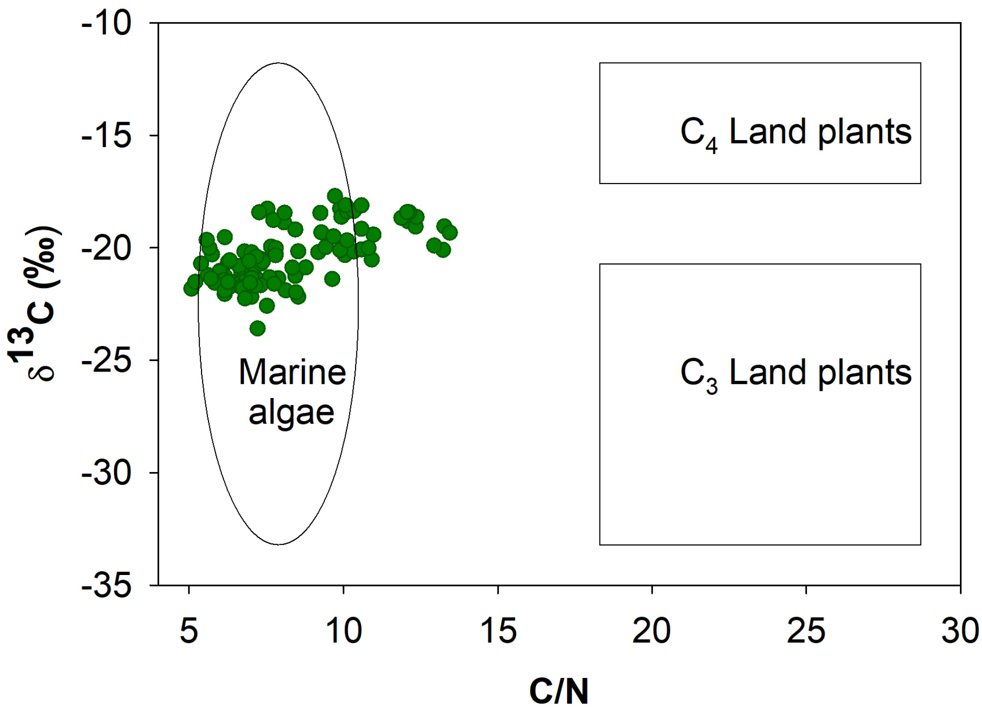

Figure 4.2: Provenance of the sedimentary organic matter is determined from $\delta^{13}C$ vs C/N ratio from the eastern Arabian Sea.

It shows that the maximum values belong to the marine algae range, which suggests the SOM is mostly of marine origin. However, there can be some contribution from the terrestrial region as a few values fall outside the marine algae range. Therefore, it needs to be checked for any effect of terrestrial contribution on the $\delta^{15}N$ values. The $\delta^{15}N$ values of marine and terrestrial organic matter are around 5-7‰ and 4‰, respectively. As both the $\delta^{13}C$ and $\delta^{15}N$ values of the terrestrial organic matter are lower than the marine counterpart, the $\delta^{15}N$ values should have a positive correlation with the $\delta^{13}C$ values. We find a poor correlation between $\delta^{13}C$ and $\delta^{15}N$ ($r^2 = 0.35$) indicating that terrestrial organic matter has a negligible effect on the $\delta^{15}N$ values (Fig. 4.3a).

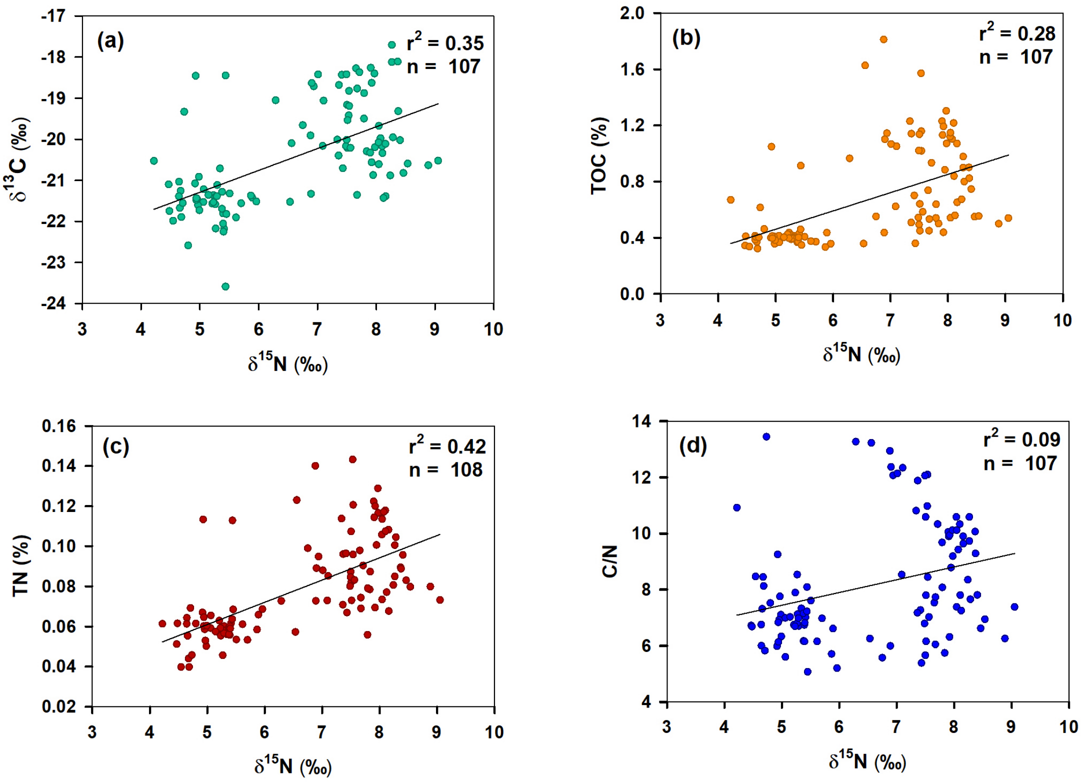

Figure 4.3: (a) The effect of the terrestrial contribution at the study site is determined from $\delta^{15}N$ vs. $\delta^{13}C$. (b, c and d) Diagenesis and alteration after deposition of the organic mater is examined from $\delta^{15}N$ vs. TOC, TN and C/N, respectively.

In the present study, the sediment core has been collected from a depth of 3640 m where diagenesis after deposition of the organic matter is possible. Therefore, we have evaluated whether the diagenesis has affected the $\delta^{15}N$, TOC, and TN values of the SOM. During diagenesis, the $\delta^{15}N$ values of the organic matter increase while the elemental concentration of the SOM (TOC and TN) decreases (Freudenthal et al., 2001). Therefore, diagenesis of SOM shall result in a negative correlation between $\delta^{15}N$ values and elemental composition and a positive correlation between $\delta^{15}N$ values and the C/N ratio. In the present study, the $\delta^{15}N$ versus TOC (r^2 = 0.28) and TN (r^2 = 0.42) shows a positive correlation (Fig. 4.3b, 4.3c), while we do not find any relation between the $\delta^{15}N$ and C/N ratio (r^2 = 0.09, Fig. 4.3d). It implies that there is no diagenetic alteration of SOM at the present study site.

4.3.2 South Asian Monsoon (SoAM) variability during late Pliocene

The denitrification and the surface productivity records span 3.4 Ma to 2.7 Ma, representing four distinct intervals i.e., I (2.7 - 2.9 Ma), II (2.9 - 3.05 Ma), III (3.05 - 3.2 Ma), and IV (3.2 - 3.4 Ma) as shown in Fig. 4.4. The $\delta^{15}N$ values of the organic matter vary between ~ 4.5 to 9 ‰ (Fig. 4.4a). During interval IV, the $\delta^{15}N$ values range from 6.5 to 4.5 ‰ indicating low denitrification and then it increases to ~9 ‰ at the beginning of MPWP (~3.22 Ma). The $\delta^{15}N$ values stay high during the MPWP (interval III, Fig. 4.4a) indicating strong denitrification. The $\delta^{15}N$ value then decreases to ~6‰ at ~3.06 Ma and continues till 2.9 Ma, indicating low denitrification in interval II. Thereafter, the $\delta^{15}N$ value increases till 2.7 Ma, indicating high denitrification (Fig. 4.4a). The TOC and TN content of the SOM can indicate the surface water productivity in the eastern Arabian Sea. The TN content of the SOM varies from 0.04 to 0.16 % (Fig. 4.4c). During intervals IV and II, the TN content ranges from 0.04 to 0.07 % that indicates low productivity, while during intervals III and I, the TN content increases from 0.08 to 0.15 % indicating high productivity in the eastern Arabian sea. Similarly, the TOC content of the organic matter is low during intervals IV and II and varies from 0.4 to 0.7 % (Fig. 4.4b). However, during intervals III and I, the TOC content shows higher values from 0.4 to ~1.6 %. Overall, the TN and the TOC content suggest low productivity during intervals IV and II, and high productivity during interval III (MPWP) and I.

The SoAM variability is reconstructed using multiple proxies of surface water productivity (TOC and TN) and denitrification ($\delta^{15}N$) from the eastern Arabian Sea supported by a chemical weathering proxy (K/Al; Sarathchandraprasad et al., 2021) (Fig. 4.4d). The monsoon-induced productivity and ventilation via intermediate water masses are the main control of water column denitrification in the Arabian Sea (Pichevin et al., 2007). Previous studies show that the degree of denitrification in the Arabian Sea fluctuates in response to the SoAM activity on various timescales (Altabet et al., 1995; Suthhof et al., 2001; Ziegler et al., 2010). A 10-million-year long record of denitrification from the same IODP site determined the SoAM variability from late Miocene to the present based on denitrification variability supported by productivity fluctuations at a coarse resolution (Tripathi et al., 2017). In the present study, the denitrification record matches with surface productivity and chemical weathering variability caused by SoAM. It suggests that the water column denitrification can indicate the SoAM variability on such long timescales. We find high denitrification and surface productivity along with high chemical weathering during intervals III and I. In contrast, low denitrification and surface productivity along with low chemical weathering is observed during intervals IV and II. It suggests that the SoAM intensified during interval III (MPWP, 3.05 - 3.2 Ma). Earlier studies from the eastern Arabian Sea (Tripathi et al., 2017; Sarathchandraprasad et al., 2021) and the South China Sea (Zhang et al., 2009) support the intensification of SoAM during the MPWP. Further, the SoAM enhanced during interval I (2.7 - 2.9 Ma) and weakened during interval IV (3.2 - 3.4 Ma) and II (2.9 - 3.05 Ma).

4.3.3 Forcing factors of South Asian Monsoon during late Pliocene: Role of Arctic sea ice extent variability

Pliocene Model Intercomparison Project Phase 2 (PlioMIP2) ensemble study shows that 'dynamical effects' are more important than the 'thermodynamical effects' in affecting the monsoonal precipitation (Han et al., 2021). The thermodynamical effect results in enhanced moisture carrying capacity because of enhanced warmth that increases precipitation. For example, the pCO_2 variability causes a thermodynamical effect by changing the global temperature. Dynamical effects, on the other hand, cause changes in the meridional transport of heat and mass leading to the northward movement of ITCZ and therefore higher SoAM precipitation during warm periods. For example, changes in temperature over the northern tropics over 'Indian Low' or southern tropical Indian Ocean (Mascarene High) can change the cross-equatorial pressure gradient and influence the ITCZ position. Arctic SIE variability has been identified recently to affect the SoAM via asymmetric inter-hemispheric energy export and through modulation of the jet stream and meridional circulation (Schneider et al., 2014; Chatterjee et al., 2021). To validate and get more insight into such remote teleconnections, we require longer time series data. An opportunity is presented to do so by the recent reconstruction of spring sea ice concentration during the late Pliocene (Rahaman et al., 2020). The various thermodynamical and dynamical effects influencing SoAM variability along with probable mechanisms during various intervals identified in the present study are discussed below.

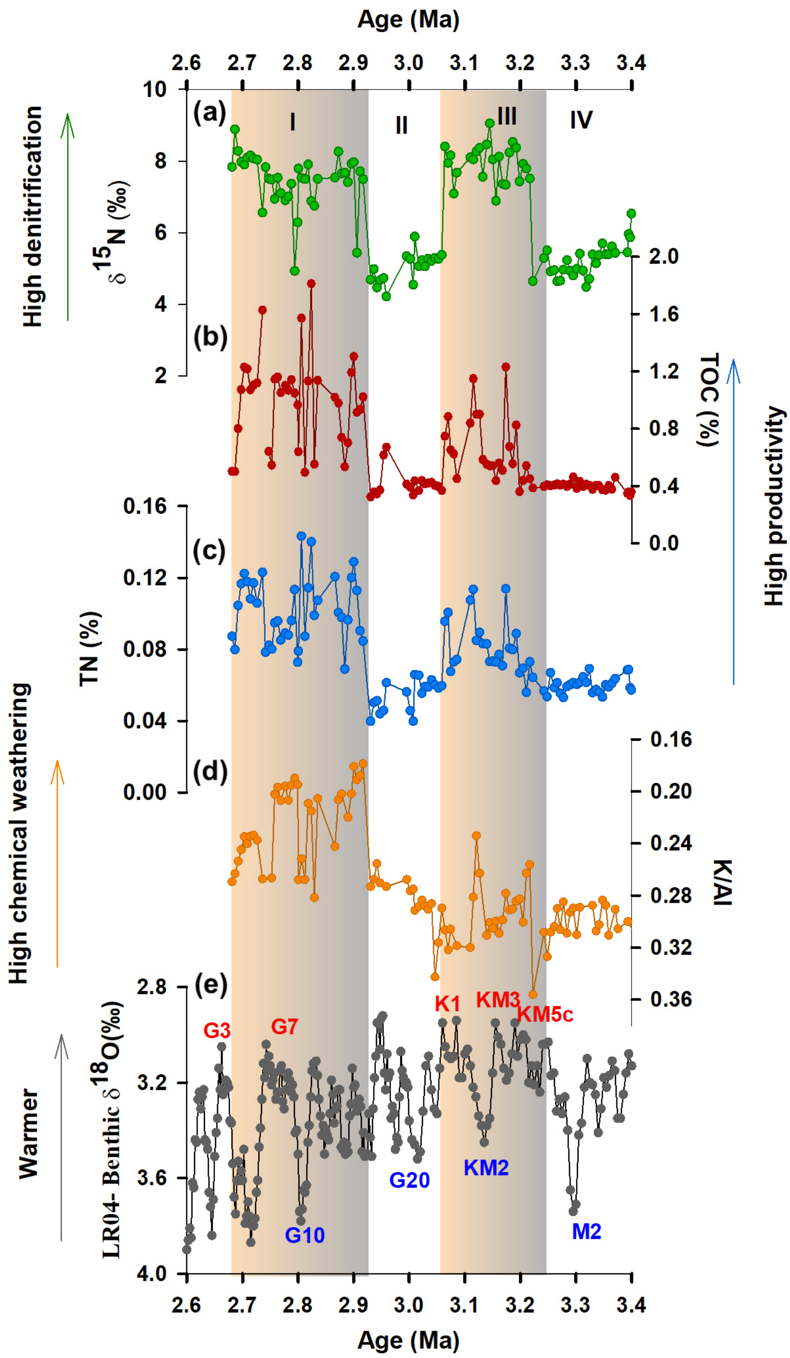

Figure 4.4: South Asian monsoon variability during late Pliocene. (a) $\delta^{15}N$ (‰) values of the SOM (present study) represent water column denitrification at the eastern Arabian Sea; (b, c) TOC % and TN % of the SOM (present study) indicate the surface productivity at the study site; (d) K/Al ratio (Sarathchandraprasad et al., 2021) represents chemical weathering related to SoAM variability; (e) LR04 stack of $\delta^{18}O$ (‰) of benthic foraminifera (Lisiecki and Raymo, 2005).

Interval IV (3.4 - 3.2 Ma)

We find weakened monsoon from 3.4 Ma to the beginning of MPWP (interval IV) that corresponds to reduced insolation at 15 °N summer solstice (Fig. 4.5a). The insolation received at the northern tropics, governed by orbital cycles (eccentricity, precession, and obliquity), is the primary factor controlling the cross-equatorial pressure gradient and hence the SoAM strength. The pCO_2 also declines from more than 400 ppm to around ~350 ppm during this period (Fig. 4.5c) causing global cooling including M2 glaciation (Fig. 4.5d). This global cooling would have caused the weakening of SoAM through the thermodynamic effect. The spring Arctic SIE for the late Pliocene is reconstructed recently using both the sea ice biomarker IP25 and a related open-water highly branched isoprenoid (HBI) lipid (HBI III) from ODP site 910C, Yermak Plateau (Rahaman et al., 2020). The spring sea ice extent is estimated in semi-quantitative form (SpSIC %) based on a regional calibration in the Arctic (Smik et al., 2016). The Arctic SIE was quite high during interval IV (Fig. 4.5b) that would cause an adverse dynamical effect. Enhanced Arctic SIE causes a northward transport of energy from the northern tropic's boundary leading to a hemispherically asymmetric energy export, which would result in a northward cross-equatorial energy flux and therefore a southward shift of the ITCZ (Schneider et al., 2014). Thus both the thermodynamical as well as the dynamical effect led to reduced SoAM strength during interval IV.

Interval III (3.2 – 3.05 Ma, MPWP)

During the early part of MPWP including MIS KM5c (~3.205 Ma) and KM3 (3.167 - 3.150 Ma), we find that enhanced monsoon coincides with higher insolation and pCO_2 along with high Arctic SIE (interval III; Fig. 4.5). It indicates that the orbital forcing and the associated solar insolation along with greenhouse gas forcing overcame the adverse effect of high Arctic SIE leading to strengthened monsoon during the MPWP. It is also supported by findings from a model study (HadCM3) that shows that the enhanced monsoon, particularly during MIS KM5c, was due to the increase in CO_2 concentration (Presscott et al., 2019).

During the later part of MPWP (3.16 Ma - 3.05 Ma), the CO_2 concentration had declined considerably and the solar insolation was also relatively weak. Despite the weak insolation and thermodynamic effect, the SoAM was quite strong during that time as evident from the proxy data. This strong monsoon can be explained by the dynamical effect due to the considerably lower Arctic SIE found during that time. Another dynamical effect, apart from the one due to the asymmetric interhemispheric energy export, is recently proposed by Chatterjee et al., 2021 wherein reduced sea ice in the Kara Sea region is associated with the increased SoAM precipitation events. The reduction of Arctic SIE decreases the pole to the mid-latitude temperature gradient that affects the jet stream (Cohen et al., 2014; Serreze and Barry, 2011) leading to a positive pressure anomaly over northwest Europe (Zhang et al., 2020). Thereafter, the Rossby wave train from northwest Europe propagates in two different pathways - one propagates zonally eastward and locks at 60° N while the other moves southward from Europe before diverting towards the east and reaching the east Asian region (Chatterjee et al., 2021). It strengthens the subtropical high, which favors increased monsoonal precipitation. Thus, the dynamical effect of lower Arctic SIE can cause higher SoAM precipitation despite unfavorable thermodynamical effects.

Interval II (3.05 - 2.9 Ma)

The reduced SoAM during interval II (3.02 to 2.9 Ma) is well explained by the low CO_2 concentration, which declines below 350 ppm (Fig. 4.5c). The insolation is also lower during the early part of interval II that contributes to lower SoAM strength. The Arctic SIE is low but the strong thermodynamic effect due to CO_2 lowering and the insolation forcing compensates for it resulting in weaker SoAM. During the latter part of interval II, the insolation increases that should have strengthened the SoAM. But the concurrent increase in Arctic SIE appears to keep the SoAM weak providing positive feedback to the CO_2 lowering effect.

Interval I (2.9 - 2.7 Ma)

The weakened SoAM is followed by an enhanced SoAM during the interval I (from 2.9 to 2.7 Ma), which corresponds to the weak orbital forcing and the decreasing trend of CO_2 concentration (Fig. 4.5). The SoAM-strengthening at 2.9 Ma coincides with the INHG when the earth's temperature started to decline slowly. The Arctic SIE is also on the higher side that should have weakened the SoAM. But the SoAM strengthened significantly despite the adverse thermodynamical as well as the dynamical effects. This intensification of SoAM is attributed to the tectonically induced reorganization of ITF (Sarathchandraprasad et al., 2021).

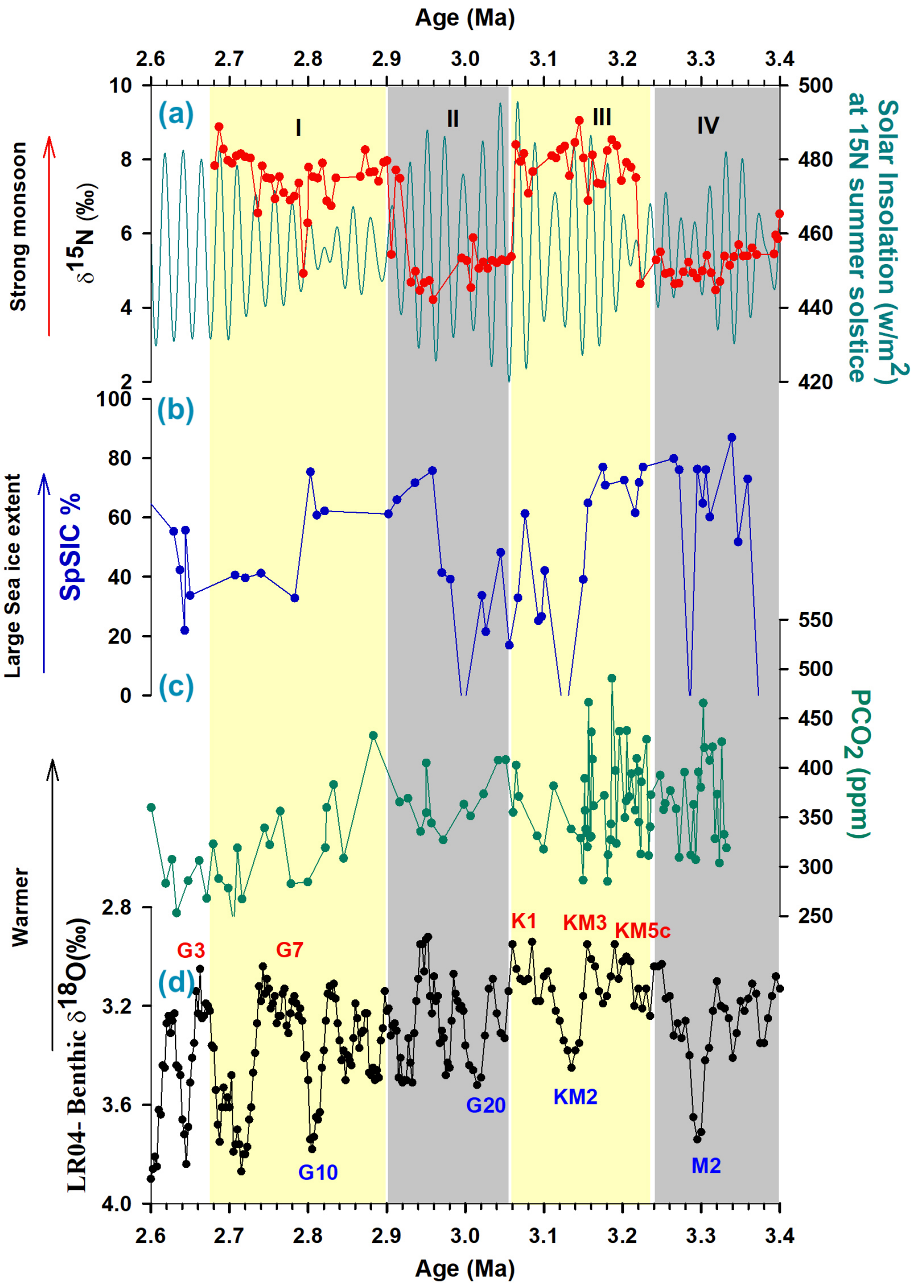

Figure 4.5: Forcing factors of SoAM variability during late Pliocene. (a) The solar insolation at 15°N summer solstice (Berger and Loutre, 1991) plotted with monsoon record ($\delta^{15}N$) from the eastern Arabian Sea; (b) Spring sea ice cover

(SpSIC%) constructed using sea ice proxy (IP25) and open water biomarker HB III from the Yermak Plateau (ODP 151, Site 910C) indicates Arctic sea ice extent during late Pliocene (Rahaman et al., 2020); (c) The atmospheric CO_2 concentration derived from boron isotope ($\delta^{11}B_{borate}$) of *G. ruber* from the ODP site 999, Caribbean Sea (de la Vega et al., 2020); (d) LR04 stack of $\delta^{18}O$ (‰) of benthic foraminifera shows glacial-interglacial cycles (Lisiecki & Raymo, 2005). The yellow bands show periods of enhanced monsoon, while the gray bands show periods of weakened monsoon.

The northward shift of tectonic plates below New Guinea during mid-Piacenzian changed the source water of ITF from warmer south pacific water to colder north pacific water (Cane and Molnar, 2001). This caused the cooling of southern tropical Indian Ocean subsurface water by 4 ◦C at 2.95 Ma, which eventually gets transferred to surface water (Karas et al., 2009; Karas et al., 2011). The colder southern Indian Ocean tropical water increases cross-equatorial pressure gradient leading to enhanced inter-hemispherical heat and moisture transport (Roxy et al., 2015; Vidya et al., 2020), which ultimately resulted in SoAM intensification during the interval I.

4.4 Conclusions

The SoAM variability during the late Pliocene - a modern-like warm period - can help to understand monsoon response to a global warming scenario. We find high surface productivity and strong denitrification supported by high chemical weathering during MPWP and from 2.9 to 2.7 Ma indicating intensified SoAM, while, during 3.4 to 3.2 Ma and 3.05 to 2.9 Ma, the weak denitrification, low surface productivity, and low chemical weathering suggests weakened SoAM. The SoAM variability is the result of an interplay between dynamic effects (orbitally controlled insolation at 15 °N summer solstice, Arctic SIE variability, southern tropical Indian Ocean surface temperature variability due to tectonically induced ITF changes) and the thermodynamic effects (global temperature change due to pCO2 variability). Higher insolation and global temperature resulted in stronger SoAM. We further find that lower (higher) Arctic SIE leads to stronger (weaker) SoAM during the late Pliocene. The Arctic SIE influences SoAM by causing asymmetric hemispheric energy export and through upper tropospheric changes via changing the jet stream flow and meridional circulation. During MPWP, a strengthened SoAM was observed following high global temperature implies that more intense precipitation is expected in near future over South Asia.

Chapter 5

Quantification of surface temperature and salinity at Lofoten Basin during Last Interglacial and Holocene period

5.1 Introduction

The Atlantic Meridional Overturning Circulation (AMOC) is a crucial factor for the sustainability of the northern high latitude climate as it transfers an enormous amount of heat. However, due to the ongoing global warming, the high latitude warming and freshening disrupt the AMOC by reducing the North Atlantic Deep Water (NADW) formation (Rennermalm et al., 2007), which adversely affects the global thermohaline circulation. The model projections predict the temperature to rise on a global scale due to anthropogenic warming with even more warming in the Arctic due to Arctic Amplification (e.g., Wang and Overland, 2009; IPCC AR6). Thus, studying oceanographic conditions in the Arctic and subarctic during past warm periods can provide a necessary test of these climate predictions and help to better understand the underlying mechanisms. The last interglacial i.e., Marine Isotope Stage 5e (MIS 5e; ~125 kyr BP) and the present interglacial i.e., Holocene (MIS 1) are suitable for such a study. Previous studies have shown that the last interglacial was interrupted by several rapid changes to a colder climate, as opposed to the Holocene, which shows a very uniform warmth as reflected from stable isotope studies of the ice cores (Kaspar et al., 2005; Otto-Bliesner et al., 2006). Thus, the last interglacial was less stable in comparison to the present one i.e., Holocene.

The present study quantifies the climate (oceanic surface temperature and salinity) during MIS 1 (Holocene) and the warmest interval of MIS 5 i.e., the last interglacial (MIS 5c to 5e), respectively at the Lofoten Basin. The surface hydrography is reconstructed through the $\delta^{18}O$ and Mg/Ca of planktic foraminifera *Neogloboquadrina pachyderma* (sinistral) and the bottom water ventilation is based on the $\delta^{13}C$ of the benthic foraminifera *Cibicidoides wuellerstrofi.*

5.2 Study Site

The sediment samples are retrieved from the Lofoten basin situated in the Nordic Sea. Two major surface current enters the Nordic Seas. The main North Atlantic Current (NAC) enters from the Faroe-Shetland Channel and propagates northward along the Norwegian and Barents Seas continental margin (Fig. 5.1). Then it enters the Arctic Ocean through the eastern Farm Strait as intermediate water. The Atlantic water transports warm and saline water to the Nordic Sea and the Arctic Ocean. Another major surface current flows from western Farm Strait to the Nordic Sea as East Greenland Current (EGC) (Fig. 5.1). It transports cold and low saline polar water to the Nordic Seas. Thus, there is an east-west gradient across the Nordic Seas. The two oceanic fronts run parallel to the main surface currents. The polar front is the boundary between low salinity polar water and relatively higher salinity Arctic water (Fronval et al., 1998), while the Arctic front is the boundary between cold Arctic water and the warm Atlantic water (Swift, 1986). The North Atlantic Deep Water (NADW) formation takes place in the Arctic water domain, where the warm saline NAC branch and cold less saline EGC branch creates a cyclonic gyre. In the early winter, the formation of sea ice leads to brine rejection, increases the surface layer density, and that induces the strong deep-water formation in the Nordic Seas. The present core site AMK-5188 is located under the direct influence of the NAC westerly branches (Fig. 5.1). The warm Atlantic water occupies the upper 600-700 m with a salinity 35 and the associated temperature between 4-6°C (Blindheim and Østerhus, 2005) (Fig. 5.2a, 5.2b). The low salinity (below 34.9) water from Greenland Basin intrudes under the Atlantic water and spread across the whole Lofoten Basin as an intermediate layer. The potential temperature in this layer varies from +0.5°C to -0.5°C and it extends from 800 to 1000 m in depth. The deeper water in Lofoten Basin originates from the Arctic Ocean, which is identified by salinity maximum (up to 34.91) from 1500 to 2500 m depth.

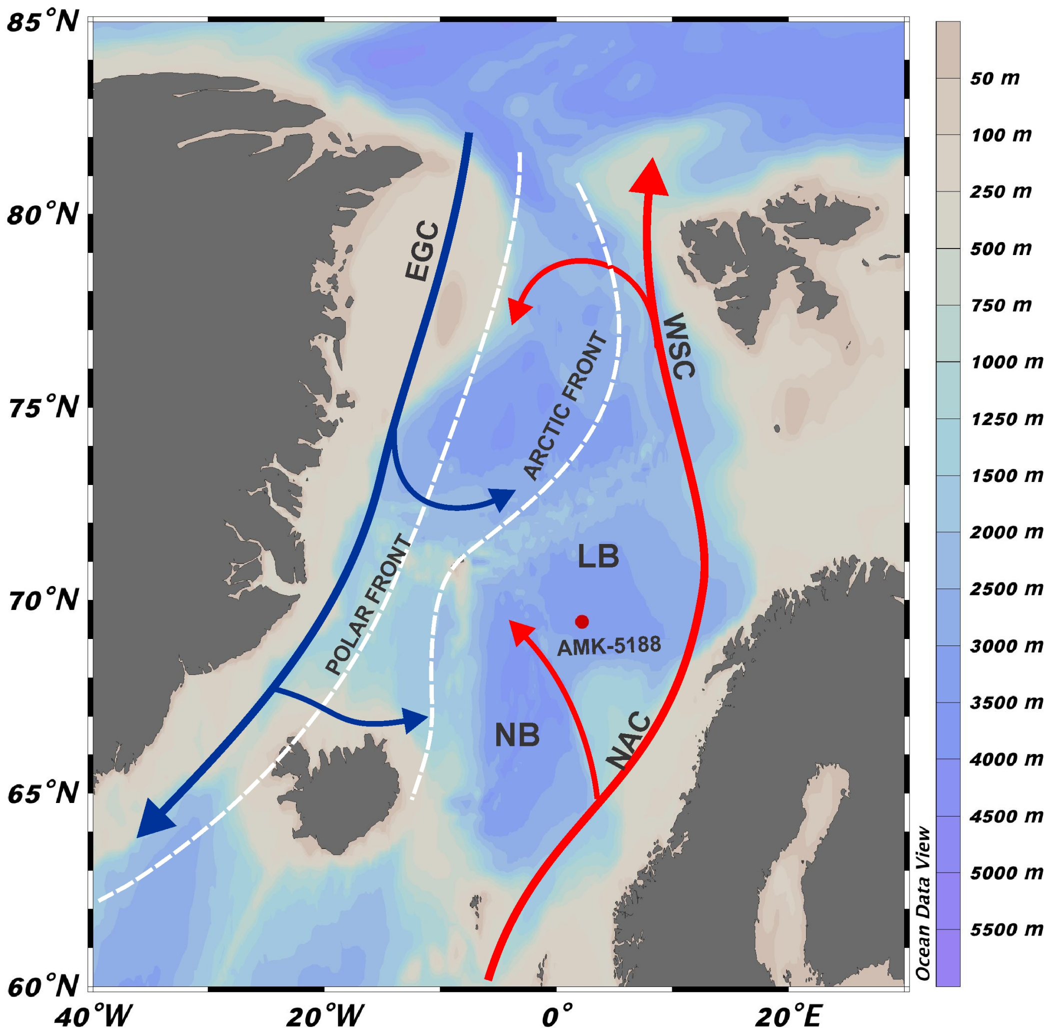

Figure 5.1: Sample location; the core site AMK-5188 (69°02.667´N, 02°06.595´E) is shown by the closed red circle. LB: Lofoten Basin, NB: Norwegian Basin, NAC: North Atlantic Current, WSC: West Spitsbergen Current, EGC: East Greenland Current. Warm surface current is shown by red arrow while the blue arrow represents cold surface current. The Polar front and the Arctic front are shown by white dotted lines.

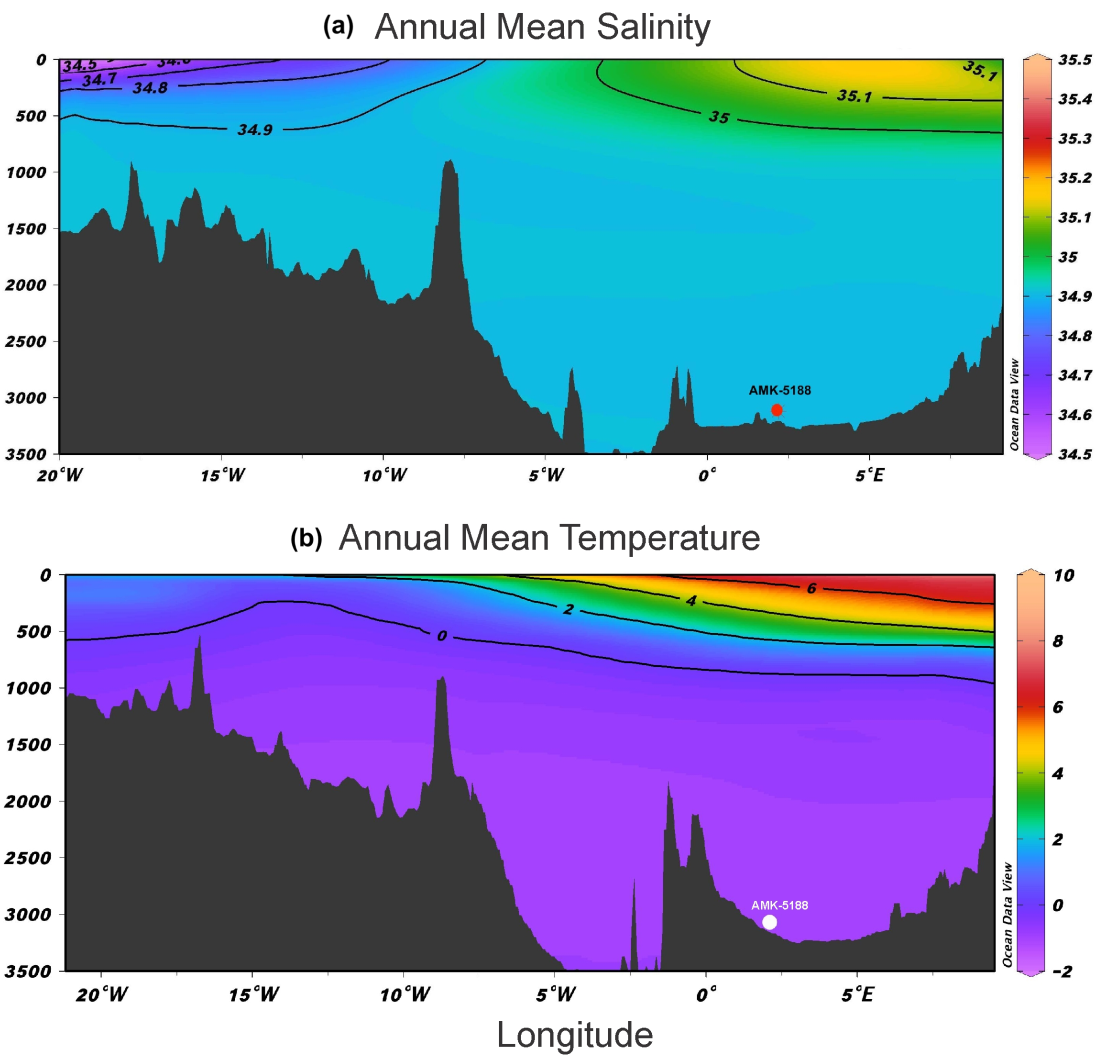

Figure 5.2: Profile of modern oceanography at the Lofoten Basin; (a) and (b) The annual mean salinity and temperature profile, respectively, plotted in the transect from the Greenland Sea to the eastern Norwegian Sea. The sample location is shown in the red and white circles.

5.3 Materials and Methodology

5.3.1 Core details and Chronology

Core AMK-5188 is retrieved from the southern Lofoten Basin in the Norwegian Sea (69°02.667′N, 02°06.595′E) at a water depth of 3206 m (Fig. 5.1). The core is 417 cm in length, with the Holocene occurring from 0 to 80 cm and the MIS 5 occurring between 180 to 270 cm. The core is subsampled at 1 cm during both intervals. The chronology of the core from 0.5 to 110.5 cm depth is based on 10 Accelerator Mass Spectrometry (AMS) ^{14}C dates (Fig. 5.3a).

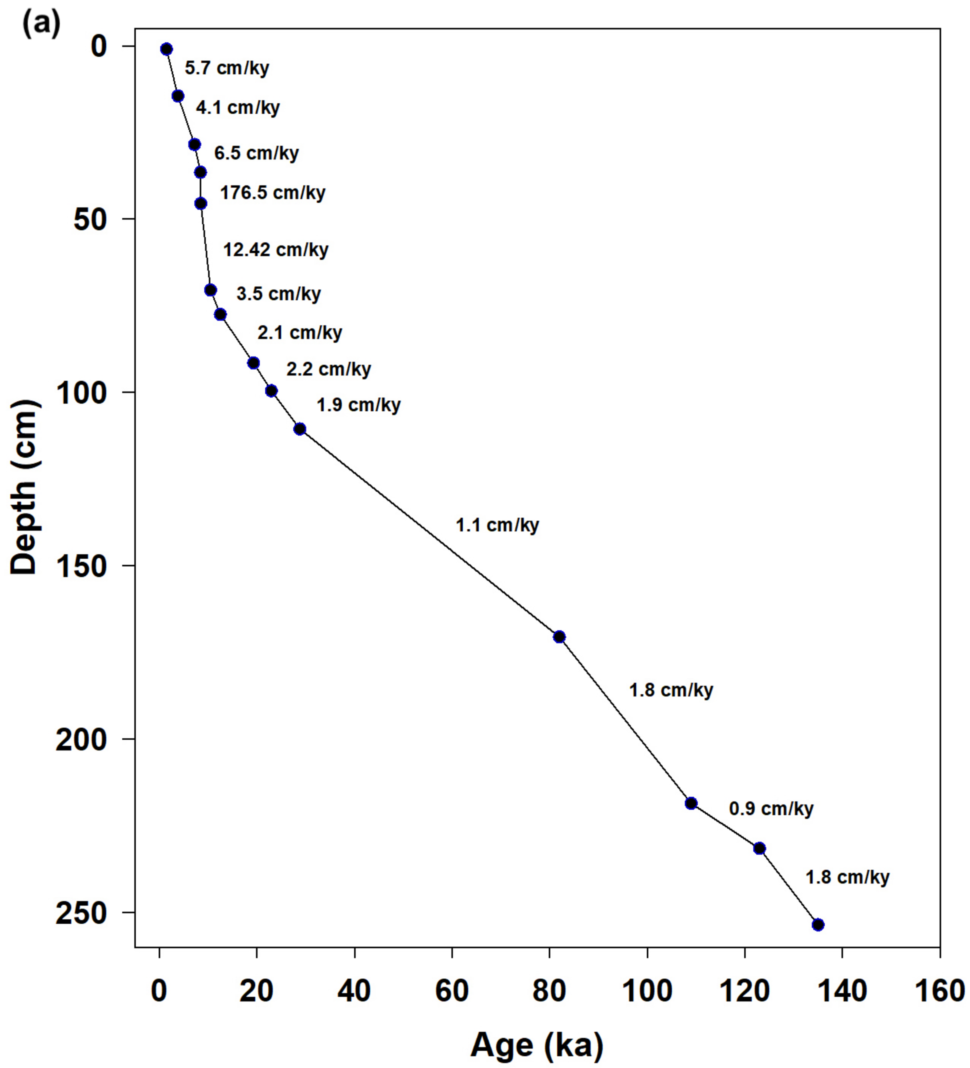

Figure 5.3: Chronology of core AMK-5188; (a) The tie points used to develop the Age-Depth model for core AMK-5188; (b) From depth 0 to 110 cm, tie points for age is given by ^{14}C dates. From depth 175 to 250 cm, tie points for age are generated using the low and high resolutions record of $\delta^{18}O$ of planktic foraminifera *N. pachyderma* (sin.) (black and blue curve respectively) compared with Marine Isotope stage ($\delta^{18}O$ of benthic foraminifera) LR04 $\delta^{18}O$ stack (Lisiecki and Raymo, 2005).

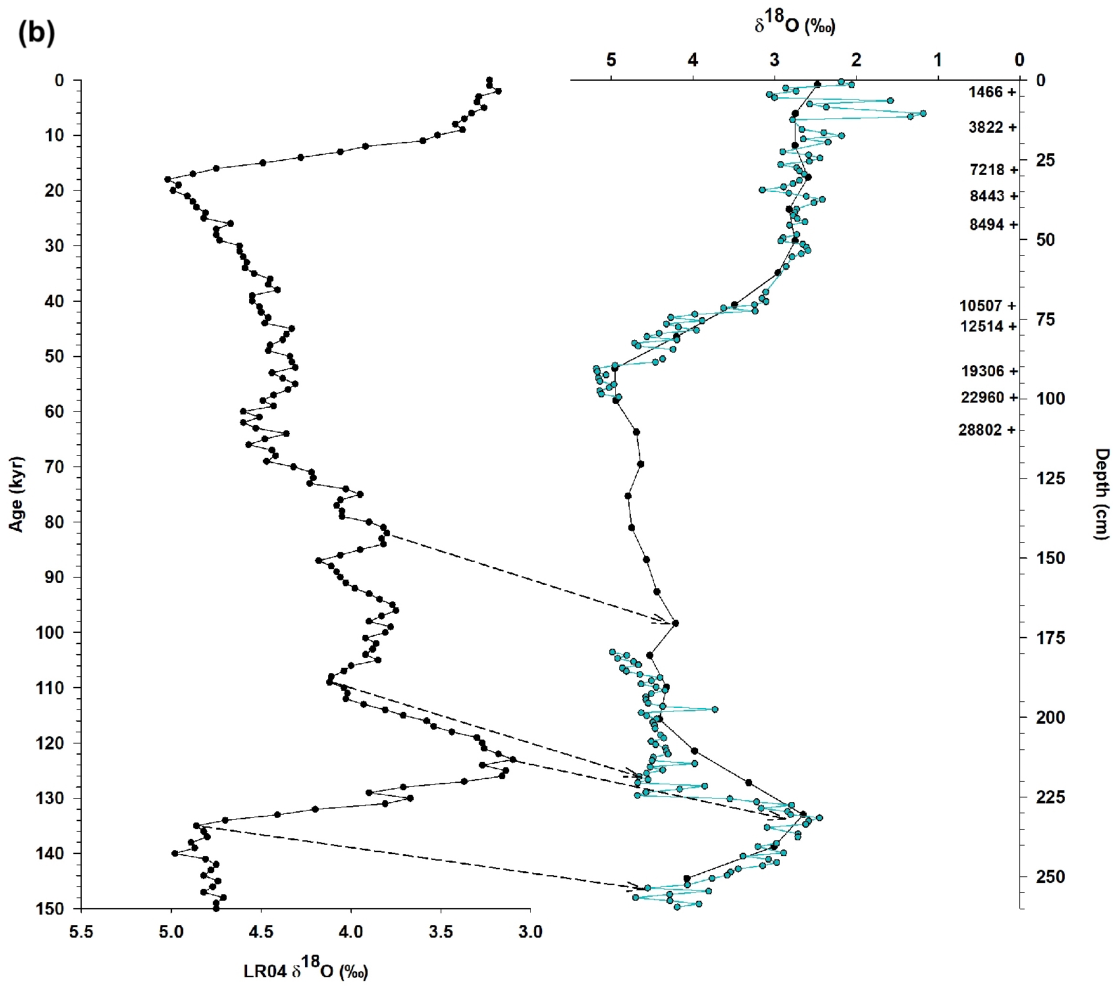

From 170.5 to 270.5, the age is calculated based on oxygen isotope stratigraphy by comparing the $\delta^{18}O$ of *N. pachyderma* (sin.) with the LR04 stack (Lisiecki and Raymo, 2005) (Table - 5.1; Fig. 5.3b). For AMS ^{14}C dating, the planktic foraminifera, *N. pachyderma* (sin.), in the size range of 150 to 250 μm from different depths were sent to Beta Analytic Testing Laboratory, USA, and Poznan Radiocarbon Laboratory, Poland. The ^{14}C dates are calibrated using the calibration program CALIB 8.2 with Marine20 (Stuiver and Reimer, 1993) and with a reservoir age correction of 400 years.

Table 5.1: Tie points for chronology of core AMK-5188

Depth in core (cm)	^{14}C age (yr BP)	Calibrated age (yr BP)	Depth in core (cm)	Age (yr BP) (oxygen isotope stratigraphy)
0-2	1920±30	1466	170-180	82000
14-15	3845±35	3822	218- 219	109000
28-29	6750±40	7218	231-232	123000
36-37	7990±50	8443	253-254	135000
45-46	8040±50	8494		
70-71	9600±50	10507		
77-78	10980±30	12514		
91-92	16600±40	19306		
99-100	19700±60	22960		
110-111	25280±100	28802		

5.3.2 Sample preparation and analysis

***Stable Isotope analysis*:**

The planktic foraminifera, *N. pachyderma* (sin.), were used to analyze the oxygen ($\delta^{18}O$) and carbon ($\delta^{13}C$) isotopes in order to reconstruct the surface water's physical properties. To reconstruct the bottom water condition, the benthic foraminifera, *C. wuellerstrofi*, is used to analyze the $\delta^{18}O$ and $\delta^{13}C$. The foraminifera size chosen for isotopic analysis is >250 μm. At a few depths, where sufficient foraminifera tests were not found, >125 μm size is used. The stable isotopes are measured on an Isoprime Dual Inlet Isotope Ratio Mass Spectrometer (IRMS) at the Marine Stable Isotope Lab (MASTIL) of National Centre for Polar and Ocean Research, Goa, India. The precision (1σ standard deviation) for $\delta^{18}O$ and $\delta^{13}C$ analysis are ± 0.08 and ± 0.06, respectively, based on repeated measurements of the reference material IAEA-603 (n = 185). The results are reported relative to the Vienna Pee Dee Belemnite (VPDB).

***Trace element analysis*:**

The past sea surface temperature (SST) is determined using the Mg/Ca content in planktic foraminifera *N. pachyderma* (sin.) shells, picked from the same sample set used for the stable isotope analysis. *N. pachyderma* (sin.) is a polar species, found throughout the upper water column abundantly from 50- 100 m depth. *N. pachyderma* (sin.) blooms during the spring and late summer, therefore the Mg/Ca analyses would reflect the spring or late summer temperature. The cleaning was carried out following Barker et al., 2003, which includes different phases of removing contamination. Around 50 tests of foraminifera were selected from a size range >250 μm and some samples of >125 μm. Then, the tests were gently crushed between two clean glass slides under the microscope to open the individual chambers and, transferred to the cleaned vials. The crushed foraminifera tests were cleaned to remove the alumino-silicates, followed by the removal of organic matter using an oxidizing agent (alkali buffered solution of H_2O_2). Further, the weak acid leach was performed to remove any adsorbed contaminant from the test fragment, and finally dissolution in dilute HNO_3 was done. Measurements were made using an iCAP 700 Inductively Coupled Plasma - Optical Emission Spectrometry (ICP-OES) at the Paleothermometry Lab of National Centre for Polar and Ocean Research, Goa, India. The residual contamination was monitored using Fe/Mg ratio and the sample was rejected with Fe/Mg exceeding 1 mol/mol (Barker et al., 2003). The precision obtained for Mg/Ca values through repeated measurement of carbonate reference material EURONORM-CRM 752-1 over the period of analysis is 0.02 mmol/mol.

The Mg/Ca and $\delta^{18}O$ of *N. pachyderma* (sin.) are used to reconstruct the past SST and sea surface salinity (SSS) using Paleo-Seawater Uncertainty Solver (PSUSolver) software in Matlab (Thirumalai et al., 2016). This software accepts foraminiferal Mg/Ca and $\delta^{18}O$ as input and uses the bootstrap Monte Carlo procedure to solve for seawater $\delta^{18}O$ and temperature. It also provides the propagated uncertainty. The calibration equation used to convert Mg/Ca ratio to SST is as follows: $SST = (1/0.099)* \ln((Mg/Ca)/0.549)$ (Kozdon et al., 2009). The $\delta^{18}O$ of seawater ($\delta^{18}O_{sw}$) is constructed based on the SST record and $\delta^{18}O$ of *N. pachyderma* (sin.) ($\delta^{18}O_c$) using the following equation: T = 12.69 - 3.55

($\delta^{18}O_c$ - $\delta^{18}O_{sw}$) (Multiza et al., 2003). $\delta^{18}O_{sw\ (local)}$ is corrected for sea level using equation: $\delta^{18}O_{sw}$ = $\delta^{18}O_{sw\ (local)}$ - 0.008*sea level. The $\delta^{18}O_{sw}$ is corrected for sea level variation using the sea-level curve record from Spratt and Lisiecki et al., 2016. Then, the $\delta^{18}O_{sw}$ is converted into salinity using the equation from Kozdon et al., 2009, i.e., $\delta^{18}O_{sw\ (local)}$ = 0.36* (Salinity - 12.17).

5.4 Results

5.4.1 Stable isotopes

The $\delta^{18}O$ values of the *N. pachyderma* (sin.) vary between 5.5 to 2.5 ‰ during MIS 5 and from 4.5 to 1 ‰ during Holocene. The $\delta^{18}O$ values are high and vary between 4.5 to 4 ‰ towards the end of penultimate glacial maxima (MIS 6; 145 to 138 kyr) (Fig. 5.4b). After this glacial period, the $\delta^{18}O$ values start to decrease from ~5.5 to 3.5 ‰ during the penultimate deglaciation. The $\delta^{18}O$ values are very low and vary in a small range between 3.5 to 3 ‰ during the last interglacial period (MIS 5e; Fig. 5.4b). Further, it starts to increase (~5 ‰) after the last interglacial period showing the transition from the last interglacial to the beginning of the last glacial period. The $\delta^{18}O$ values of the *N. pachyderma* (sin.) show a continuous decreasing trend from 14 to 2 kyr BP (Fig. 5.5a).

The $\delta^{18}O$ values of the *C. wuellerstrofi* vary from 5 to 3‰ during the last interglacial period and between 4.6 to 3.8 ‰ during Holocene. The low $\delta^{18}O$ values (~3.2 ‰) of benthic foraminifera during the last interglacial period increase afterward from 118 to 89 kyr BP indicating glacial condition (Fig. 5.4c). During the Holocene, the $\delta^{18}O$ values are low in the early phase and increase for ~2 kyr BP from 9.8 to 8.2 kyr BP (Fig. 5.5b). Afterward, it starts to decrease from 4.4 to 3.9 ‰ during 8 to 4 kyr BP. There is a sudden increase in $\delta^{18}O$ values from 3 to 2 kyr BP.

The $\delta^{13}C$ values of *C. wuellerstrofi* vary from 2 to 0.8 ‰ during the last interglacial, while it varies between 1.5 to 1 ‰ during the Holocene. The $\delta^{13}C$ values are high during the early phase of the last interglacial period and range between 1.8 to 1.4 ‰, which decreases to ~1 ‰ during the peak of the last interglacial period (Fig. 5.4f). Further, they increase to higher values (1 to ~2 ‰) from 110 to 87 kyr BP. The $\delta^{13}C$ values show an increasing trend in the early phase from 1.1 to 1.3 ‰ and then decreased to 1.1 ‰ from 9.8 to 8.6 kyr BP interval (Fig. 5.5c). It increases afterward from 1.2 to 1.5 ‰ during 8 to 4 kyr BP interval. There is a sudden drop in $\delta^{13}C$ value during the late Holocene (3 to 2 kyr BP).

5.4.2 Sea surface temperature and salinity

The sea surface temperature is reconstructed using *N. pachyderma* (sin.), which predominantly dwells at the mixed layer depth (50-100 m depth). It represents the annual average temperature at the high northern latitude. The SST at the study site varies between 2 to 8°C during the MIS 5 and 0 to 10°C during the Holocene. The SST is high at the onset of the last interglacial period (MIS 5e) at around 6°C, however, it reduces to 3°C in the middle of the interglacial period (Fig. 5.4d). Further, it increases to ~7°C towards the end of the last interglacial. After MIS 5e, the average SST declines from 118 to 87 kyr BP with two peaks of high SST indicating the MIS 5c interstadial (Fig. 5.4d). In the early Holocene, the SST starts to decline from ~8 °C to 2 °C from 11.9 to 8.6 kyr BP (Fig. 5.5d). Subsequently, it increases to the observed maximum temperature (8 °C) at around 8 kyr BP and stays at the same level with a slight decline till 4 kyr BP (Fig. 5.5d). Further, the SST decreases to ~ 3 °C from 4 to 2 kyr BP and then it increases to the modern value.

The SSS anomaly from the modern value (35.3 PSU) follows the temperature trend during Holocene and an opposite trend during MIS 5 (Fig. 5.4e; Fig. 5.5e). The SSS anomaly increases to the modern value in the early stage of the last interglacial period. Then it decreases in the middle of the last interglacial period and attains the modern value towards the end of the last interglacial (Fig. 5.4e). The salinity rises to a high value after the end of the last interglacial from 118 to 87 kyr BP indicating a colder climate. During the Holocene, the salinity fluctuates abruptly from the modern value. In the early stage of the Holocene, the salinity decreases and reaches near the modern value at ~10 kyr BP (Fig. 5.5e). It further decreases from the modern referred value from 10 to 8.6 kyr BP and subsequently increases to higher values till 8 kyr BP. During 8 to 4 kyr BP, it becomes stable and slowly decreases to the modern value. Further, it suddenly decreases to a minimum value from 3 to 2 kyr BP and rises again to the modern value.

5.5 Discussion

5.5.1 Last Interglacial to last glacial transition

The $\delta^{18}O$ of planktic *N. pachyderma* (sin.), SST, and SSS shows the surface hydrography, while the $\delta^{18}O$ and $\delta^{13}C$ of *C. wuellerstrofi* indicate the bottom water condition from peak warm period (MIS 5e) to the beginning of last glacial period. During early MIS 5e, the $\delta^{18}O$ values of *N. pachyderma* (sin.) decreases and the SST increases to ~6 °C (Fig. 5.4b and 5.4d) indicating the warmer surface water at the Lofoten Basin. The surface salinity also increases during this phase (Fig. 5.4e). It suggests the influence of the warm and saline Atlantic Water (AW) at the Lofoten Basin during the early MIS 5e. However, this warm and higher salinity surface water is interrupted by a colder and lesser salinity water influx at around 124 kyr BP as evident from the decrease in SST (~3°C) and SSS (Fig. 5.4d and 5.4e). This cold event exists for a short time interval. After this cold event, the surface temperature again increased to around 7°C and the surface salinity reached the modern value towards the end of the last interglacial period. It suggests that the last interglacial attained its peak warmth relatively late after the deglaciation. Similar results are reported from the Nordic Seas where it shows that the last interglacial period had two distinct phases (Bauch and Erlenkeuser, 2008). The early warm phase was interrupted by the subsequent cooling phase, which lasted until 118.5 kyr BP. The primary reason behind this cooling event during this interglacial period may be related to the breakdown or reduction of thermohaline circulation within the Nordic Seas (Galaasen et al., 2014). The fresh water influx after the deglaciation could have possibly decreased the water column density and declined the NADW formation that led to lower heat transport to the northern high latitude and reduced the temperature. In the present study, the low $\delta^{13}C$ value of *C. wuellerstrofi* during the colder event also indicates the reduction of bottom water ventilation by the NADW (Fig. 5.2f). It is also seen that the NADW influence was strong at the onset of the last interglacial period and then was interrupted by several prominent, centennial-scale reductions (Cortijo et al., 1994; Govin et al., 2012; Galaasen et al., 2014). The reduction of temperature during the middle of interglacial period is also supported by Bauch et al., 2012, where they suggest that the temperature for Nordic Seas were generally colder during the last interglacial than in the Holocene. The surface water temperature demonstrates the significant movement of oceanographic fronts. During the warmer conditions, the Arctic front is located far west of the present day location at least within the Iceland region (Fronval et al., 1998). From 126 to 125 kyr BP, the Norwegian Current was more strong and westerly located. During the later warm intervals, after the major cold event at ~ 124 kyr, the higher heat flux to the western part of the basin reflects in a combination of a strong Irminger Current and/or a weaker East Greenland Current (Fronval et al., 1998). During the colder event at ~ 124 kyr, the Arctic front was located more southeasterly than today, and intrusion of North Atlantic current was probably limited to a narrow corridor in the eastern Norwegian Sea (Fronval et al., 1998). After this cooling event, the climatic optimum was reached, which suggests the most intense advection of the Atlantic surface water mass until 118 kyr BP. The last interglacial period is marked by the absence of the ice-rafted debris in the Nordic Seas (MD 99-2304; Risebrobakken et al., 2005) indicating the warmer condition during MIS 5e (Fig. 5.4g).

After the last interglacial period (MIS 5e), the increase in $\delta^{18}O$ values of both planktic and benthic species from 118 to ~89 kyr BP indicates the beginning of the last glacial period (Fig. 5.4b and 5.4c). The SST shows slight declining trend in this interval with two high SST peaks at ~100 kyr BP and another at ~ 92 kyr BP (Fig. 5.4d). In this interval of an overall colder climate, the surface salinity is more than the modern value (Fig. 5.4e). The ventilation, as shown by the $\delta^{13}C$ values of *C. wuellerstrofi* (Fig. 5.4f), enhances during this cold interval. In a colder climate, the saltier Atlantic water achieves a higher density, and thus sinks to the deeper depth in the water column. The colder climate after the end of the last interglacial is also reflected in the high IRD in the Nordic Seas (Fig. 5.4g). However, the IRD signature is not continuous through out this glacial period. The high SST peaks found in the present study during this glacial period corresponds to the absence of IRD in the Nordic Seas (Fig. 5.4d and 5.4g). It indicates the two interstadial during the MIS 5 with high temperature and high salinity with less IRD.

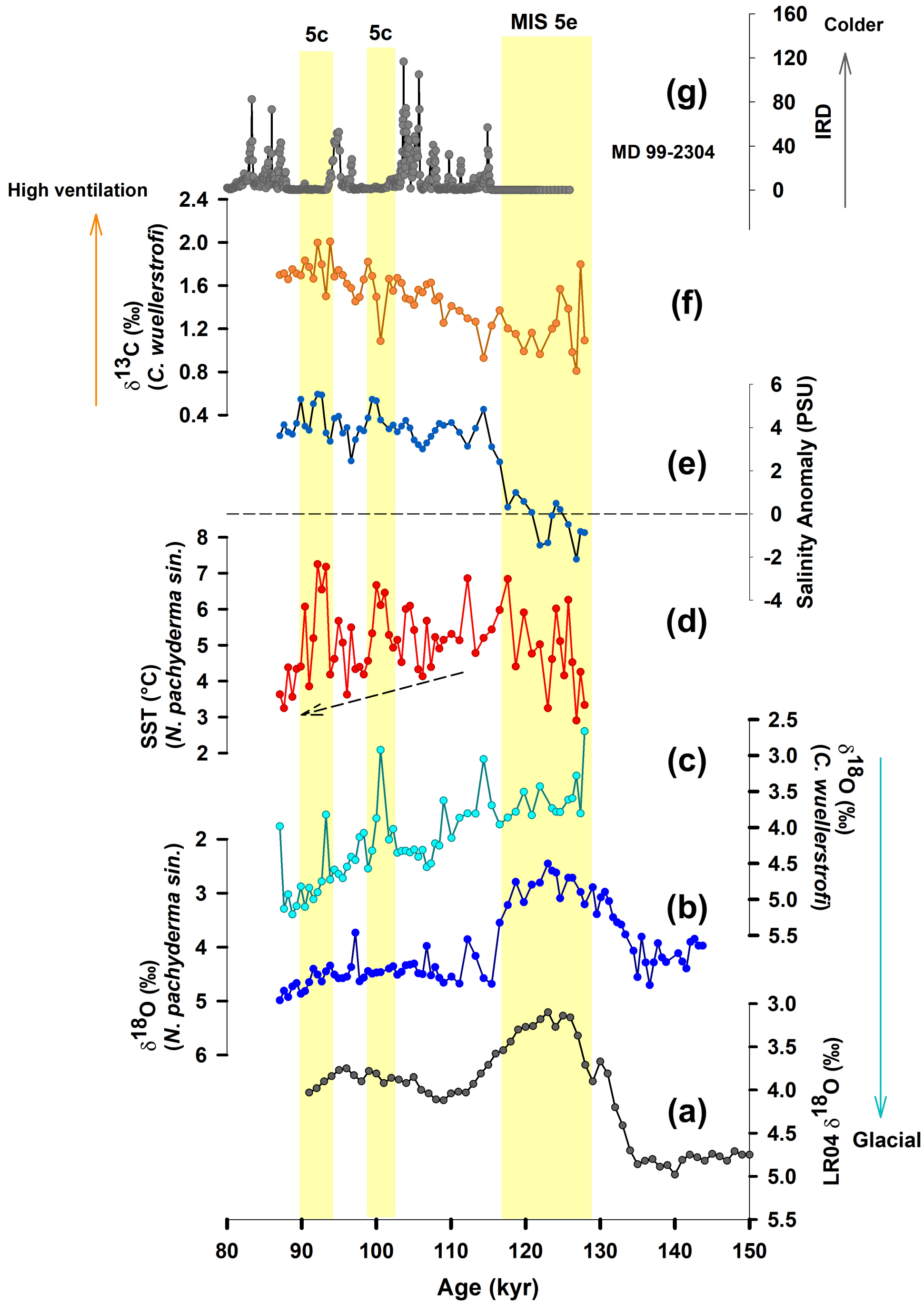

Figure 5.4: (a, b, and c) The $\delta^{18}O$ of benthic foraminifera from LR04 stack (Lisiecki and Raymo, 2005), the $\delta^{18}O$ of *N. pachyderma* (sin.), and $\delta^{18}O$ of *C. wuellerstrofi*, respectively; (d) SST at Lofoten Basin reconstructed using Mg/Ca ratio of *N. pachyderma* (sin.); (e) Sea surface salinity anomaly shows the change

in surface salinity with reference to the modern value; (f) $\delta^{13}C$ value of *C. wuellerstrofi* shows the bottom water ventilation at the study site; (g) Ice rafted debris (IRD) recorded from site MD99-2304, Nordic Seas shows the colder and warmer condition (Risebrobakken et al., 2014).

5.5.2 Holocene

During the early phase of Holocene, the warm and high salinity surface water (high SST and SSS; Fig. 5.5d and 5.5e) gradually cools and gets fresher as evident by a decrease in SST and SSS till 8.6 kyr BP. From 11.9 to 9.8 kyr BP, the declining trend of SST corresponds to the increase in $\delta^{13}C$ values indicating an increase in bottom water ventilation (Fig. 5.5d and 5.5c). The $\delta^{13}C$ of the benthic foraminifera is widely used to trace the relative influence of nutrient poor (high $\delta^{13}C$) NADW and nutrient rich (low $\delta^{13}C$) southern sourced bottom water (Curry and Oppo, 2005; Galaasen et al., 2014). At the surface, the primary productivity preferably uses lighter isotope i.e., ^{12}C for photosynthesis as lower dissociation energy is required to break the bonds containing lighter isotopes due to their higher vibrational energy. It thus enriches the water with the heavier isotope i.e., ^{13}C. Thus, the Atlantic surface water has a high $\delta^{13}C$ value. While, the aged southern sourced water mass has a low $\delta^{13}C$ value due to the respiration of the organic matter, which releases ^{12}C into the water. The declining trend of SST and SSS during this interval could be due to the enhanced deglacial fresh water influx from the Greenland ice sheet. It may also have delayed the warming in the central Nordic Seas, which thereby influenced the AMOC development (Seidenkrantz et al., 2012; Blaschek and Renssen, 2013). However, the continuous decrease in SST from 9.8 to 8.6 kyr BP strongly corresponds to a decrease in $\delta^{13}C$ and an increase in the $\delta^{18}O$ values of *C. wuellerstrofi* (blue coloured band; Fig. 5.5d, 5.5c, and 5.5b) indicating a colder climate with the reduction of bottom water ventilation. During this interval, the decrease in surface salinity indicates the influx of low salinity water at the core site (Fig. 5.5e). The fresh water influx could have weakened the thermohaline circulation and reduced the heat transport to the higher latitudes. That could have led to the cooling event during the early Holocene. This cold event from ~9.8 to 8.6 kyr BP could be related to the 8.2 kyr event, a widespread cold event related to a catastrophic freshwater release into the

Labrador Sea and disruption of NADW formation (Barber et al., 1999; Rohling and Palike, 2005). The model simulations show that the fresh water outburst during 8.2 kyr strengthened the subpolar gyre, however, it weakened the transport of AW into the Nordic Seas (Born and Levermann, 2010; Telesinski et al., 2015). This resulted in a cold and dry climate over higher latitudes. Further, the low $\delta^{13}C$ values of benthic foraminifera indicate the limited deep-water renewal associated with the AMOC collapse during this interval (Hall et al., 2004). Thus, it suggests that the sudden climate change due to fresh water outburst were probably superimposed on a longer-term climatic trend.

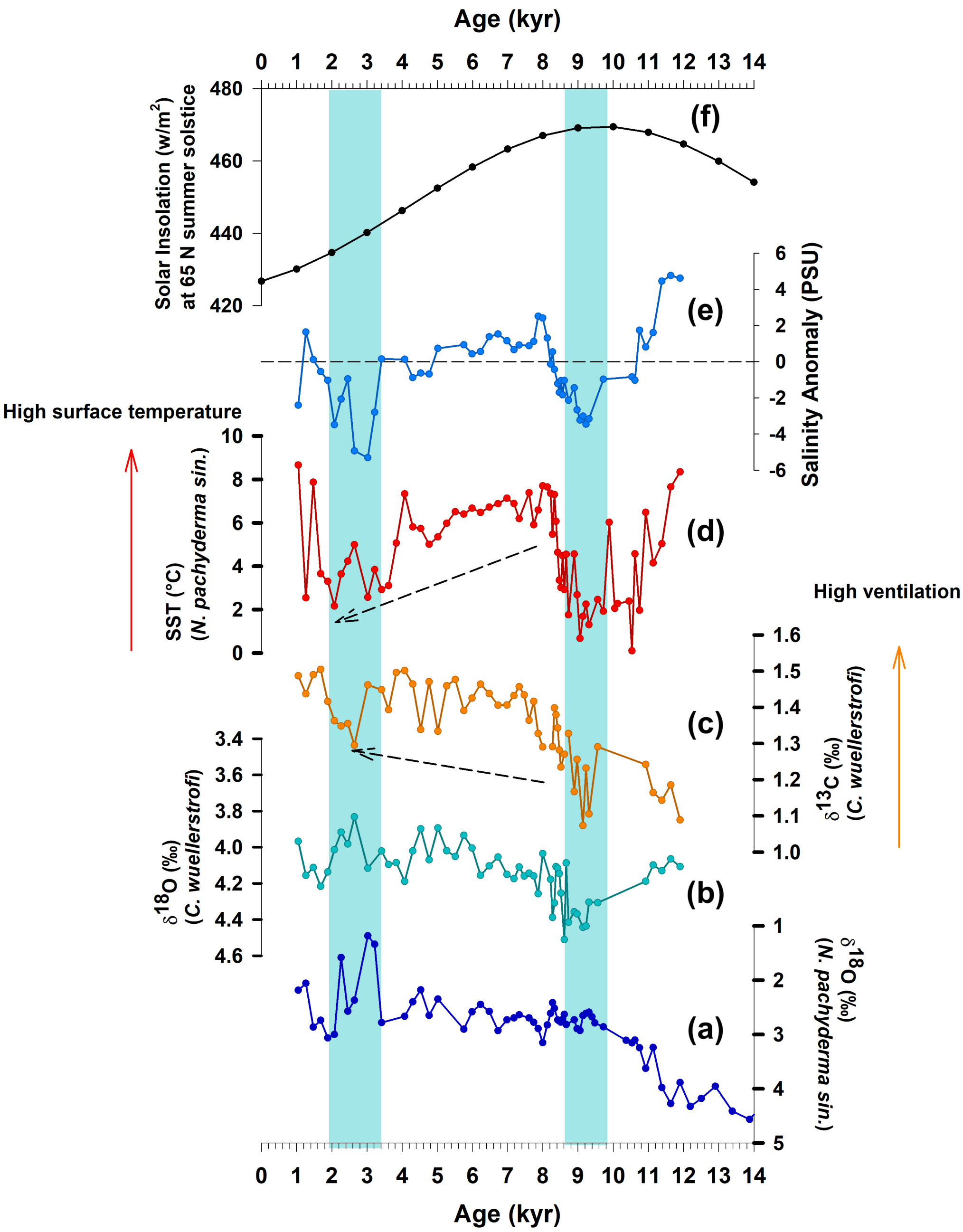

Figure 5.5: (a and b) The $\delta^{18}O$ of planktic foraminifera *N. pachyderma* (sin.) and $\delta^{18}O$ of benthic foraminifera *C. wuellerstrofi*, respectively; (c) $\delta^{13}C$ values of *C. wuellerstrofi* show the bottom water ventilation at the study site; (d) SST at Lofoten Basin generated using Mg/Ca ratio of *N. pachyderma* (sin.) (e) Sea surface salinity anomaly shows the change in surface salinity with respect to the modern value; (f) Solar insolation at 65°N summer solstice (Berger & Loutre, 1991).

The SST increased after this cold event and reached the mid Holocene thermal maxima at around 8 kyr BP. The SST, SSS, and the bottom water ventilation (Fig. 5.5d, 5.5e, and 5.5c) reached the modern conditions at 8 kyr BP and thereafter declined slightly till 4 kyr BP. It shows that, after the 8-7 kyr, when the fresh water input ceased completely, the modern surface ocean circulation pattern and the flow strength of AMOC were reached. This warmer climate was further disturbed by another cold event from 4 to 2 kyr BP, as shown by a reduction in temperature and salinity (blue coloured band; Fig. 5.5d and 5.5e) and also marked by a significant reduction of the bottom water ventilation (low $\delta^{13}C$; Fig. 5.5c). The cooling from 4 to 2 kyr BP represents the termination of mid Holocene thermal maxima. This cooling however, coincides with the end of a vast Siberian flood (5.5 kyr) and the increase in sea ice production on the Arctic shelves (Bauch et al., 2001; Werner et al., 2013). The sea ice transported via Farm Strait to the northwestern Nordic Seas probably acted as positive feedback for Neoglaciation after the mid Holocene. However, the cooling in the Lofoten Basin was delayed could be due to the slow expansion of Arctic sea ice towards the eastern Norwegian Sea (Telesinski et al., 2014, 2015). Another possibility is that the strong convection also played a role in delaying the cooling in Lofoten basin as it requires an enhanced inflow of AW. It has been recorded that there was a stepwise decrease in convection strength around 3 kyr BP (Telesinski et al., 2014). A warming trend is noticeable after 2 kyr BP and the SST reached a level comparable with mid Holocene thermal maxima. It is related to the increase in AW advection into the Nordic seas (Giraudeau et al., 2010; Olsen et al., 2012). The long-term decline in SST matches with the decrease in solar insolation at 65°N during the summer solstice (Fig. 5.5f).

5.6 Conclusions

We found that during the early phase of the last interglacial the surface was warmer and saltier, which was then interrupted by a small interval of cold and fresh surface water. During this cold event, the decline in ventilation suggests the fresh water influx could have reduced the thermohaline circulation, which thereby decreases the heat transport to the high northern latitude, and that results in a cooling event. Thereafter, the peak warmth reached and lasted up to 118 kyr BP. After the last interglacial, the beginning of the last glacial period is marked by the increase in $\delta^{18}O$ of both planktic and benthic foraminifera, a slight declining trend of SST and increase in salinity. In this glacial interval, the SST record also shows the interstadial MIS 5c. The ventilation increased during the glacial phase. Likewise the last interglacial period, the Holocene also records the effect of fresh water influx during the early Holocene. The 8.2 kyr BP cold event is also observed at the Lofoten basin (from 9.8 to 8.6 kyr BP). The enhanced fresh water influx is marked by the decrease in salinity (below the modern value), SST, and ventilation. This cold event is also recorded by the increase in $\delta^{18}O$ values of the benthic foraminifera. The mid Holocene thermal maxima reached after 8 kyr BP and lasted up to 4 kyr BP. The thermal maxima terminated by the Neoglaciation from 4 to 2 kyr BP.

Chapter 6

Conclusion and Recommendations for future work

Earth's climatic components are linked to each other via various oceanic and atmospheric teleconnection mechanisms. The South Asian monsoon, a major and unique feature of the Earth's climatic system, is important to a vast population. It varies on different time scales (from seasonal to tectonic) driven by various forcing factors. Similarly, the northern polar region (Arctic) is highly sensitive to climatic fluctuations and also affects the other parts of the earth's climate. One of the major aims of this thesis is to reconstruct the paleoenvironmental condition in the Arctic and explore its effect on the SoAM variability during the Mid Pliocene Warm Period (MPWP), the period analogous to the modern climate. The other aim is to quantify the high latitude climate (Norwegian Sea) during the last interglacial and the Holocene.

To achieve these objectives, the sediment core samples collected from different locations are analyzed for different geochemical proxies. The nitrogen isotope ($\delta^{15}N$) of the sedimentary organic matter (SOM) indicates denitrification in the eastern Arabian Sea and relative nutrient utilization in the Arctic Ocean. The elemental concentration of the organic matter such as Total Organic Carbon (TOC) and Total Nitrogen (TN) used to determine the surface productivity and its ratio reflects the provenance of the organic matter. The carbon isotope ($\delta^{13}C$) is used to determine the influence of terrestrial organic matter on the $\delta^{15}N$ value as well as the provenance of SOM. The trace element ratio (Mg/Ca) of the microfossil foraminifera are used to reconstruct the past sea surface temperature (SST) and salinity (SSS). The oxygen and carbon isotope ratios ($\delta^{18}O$ and $\delta^{13}C$) of planktic and benthic foraminifera are used to reconstruct the glacial and interglacial cycles and bottom water ventilation. The major findings of this thesis are discussed below:

6.1 Arctic climate reconstruction during late Pliocene

The late Pliocene period encompasses the MPWP, other interglacial periods as well as glacial periods with one major glaciation (MIS M2). The Arctic climate is sensitive to the presence of sea ice. The sea ice melting and the associated positive feedbacks accelerate the warming in that region. This thesis study the Arctic climate variability during a period analogous to the modern climate i.e., MPWP. The sea ice melting and the freshwater influx are studied based on the Arctic water column stratification.

The relative nutrient utilization indicates the replenishment of the nutrient at the surface, which suggests the mixing between surface water with the nutrient-rich intermediate water. The high relative nutrient utilization represents high consumption of the nutrient and low replenishment of nutrients at the surface. Thus, it suggests a strong stratification. We find that during warm periods of the late Pliocene including MPWP, the stratification is strong. While during colder periods, the stratification is weak. We suggest that during warmer periods like MPWP, the sea ice melt and high river runoff brings a high amount of freshwater to the surface that could have strengthened the Arctic stratification.

During these warmer periods, the enhancement of the North Atlantic Current to the core site is also observed by Rahaman et al., 2020. The warm North Atlantic Current could have played a major role in the sea ice melt. We find that the external forcing factor, which controls the strength of stratification and the enhancement of NAC, is predominantly the eccentricity cycle. The enhanced influx of north Atlantic current to the Arctic and the strong solar insolation together increased the sea ice melt and high river runoff, which increases the stratification.

6.2 South Asian Monsoon variability during the late Pliocene period

The South Asian Monsoon (SoAM) variability is extensively studied on different time scales though lacuna still exists during MPWP. To fill this knowledge gap, a high-resolution record of the denitrification and productivity related to SoAM variability from the eastern Arabian Sea is reconstructed during the late Pliocene including MPWP. The samples were collected during IODP expedition 355 from Site U1456. The provenance of the sedimentary organic matter is determined using TOC/TN ratio and the $\delta^{13}C$ value shows that the organic matter is mostly of marine origin. Any contribution from the terrestrial organic matter has a negligible effect on the $\delta^{15}N$ value as observed from the $\delta^{15}N$ vs $\delta^{13}C$. There is no diagenesis observed at the study site.

The high productivity and high denitrification suggest the intensification of SoAM. We find that during the late Pliocene, the surface productivity and denitrification record showed four distinct intervals viz. intervals I (2.7 - 2.9 Ma), II (2.9 - 3.05 Ma), III (3.05 - 3.2 Ma), and IV (3.2 - 3.4 Ma). The productivity and denitrification are low during intervals IV and II, which suggest weakened SoAM during these intervals. The productivity and denitrification are high during interval III (MPWP) and interval I indicating an intensified SoAM during those periods. Interval I, despite being the period pertaining to the intensification of the northern hemisphere glaciation, experiences intensified monsoon due to Indonesian Throughflow related changes.

6.3 Teleconnection between Arctic sea ice extent and SoAM variability during the Late Pliocene

The teleconnection between SoAM and the Arctic sea ice extent during the late Pliocene is established in the present study. The SoAM is reconstructed from the eastern Arabian Sea based on the denitrification and productivity record. The spring sea ice cover is constructed using the sea ice biomarker IP25 and a related open-water highly branched isoprenoid (HBI) lipid (HBI III) from the Yermak Plateau during the late Pliocene (Rahaman et al., 2020). The monsoon variability is an interplay between dynamic and thermodynamic effects. The sea ice extent variability induces a dynamic effect whereby it changes the meridional heat and mass transport and thus affects the migration of ITCZ. The enhanced sea ice extent causes an adverse dynamic effect of shifting the ITCZ southwards. The solar insolation at 15°N summer solstice also causes a dynamic effect by influencing the meridional temperature gradient and thus the cross-equatorial monsoon flow. The high (low) atmospheric pCO_2 concentration causes a thermodynamic effect by increasing (decreasing) moisture carrying capacity of winds during enhanced (reduced) warmth.

During interval IV, both the dynamical and thermodynamical effects are adverse resulting in reduced SoAM. During interval III (MPWP), the early part shows high solar insolation and high pCO2 while the spring sea ice extent is high. We find enhanced monsoon during this interval, which suggests that the thermodynamic effect and insolation-influence overcame the adverse dynamic effect of sea ice increase. However, during the later part of this interval, the reduction of sea ice mainly enhances the monsoon even though the thermodynamic effect is weakened. During interval II, the low CO_2 concentration and low solar insolation reduce the monsoon. Although a favourable dynamic effect due to less sea ice exists but the strong thermodynamic effect results in a weaker monsoon. During interval I, the enhanced monsoon is attributed to the tectonically induced reorganization of the Indonesian Through Flow (ITF). The change of ITF cools the southern tropical Indian Ocean subsurface and surface. This leads to an increase in the cross-equatorial pressure gradient and that increases the inter-hemispherical heat and moisture transport resulting in intensified SoAM. As far as the influence of Arctic sea ice extent on monsoon is concerned, we find that higher (lower) Arctic sea ice extent causes a weak (strong) monsoon.

6.4 Quantitative Climatic reconstruction at the Norwegian Sea during the last interglacial period and the Holocene

To quantify the climate in the Norwegian Sea, we have used the sediment core samples collected during the 62nd cruise of the Research Vessel AMK-5188. This sediment core is collected from the Lofoten Basin, Nordic Seas. The surface hydrography is reconstructed based on the SST and SSS. The bottom water ventilation is shown by the $\delta^{13}C$ values of the benthic foraminifera. In the early phase of the last interglacial period, the SST increased from ~3°C to 6°C and the surface salinity also increased to the modern value. It indicates the enhancement of North Atlantic water towards the Norwegian Sea after the penultimate deglaciation. This warm interval was however disrupted by the large influx of fresh water into the Nordic Seas. The freshwater influx is indicated by the reduction of surface temperature, salinity, and bottom water ventilation. The freshwater influx could have reduced the thermohaline circulation by reducing the surface density. The reduction of thermohaline circulation decreases the heat transport to the high northern latitude, and that results in a cooling event. This disruption of the warm interval sets the peak warmth (~7 °C) a little late. After the last interglacial period, the early part of the last glacial period is marked by the increase in sea surface salinity and a slight decrease in sea surface temperature. The ventilation is also high during the early phase of the last glacial period.

The Holocene, the current interglacial period, also shows the freshwater events in the Norwegian Sea. During the early phase of the Holocene, the warm and high salinity surface water gradually cools and gets fresher till 8.6 kyr BP. However, the early phase of the cooling is associated with the enhanced deglacial freshwater influx from the Greenland ice sheet. Further, the decrease in surface temperature and salinity till 8.6 kyr BP corresponds to the decrease in bottom water ventilation, suggesting its possible relation to the 8.2 kyr BP cooling event. This cold event could be related to the catastrophic freshwater release into the Labrador Sea and the disruption of NADW formation, which reduced the heat transport to higher latitudes. After this cold event, the SST increased up to ~7°C and the SSS also increased above modern value. Thus, the Holocene attains the thermal maxima at ~8 kyr BP (mid-Holocene thermal maxima). The Holocene is further disturbed by another cold event from 4 to 2 kyr BP, which is marked by a significant reduction of bottom water ventilation. This cold event is associated with the increase in sea ice expansion to the Norwegian Sea. A warming trend is noticeable after 2 kyr BP.

6.5 Recommendation for future work

The remote processes play an important role in influencing the tropical climate including the South Asian monsoon. Climate variability of northern and southern high latitudes are such processes that can influence monsoon via various oceanic and atmospheric teleconnections. Following are the recommendation for future work:

(i) *Quantitative* proxy data, in terms of exact SST and salinity, is required for a better understanding of the complex processes occurring in oceans and the atmosphere.

(ii) In addition to the proxy records, paleoclimate *models* are also necessary to understand these teleconnections.

(iii) Further, how the Arctic sea ice influences the monsoon through the Pacific Ocean and the Walker Circulation needs to be explored.

(iv) Thermohaline circulation influences the global climate and monsoon by transporting heat. Therefore, the temporal and spatial extent of it needs to be constrained using various water mass proxies like neodymium isotopes, carbon isotopes of benthic foraminifera, etc.

(v) The full temporal extent of northern and southern polar climate variability is still unexplored. So, attempts shall be made to go back much farther in time using IODB cores to cover the whole Cenozoic and study the co-evolution of monsoon and polar climate.

Bibliography

Aagaard, K., Coachman, L. K., & Carmack, E. (1981). On the halocline of the Arctic Ocean. *Deep Sea Research Part A, Oceanographic Research Papers*, *28*(6), 529–545. https://doi.org/10.1016/0198-0149(81)90115-1

Adkins, J. F., McIntyre, K., & Schrag, D. P. (2002). The salinity, temperature, and δ18O of the glacial deep ocean. *Science*. https://doi.org/10.1126/science.1076252

Agnihotri, R., Dutta, K., Bhushan, R., & Somayajulu, B. L. K. (2002). Evidence for solar forcing on the Indian monsoon during the last millennium. *Earth and Planetary Science Letters*, *198*(3–4), 521–527.

Altabet, M. A., & Francois, R. (1994). Sedimentary nitrogen isotopic ratio as a recorder for surface ocean nitrate utilization. *Global Biogeochemical Cycles*. https://doi.org/10.1029/93GB03396

Altabet, M. A., Francois, R., Murray, D. W., & Prell, W. L. (1995). Climate-related variations in denitrification in the Arabian Sea from sediment 15N/14N ratios. *Nature*, *373*(6514), 506–509.

Altabet, M. A., Higginson, M. J., & Murray, D. W. (2002). The effect of millennial-scale changes in Arabian Sea denitrification on atmospheric CO2. *Nature*, *415*(6868), 159–162.

Anand, P., Elderfield, H., & Conte, M. H. (2003). Calibration of Mg/Ca thermometry in planktonic foraminifera from a sediment trap time series. *Paleoceanography*, *18*(2)

Ashok, K., Guan, Z., & Yamagata, T. (2001). Impact of the Indian Ocean dipole on the relationship between the Indian monsoon rainfall and ENSO. *Geophysical Research Letters*, *28*(23), 4499–4502.

Ashok, K., Behera, S. K., Rao, S. A., Weng, H., & Yamagata, T. (2007). El Niño Modoki and its possible teleconnection. *Journal of Geophysical Research: Oceans*, *112*(C11).

Asmerom, Y., Polyak, V. J., & Burns, S. J. (2010). Variable winter moisture in the southwestern United States linked to rapid glacial climate shifts. *Nature Geoscience*, *3*(2), 114–117.

Barber, D. C., Dyke, A., Hillaire-Marcel, C., Jennings, A. E., Andrews, J. T., Kerwin, M. W., et al. (1999). Forcing of the cold event of 8,200 years ago by catastrophic drainage of Laurentide lakes. *Nature*, *400*(6742), 344–348. https://doi.org/10.1038/22504

Bard, E., Hamelin, B., Arnold, M., Montaggioni, L., Cabioch, G., Faure, G., &

Rougerie, F. (1996). Deglacial sea-level record from Tahiti corals and the timing of global meltwater discharge. *Nature*, *382*(6588), 241–244.

Barker, S., Greaves, M., & Elderfield, H. (2003). A study of cleaning procedures used for foraminiferal Mg/Ca paleothermometry. *Geochemistry, Geophysics, Geosystems*, *4*(9), 1–20. https://doi.org/10.1029/2003GC000559

Barker, Stephen, Diz, P., Vautravers, M. J., Pike, J., Knorr, G., Hall, I. R., & Broecker, W. S. (2009). Interhemispheric Atlantic seesaw response during the last deglaciation. *Nature*, *457*(7233), 1097–1102.

Bartoli, Gretta, Hönisch, B., & Zeebe, R. E. (2011). Atmospheric CO2 decline during the Pliocene intensification of Northern Hemisphere glaciations. *Paleoceanography*, *26*(4), 1–14. https://doi.org/10.1029/2010PA002055

Bauch, H. A., & Erlenkeuser, H. (2008). A “critical” climatic evaluation of last interglacial (MIS 5e) records from the Norwegian Sea. *Polar Research*, *27*(2), 135-151.

Bauch, H. A., Kandiano, E. S., & Helmke, J. P. (2012). Contrasting ocean changes between the subpolar and polar North Atlantic during the past 135 ka. *Geophysical Research Letters*, *39*(11), 1–7. https://doi.org/10.1029/2012GL051800

Bemis, B. E., Spero, H. J., Bijma, J., & Lea, D. W. (1998). Reevaluation of the oxygen isotopic composition of planktonic foraminifera: Experimental results and revised paleotemperature equations. *Paleoceanography*, *13*(2), 150–160.

Berends, C. J., De Boer, B., Dolan, A. M., Hill, D. J., & Van De Wal, R. S. W. (2019). Modelling ice sheet evolution and atmospheric CO 2 during the Late Pliocene. *Climate of the Past*, *15*(4), 1603–1619.

Berger, A., & Loutre, M. F. (1991). Insolation values for the climate of the last 10 million years. *Quaternary Science Reviews*. https://doi.org/10.1016/0277-3791(91)90033-Q

Beszczynska-Mller, A., Fahrbach, E., Schauer, U., & Hansen, E. (2012). Variability in Atlantic water temperature and transport at the entrance to the Arctic Ocean, 19972010. *ICES Journal of Marine Science*. https://doi.org/10.1093/icesjms/fss056

Betzler, C., Eberli, G. P., Kroon, D., Wright, J. D., Swart, P. K., Nath, B. N., et al. (2016). The abrupt onset of the modern South Asian Monsoon winds. *Scientific Reports*, *6*(1), 1–10.

Bjerknes, J. (1969). Atmospheric teleconnections from the equatorial Pacific. *Monthly Weather Review*, *97*(3), 163–172.

Blaschek, M., & Renssen, H. (2013). The Holocene thermal maximum in the Nordic Seas: the impact of Greenland Ice Sheet melt and other forcings in a coupled atmosphere–sea-ice–ocean model. *Climate of the Past*, *9*(4), 1629–

1643. https://doi.org/10.5194/cp-9-1629-2013

Blindheim, J., & Østerhus, S. (2013). The Nordic Seas, Main Oceanographic Features. *The Nordic Seas: An Integrated Perspective: Oceanography, Climatology, Biogeochemistry, and Modeling*, (June), 11–37. https://doi.org/10.1029/158GM03

Bond, G., Showers, W., Cheseby, M., Lotti, R., Almasi, P., DeMenocal, P., et al. (1997). A pervasive millennial-scale cycle in North Atlantic Holocene and glacial climates. *Science*, *278*(5341), 1257–1266.

Bond, G. C., & Lotti, R. (1995). Iceberg discharges into the North Atlantic on millennial time scales during the last glaciation. *Science*, *267*(5200), 1005–1010.

Born, A., & Levermann, A. (2010). The 8.2 ka event: Abrupt transition of the subpolar gyre toward a modern North Atlantic circulation. *Geochemistry, Geophysics, Geosystems*, *11*(6), 1–8. https://doi.org/10.1029/2009GC003024

Brodie, C. R., Casford, J. S. L., Lloyd, J. M., Leng, M. J., Heaton, T. H. E., Kendrick, C. P., & Yongqiang, Z. (2011). Evidence for bias in C/N, δ13C and δ15N values of bulk organic matter, and on environmental interpretation, from a lake sedimentary sequence by pre-analysis acid treatment methods. *Quaternary Science Reviews*, *30*(21–22), 3076–3087. https://doi.org/10.1016/j.quascirev.2011.07.003

Van Der Burgh, J., Visscher, H., Dilcher, D. L., & Kürschner, W. M. (1993). Paleoatmospheric signatures in Neogene fossil leaves. *Science*, *260*(5115), 1788–1790.

Cane, M. A., & Molnar, P. (2001). Closing of the Indonesian seaway as a precursor to east African aridification around 3-4 million years ago. *Nature*, *411*(6834), 157–162. https://doi.org/10.1038/35075500

Carmack, E., Polyakov, I., Padman, L., Fer, I., Hunke, E., Hutchings, J., et al. (2015). Toward quantifying the increasing role of oceanic heat in sea ice loss in the new arctic. *Bulletin of the American Meteorological Society*, *96*(12), 2079–2105. https://doi.org/10.1175/BAMS-D-13-00177.1

Cavalieri, D. J., & Parkinson, C. L. (2012). Arctic sea ice variability and trends, 1979-2010. *Cryosphere*, *6*(4), 881–889. https://doi.org/10.5194/tc-6-881-2012

Chatterjee, S., Ravichandran, M., Murukesh, N., Raj, R. P., & Johannessen, O. M. (2021). A possible relation between Arctic sea ice and late season Indian Summer Monsoon Rainfall extremes. *Npj Climate and Atmospheric Science*, *4*(1), 1–6. https://doi.org/10.1038/s41612-021-00191-w

Cheng, H., Edwards, R. L., Wang, Y., Kong, X., Ming, Y., Kelly, M. J., et al. (2006). A penultimate glacial monsoon record from Hulu Cave and two-phase glacial terminations. *Geology*, *34*(3), 217–220.

Clift, Peter D, Hodges, K. V, Heslop, D., Hannigan, R., Van Long, H., & Calves, G. (2008). Correlation of Himalayan exhumation rates and Asian monsoon intensity. *Nature Geoscience*, *1*(12), 875–880.

Clift, Peter Dominic, Webb, A. G., Stockli, D. F., Blusztajn, J., & Zhou, P. (2018). Climate-Tectonic Feedbacks in the Cenozoic Western Himalaya. In *AGU Fall Meeting Abstracts* (Vol. 2018, pp. PP24C-05).

Coachman, L. K., & Barnes, C. A. (1962). Surface Water in the Eurasian Basin of the Arctic Ocean. *Arctic*, *15*(4). https://doi.org/10.14430/arctic3581

Codispoti, L. A., Kelly, V., Thessen, A., Matrai, P., Suttles, S., Hill, V., et al. (2013). Synthesis of primary production in the Arctic Ocean: III. Nitrate and phosphate based estimates of net community production. *Progress in Oceanography*, *110*(December 2012), 126–150. https://doi.org/10.1016/j.pocean.2012.11.006

Cohen, J., Screen, J. A., Furtado, J. C., Barlow, M., Whittleston, D., Coumou, D., Francis, J., Dethloff, K., Entekhabi, D., & Overland, J. (2014). Recent Arctic amplification and extreme mid-latitude weather. *Nature Geoscience*, *7*(9), 627–637.

Cortijo, E., Duplessy, J. C., Labeyrie, L., Leclaire, H., Duprat, J., & Van Wearing, T. C. E. (1994). Eemian cooling in the Norwegian Sea and North Atlantic ocean preceding continental ice-sheet growth. *Nature*. https://doi.org/10.1038/372446a0

Craig, H. (1953). The geochemistry of the stable carbon isotopes. *Geochimica et Cosmochimica Acta*, *3*(2–3), 53–92.

Cronin, T. M., Whatley, R., Wood, A., Tsukagoshi, A., Ikeya, N., Brouwers, E. M., & Briggs, W. M. (1993). Microfaunal Evidence for Elevated Pliocene Temperatures in the Arctic Ocean. *Paleoceanography*. https://doi.org/10.1029/93PA00060

Crowley, T. J. (1996). Pliocene climates: the nature of the problem. *Marine Micropaleontology*, *27*(1–4), 3–12.

Curry, W. B., & Oppo, D. W. (2005). Glacial water mass geometry and the distribution of δ 13C of ΣCO2 in the western Atlantic Ocean. *Paleoceanography*, *20*(1), 1–12. https://doi.org/10.1029/2004PA001021

Dansgaard, W., Johnsen, S. J., Clausen, H. B., Dahl-Jensen, D., Gundestrup, N. S., Hammer, C. U., et al. (1993). Evidence for general instability of past climate from a 250-kyr ice-core record. *Nature*, *364*(6434), 218–220.

Dolan, A. M., Haywood, A. M., Hill, D. J., Dowsett, H. J., Hunter, S. J., Lunt, D. J., & Pickering, S. J. (2011). Sensitivity of Pliocene ice sheets to orbital forcing. *Palaeogeography, Palaeoclimatology, Palaeoecology*, *309*(1–2), 98–110.

Douville, H., & John, A. (2021). Fast adjustment versus slow SST-mediated response of daily precipitation statistics to abrupt 4xCO2. *Climate Dynamics*, *56*(3–4), 1083–1104. https://doi.org/10.1007/s00382-020-05522-w

Dowsett, H., Barron, J., & Poore, R. (1996). Middle Pliocene sea surface temperatures: A global reconstruction. *Marine Micropaleontology*. https://doi.org/10.1016/0377-8398(95)00050-X

Dowsett, Harry J., Cronin, T. M., Poore, R. Z., Thompson, R. S., Whatley, R. C., & Wood, A. M. (1992). Micropaleontological evidence for increased meridional heat transport in the North Atlantic ocean during the Pliocene. *Science*, *258*(5085), 1133–1135. https://doi.org/10.1126/science.258.5085.1133

Dowsett, H. J., Robinson, M. M., & Foley, K. M. (2009). Pliocene three-dimensional global ocean temperature reconstruction. *Climate of the Past*, *5*(4), 769-783.

Dowsett, H., Robinson, M., Haywood, A. M., Salzmann, U., Hill, D., Sohl, L. E., ... & Stoll, D. K. (2010). The PRISM3D paleoenvironmental reconstruction. *Stratigraphy*, *7*(2-3), 123-139.

Dowsett, H. J., Robinson, M. M., Haywood, A. M., Hill, D. J., Dolan, A. M., Stoll, D. K., ... & Riesselman, C. R. (2012). Assessing confidence in Pliocene sea surface temperatures to evaluate predictive models. *Nature Climate Change*, *2*(5), 365-371.

Dowsett, Harry J., Robinson, M. M., Foley, K. M., Herbert, T. D., Otto-Bliesner, B. L., & Spivey, W. (2019). The mid-Piacenzian of the North Atlantic Ocean. *Stratigraphy*, *16*(3), 119–144. https://doi.org/10.29041/strat.16.3.119-144

Dowsett, Harry J, & Cronin, T. M. (1990). High eustatic sea level during the middle Pliocene: Evidence from the southeastern US Atlantic Coastal Plain. *Geology*, *18*(5), 435–438.

Dutton, A., & Lambeck, K. (2012). Ice volume and sea level during the last interglacial. *Science*, *337*(6091), 216–219.

Dymond, J., Suess, E., & Lyle, M. (1992). Correction to "Barium in the deep-sea sediment: A geochemical proxy for paleoproductivity." *Paleoceanography*, *7*(3), 391–391. https://doi.org/10.1029/92PA01080

Elderfield, H., & Ganssen, G. (2000). Past temperature and δ18O of surface ocean waters inferred from foraminiferal Mg/Ca ratios. *Nature*, *405*(6785), 442–445.

Erez, J., & Luz, B. (1983). Experimental paleotemperature equation for planktonic foraminifera. *Geochimica et Cosmochimica Acta*, *47*(6), 1025–1031.

Fairbanks, R. G. (1989). A 17,000-year glacio-eustatic sea level record: influence of glacial melting rates on the Younger Dryas event and deep-ocean circulation. *Nature*, *342*(6250), 637–642.

Farquhar, G. D., Ehleringer, J. R., & Hubick, K. T. (1989). Carbon Isotope Discrimination and Photosynthesis. *Annual Review of Plant Physiology and Plant Molecular Biology*. https://doi.org/10.1146/annurev.pp.40.060189.002443

Findlater, J. (1981). An experiment in monitoring cross-equatorial airflow at low level over. *Monsoon Dynamics*, 309.

Fleming, K., & Lambeck, K. (2004). Constraints on the Greenland Ice Sheet since the Last Glacial Maximum from sea-level observations and glacial-rebound models. *Quaternary Science Reviews*, *23*(9–10), 1053–1077.

Fox-Kemper, B., Hewitt, H. T., Xiao, C., Aðalgeirsdóttir, G., Drijfhout, S. S., Edwards, T. L., et al. (2021). Ocean, Cryosphere and Sea Level Change. *Climate Change 2021: The Physical Science Basis. Contribution of Working Group I to the Sixth Assessment Report of the Intergovernmental Panel on Climate ChangeScience Basis. Contribution of Working Group I to the Sixth Assessment Report of the Intergover*, *2018*(August), 1–257.

Freudenthal, T., Wagner, T., Wenzhöfer, F., Zabel, M., & Wefer, G. (2001). Early diagenesis of organic matter from sediments of the Eastern subtropical Atlantic: Evidence from stable nitrogen and carbon isotopes. *Geochimica et Cosmochimica Acta*, *65*(11), 1795–1808. https://doi.org/10.1016/S0016-7037(01)00554-3

Fronval, T., Jansen, E., Haflidason, H., & Sejrup, H. P. (1998). Variability in surface and deep water conditions in the Nordic seas during the last interglacial period. *Quaternary Science Reviews*, *17*(9-10), 963-985.

Gadgil, S. (2003). The Indian monsoon and its variability. *Annual Review of Earth and Planetary Sciences*, *31*(1), 429–467.

Gadgil, S. (2018). The monsoon system: Land–sea breeze or the ITCZ? *Journal of Earth System Science*, *127*(1), 1–29.

Galaasen, E. V., Ninnemann, U. S., Irvali, N., Kleiven, H. F., Rosenthal, Y., Kissel, C., & Hodell, D. A. (2014). Rapid reductions in North Atlantic Deep Water during the peak of the last interglacial period. *Science*, *343*(6175), 1129–1132. https://doi.org/10.1126/science.1248667

Ganachaud, A., & Wunsch, C. (2000). Improved estimates of global ocean circulation, heat transport and mixing from hydrographic data. *Nature*, *408*(6811), 453–457.

Gebregiorgis, D., Hathorne, E. C., Giosan, L., Clemens, S., Nürnberg, D., & Frank, M. (2018). Southern Hemisphere forcing of South Asian monsoon precipitation over the past~ 1 million years. *Nature Communications*, *9*(1), 1–8.

Gingele, F. X., Zabel, M., Kasten, S., Bonn, W. J., & Nürnberg, C. C. (1999).

Biogenic Barium as a Proxy for Paleoproductivity: Methods and Limitations of Application. *Use of Proxies in Paleoceanography*, 345–364. https://doi.org/10.1007/978-3-642-58646-0_13

Giraudeau, J., Grelaud, M., Solignac, S., Andrews, J. T., Moros, M., & Jansen, E. (2010). Millennial-scale variability in Atlantic water advection to the Nordic Seas derived from Holocene coccolith concentration records. *Quaternary Science Reviews*, *29*(9–10), 1276–1287. https://doi.org/10.1016/j.quascirev.2010.02.014

Gleick, P. H. (2000). *The world's water 2000– 2001* (pp. 39–61). Island Press.

Goswami, B. N., & Chakravorty, S. (2017). Dynamics of the Indian summer monsoon climate. In *Oxford research encyclopedia of climate science*.

Goswami, B. N., Madhusoodanan, M. S., Neema, C. P., & Sengupta, D. (2006). A physical mechanism for North Atlantic SST influence on the Indian summer monsoon. *Geophysical Research Letters*, *33*(2), 1–4. https://doi.org/10.1029/2005GL024803

Govin, A., Braconnot, P., Capron, E., Cortijo, E., Duplessy, J. C., Jansen, E., et al. (2012). Persistent influence of ice sheet melting on high northern latitude climate during the early Last Interglacial. *Climate of the Past*, *8*(2), 483–507. https://doi.org/10.5194/cp-8-483-2012

Gradstein, F., & Ogg, J. (2004). Geologic time scale 2004–why, how, and where next! *Lethaia*, *37*(2), 175–181.

Grootes, P. M., Stuiver, M., White, J. W. C., Johnsen, S., & Jouzel, J. (1993). Comparison of oxygen isotope records from the GISP2 and GRIP Greenland ice cores. *Nature*, *366*(6455), 552–554.

Grunseich, G., & Wang, B. (2016). Arctic sea ice patterns driven by the asian summer monsoon. *Journal of Climate*, *29*(24), 9097–9112. https://doi.org/10.1175/JCLI-D-16-0207.1

Gupta, A. K., Yuvaraja, A., Prakasam, M., Clemens, S. C., & Velu, A. (2015). Evolution of the South Asian monsoon wind system since the late Middle Miocene. *Palaeogeography, Palaeoclimatology, Palaeoecology*, *438*, 160–167.

Hall, I. R., Bianchi, G. G., & Evans, J. R. (2004). Centennial to millennial scale Holocene climate-deep water linkage in the North Atlantic. *Quaternary Science Reviews*, *23*(14–15), 1529–1536. https://doi.org/10.1016/j.quascirev.2004.04.004

Han, Z., Zhang, Q., Li, Q., Feng, R., Haywood, A., Tindall, J., et al. (2021). Evaluating the large-scale hydrological cycle response within the PlioMIP2 ensemble. *Climate of The Past Discussions*, (November), 1–32. https://doi.org/10.5194/cp-2021-72

Hastenrath, S., & Lamb, P. J. (1979). Climatic Atlas of the Indian Ocean, vol. 1, Surface Climate and Atmospheric Circulation. *Madison: University of Wisconsin Press, Ll.*

Haugan, P. M. (1999). Structure and heat content of the West Spitsbergen Current. In *Polar Research*. https://doi.org/10.1111/j.1751-8369.1999.tb00291.x

Haywood, A. M., Hill, D. J., Dolan, A. M., Otto-Bliesner, B. L., Bragg, F., Chan, W. L., et al. (2013). Large-scale features of Pliocene climate: Results from the Pliocene Model Intercomparison Project. *Climate of the Past*. https://doi.org/10.5194/cp-9-191-2013

Haywood, Alan M., Tindall, J. C., Dowsett, H. J., Dolan, A. M., Foley, K. M., Hunter, S. J., et al. (2020). The Pliocene Model Intercomparison Project Phase 2: Large-scale climate features and climate sensitivity. *Climate of the Past*. https://doi.org/10.5194/cp-16-2095-2020

Haywood, A. M., Dowsett, H. J., Otto-Bliesner, B., Chandler, M. A., Dolan, A. M., Hill, D. J., ... & Sohl, L. E. (2010). Pliocene model intercomparison project (PlioMIP): experimental design and boundary conditions (experiment 1). *Geoscientific Model Development*, *3*(1), 227-242.

Haywood, Alan M, Dekens, P., Ravelo, A. C., & Williams, M. (2005). Warmer tropics during the mid‐Pliocene? Evidence from alkenone paleothermometry and a fully coupled ocean‐atmosphere GCM. *Geochemistry, Geophysics, Geosystems*, *6*(3).

Heinrich, H. (1988). Origin and consequences of cyclic ice rafting in the northeast Atlantic Ocean during the past 130,000 years. *Quaternary Research*, *29*(2), 142–152.

Hill, D. J., Dolan, A. M., Haywood, A. M., Hunter, S. J., & Stoll, D. K. (2010). Sensitivity of the Greenland Ice Sheet to Pliocene sea surface temperatures. *Stratigraphy*, *7*(2–3), 111–121.

Hoefs, J., 2009. Stable Isotope Geochemistry, sixth ed. Springer-Verlag. p. 285.

Huang, Y., Clemens, S. C., Liu, W., Wang, Y., & Prell, W. L. (2007). Large-scale hydrological change drove the late Miocene C4 plant expansion in the Himalayan foreland and Arabian Peninsula. *Geology*, *35*(6), 531–534.

Jaiser, R., Dethloff, K., Handorf, D., Rinke, A., & Cohen, J. (2012). Impact of sea ice cover changes on the Northern Hemisphere atmospheric winter circulation. *Tellus A: Dynamic Meteorology and Oceanography*, *64*(1), 11595.

Jung, S. J. A., Kroon, D., Ganssen, G., Peeters, F., & Ganeshram, R. (2009). Enhanced Arabian Sea intermediate water flow during glacial North Atlantic cold phases. *Earth and Planetary Science Letters*, *280*(1–4), 220–228. https://doi.org/10.1016/j.epsl.2009.01.037

Kapsch, M.-L., Graversen, R. G., Tjernström, M., & Bintanja, R. (2016). The effect of downwelling longwave and shortwave radiation on Arctic summer sea ice. *Journal of Climate*, *29*(3), 1143–1159.

Karas, C., Nürnberg, D., Gupta, A. K., Tiedemann, R., Mohan, K., & Bickert, T. (2009). Mid-Pliocene climate change amplified by a switch in Indonesian subsurface throughflow. *Nature Geoscience*, *2*(6), 434–438. https://doi.org/10.1038/ngeo520

Karas, C., Nürnberg, D., Tiedemann, R., & Garbe-Schönberg, D. (2011). Pliocene Indonesian Throughflow and Leeuwin Current dynamics: Implications for Indian Ocean polar heat flux. *Paleoceanography*, *26*(2), 1–9. https://doi.org/10.1029/2010PA001949

Kaspar, F., Kühl, N., Cubasch, U., & Litt, T. (2005). A model-data comparison of European temperatures in the Eemian interglacial. *Geophysical Research Letters*, *32*(11), 1–5. https://doi.org/10.1029/2005GL022456

Kathayat, G., Cheng, H., Sinha, A., Spötl, C., Edwards, R. L., Zhang, H., et al. (2016). Indian monsoon variability on millennial-orbital timescales. *Scientific Reports*, *6*(1), 1–7.

Kawamura, K., Parrenin, F., Lisiecki, L., Uemura, R., Vimeux, F., Severinghaus, J. P., et al. (2007). Northern Hemisphere forcing of climatic cycles in Antarctica over the past 360,000 years. *Nature*, *448*(7156), 912–916.

Kim, S., & Crowley, T. J. (2000). Increased Pliocene North Atlantic deep water: cause or consequence of Pliocene warming? *Paleoceanography*, *15*(4), 451–455.

Kısakürek, B., Eisenhauer, A., Böhm, F., Garbe-Schönberg, D., & Erez, J. (2008). Controls on shell Mg/Ca and Sr/Ca in cultured planktonic foraminiferan, Globigerinoides ruber (white). *Earth and Planetary Science Letters*, *273*(3–4), 260–269.

Knies, J., Matthiessen, J., Vogt, C., & Stein, R. (2002). Evidence of "Mid-Pliocene (similar to 3 Ma) global warmth" in the eastern Arctic Ocean and implications for the Svalbard/Barents Sea ice sheet during the late Pliocene and early Pleistocene (similar to 3-1.7 Ma). *Boreas*, *31*(1), 82–93. https://doi.org/10.1080/03009480210652

Knies, J., Brookes, S., & Schubert, C. J. (2007). Re-assessing the nitrogen signal in continental margin sediments: New insights from the high northern latitudes. *Earth and Planetary Science Letters*, *253*(3–4), 471–484. https://doi.org/10.1016/j.epsl.2006.11.008

Knies, J., Cabedo-Sanz, P., Belt, S. T., Baranwal, S., Fietz, S., & Rosell-Melé, A. (2014). The emergence of modern sea ice cover in the Arctic Ocean. *Nature Communications*, *5*, 1–7. https://doi.org/10.1038/ncomms6608

Kopp, R. E., Simons, F. J., Mitrovica, J. X., Maloof, A. C., & Oppenheimer, M. (2009). Probabilistic assessment of sea level during the last interglacial stage.

Nature, *462*(7275), 863–867.

Kothawale, D. R., & Kumar, K. R. (2002). Tropospheric temperature variation over India and links with the Indian summer monsoon: 1971-2000. *Mausam*, *53*(3), 289–308.

Kozdon, R., Eisenhauer, A., Weinelt, M., Meland, M. Y., & Nürnberg, D. (2009). Reassessing Mg/Ca temperature calibrations of Neogloboquadrina pachyderma (sinistral) using paired δ44/40Ca and Mg/Ca measurements. *Geochemistry, Geophysics, Geosystems*, *10*(3). https://doi.org/10.1029/2008GC002169

Krishnamurthy, L., & Krishnamurthy, V. (2016). Teleconnections of Indian monsoon rainfall with AMO and Atlantic tripole. *Climate Dynamics*, *46*(7–8), 2269–2285. https://doi.org/10.1007/s00382-015-2701-3

Krishnamurti, T. N., Krishnamurti, R., Das, S., Kumar, V., Jayakumar, A., & Simon, A. (2015). A pathway connecting the monsoonal heating to the rapid Arctic ice melt. *Journal of the Atmospheric Sciences*, *72*(1), 5–34. https://doi.org/10.1175/JAS-D-14-0004.1

Kroon, D., Steens, T., & Troelstra, S. R. (1991). 13. Onset of monsoonal related upwelling in the western arabian sea as revealed by planktonic foraminifers1. In *Proceedings of the Ocean Drilling Program, Scientific Results, College Station, TX (Ocean Drilling Program)* (Vol. 117, pp. 257–263).

Kucharski, F., Bracco, A., Yoo, J. H., & Molteni, F. (2007). Low-frequency variability of the Indian monsoon–ENSO relationship and the tropical Atlantic: The "weakening" of the 1980s and 1990s. *Journal of Climate*, *20*(16), 4255–4266.

Kumar, K. K., Rajagopalan, B., Hoerling, M., Bates, G., & Cane, M. (2006). Unraveling the mystery of Indian monsoon failure during El Niño. *Science*, *314*(5796), 115–119.

Kumar, V., Tiwari, M., Prakash, P., Mohan, R., & Thamban, M. (2021). SST Changes in the Indian Sector of the Southern Ocean and Their Teleconnection With the Indian Monsoon During the Last Glacial Period. *Paleoceanography and Paleoclimatology*, *36*(8), 1–19. https://doi.org/10.1029/2020PA004139

Kutzbach, J. E., Guetter, P. J., Ruddiman, W. F., & Prell, W. L. (1989). Sensitivity of climate to late Cenozoic uplift in southern Asia and the American west: numerical experiments. *Journal of Geophysical Research: Atmospheres*, *94*(D15), 18393–18407.

de la Vega, E., Chalk, T. B., Wilson, P. A., Bysani, R. P., & Foster, G. L. (2020). Atmospheric CO2 during the Mid-Piacenzian Warm Period and the M2 glaciation. *Scientific Reports*, *10*(1), 14–21. https://doi.org/10.1038/s41598-020-67154-8

Laskar, J., Robutel, P., Joutel, F., Gastineau, M., Correia, A. C. M., & Levrard, B.

(2004). A long-term numerical solution for the insolation quantities of the Earth. *Astronomy and Astrophysics*. https://doi.org/10.1051/0004-6361:20041335

Lawrence, K. T., Liu, Z., & Herbert, T. D. (2006). Evolution of the eastern tropical Pacific through Plio-Pleistocene glaciation. *Science*, *312*(5770), 79–83.

Lawrence, K. T., Herbert, T. D., Brown, C. M., Raymo, M. E., & Haywood, A. M. (2009). High-amplitude variations in north atlantic sea surface temperature during the early pliocene warm period. *Paleoceanography*, *24*(2), 1–15. https://doi.org/10.1029/2008PA001669

Lind, S., Ingvaldsen, R. B., & Furevik, T. (2018). Arctic warming hotspot in the northern Barents Sea linked to declining sea-ice import. *Nature Climate Change*, *8*(7), 634–639. https://doi.org/10.1038/s41558-018-0205-y

Lisiecki, L. E., & Raymo, M. E. (2005). A Pliocene-Pleistocene stack of 57 globally distributed benthic δ 18O records. *Paleoceanography*, *20*(1), 1–17. https://doi.org/10.1029/2004PA001071

Liu, J., Curry, J. A., Wang, H., Song, M., & Horton, R. M. (2012). Impact of declining Arctic sea ice on winter snowfall. *Proceedings of the National Academy of Sciences*, *109*(11), 4074–4079.

Liu, Z., & Alexander, M. (2007). Atmospheric bridge, oceanic tunnel, and global climatic teleconnections. *Reviews of Geophysics*, *45*(2).

Lourens, L., Hilgen, F., Shackleton, N. J., Laskar, J., & Wilson, J. (2012). Orbital tuning calibrations and conversions for the Neogene Period. In *A Geologic Time Scale 2004*. https://doi.org/10.1017/cbo9780511536045.026

Lunt, D. J., Foster, G. L., Haywood, A. M., & Stone, E. J. (2008). Late Pliocene Greenland glaciation controlled by a decline in atmospheric CO2 levels. *Nature*, *454*(7208), 1102–1105.

Lunt, D. J., Abe-Ouchi, A., Bakker, P., Berger, A., Braconnot, P., Charbit, S., et al. (2013). A multi-model assessment of last interglacial temperatures. *Climate of the Past*, *9*(2), 699–717.

Lourens, L. J., Sluijs, A., Kroon, D., Zachos, J. C., Thomas, E., Röhl, U., et al. (2005). Astronomical pacing of late Palaeocene to early Eocene global warming events. *Nature*, *435*(7045), 1083-1087.

Marcott, S. A., Shakun, J. D., Clark, P. U., & Mix, A. C. (2013). A reconstruction of regional and global temperature for the past 11,300 years. *Science*, *339*(6124), 1198–1201.

Massonnet, F., Fichefet, T., Goosse, H., Bitz, C. M., Philippon-Berthier, G., Holland, M. M., & Barriat, P.-Y. (2012). Constraining projections of summer Arctic sea ice. *The Cryosphere*, *6*(6), 1383–1394.

McIntyre, A., & Molfino, B. (1996). Forcing of Atlantic equatorial and subpolar millennial cycles by precession. *Science*, *274*(5294), 1867–1870.

Meyers, P. A. (1994). Preservation of elemental and isotopic source identification of sedimentary organic matter. *Chemical Geology*, *114*, 289–302. https://doi.org/10.1016/0009-2541(94)90059-0

Miller, K. G., Wright, J. D., Browning, J. V., Kulpecz, A., Kominz, M., Naish, T. R., et al. (2012). High tide of the warm pliocene: Implications of global sea level for Antarctic deglaciation. *Geology*. https://doi.org/10.1130/G32869.1

Milne, G. A., Long, A. J., & Bassett, S. E. (2005). Modelling Holocene relative sea-level observations from the Caribbean and South America. *Quaternary Science Reviews*, *24*(10–11), 1183–1202.

Molfino, B., & McIntyre, A. (1990). Precessional forcing of nutricline dynamics in the equatorial Atlantic. *Science*, *249*(4970), 766–769.

Molnar, P., Boos, W. R., & Battisti, D. S. (2010). Orographic controls on climate and paleoclimate of Asia: Thermal and mechanical roles for the Tibetan Plateau. *Annual Review of Earth and Planetary Sciences*, *38*, 77–102.

Moran, K., Backman, J., Brinkhuis, H., Clemens, S. C., Cronin, T., Dickens, G. R., et al. (2006). The cenozoic palaeoenvironment of the arctic ocean. *Nature*, *441*(7093), 601–605.

Mulitza, S., Boltovskoy, D., Donner, B., Meggers, H., Paul, A., & Wefer, G. (2003). Temperature: δ18O relationships of planktonic foraminifera collected from surface waters. *Palaeogeography, Palaeoclimatology, Palaeoecology*, *202*(1–2), 143–152. https://doi.org/10.1016/S0031-0182(03)00633-3

Myhre, A. M., Thiede, J., & Firth, J. V. (1995). Shipboard Scientific Party HOLE 910A Physiography , Plate Tectonic , and Volcanic History of Yermak Plateau. *Proceedings of the Ocean Drilling Program, Initial Reports*, *151*, 221–270.

Naafs, B. D. A., Stein, R., Hefter, J., Khélifi, N., De Schepper, S., & Haug, G. H. (2010). Late Pliocene changes in the North Atlantic Current. *Earth and Planetary Science Letters*, *298*(3–4), 434–442. https://doi.org/10.1016/j.epsl.2010.08.023

Naish, T., Powell, R., Levy, R., Wilson, G., Scherer, R., Talarico, F., et al. (2009). Obliquity-paced Pliocene West Antarctic ice sheet oscillations. *Nature*, *458*(7236), 322–328.

Naqvi, S. W. A. (1994). Denitrification processes in the Arabian Sea. *Proceedings of the Indian Academy of Sciences - Earth and Planetary Sciences*, *103*(2), 279–300. https://doi.org/10.1007/BF02839539

Nummelin, A., Ilicak, M., Li, C., & Smedsrud, L. H. (2016). Consequences of future increased Arctic runoff on Arctic Ocean stratification, circulation, and sea ice cover. *Journal of Geophysical Research: Oceans*.

https://doi.org/10.1002/2015JC011156

Nürnberg, D., Bijma, J., & Hemleben, C. (1996). Assessing the reliability of magnesium in foraminiferal calcite as a proxy for water mass temperatures. *Geochimica et Cosmochimica Acta*, *60*(5), 803–814.

Olsen, J., Anderson, N. J., & Knudsen, M. F. (2012). Variability of the North Atlantic Oscillation over the past 5,200 years. *Nature Geoscience*, *5*(11), 808–812. https://doi.org/10.1038/ngeo1589

Onarheim, I. H., Smedsrud, L. H., Ingvaldsen, R. B., & Nilsen, F. (2014). Loss of sea ice during winter north of Svalbard. *Tellus, Series A: Dynamic Meteorology and Oceanography*, *66*(1). https://doi.org/10.3402/tellusa.v66.23933

Otto-Bliesner, B. L., Brady, E. C., Clauzet, G., Tomas, R., Levis, S., & Kothavala, Z. (2006). Last glacial maximum and Holocene climate in CCSM3. *Journal of Climate*, *19*(11), 2526–2544.

Otto-Bliesner, B. L., Marshall, S. J., Overpeck, J. T., Miller, G. H., & Hu, A. (2006). Simulating arctic climate warmth and icefield retreat in the last interglaciation. *Science*, *311*(5768), 1751–1753. https://doi.org/10.1126/science.1120808

Otto-Bliesner, B. L., Brady, E. C., Fasullo, J., Jahn, A., Landrum, L., Stevenson, S., et al. (2016). Climate variability and change since 850 CE: An ensemble approach with the Community Earth System Model. *Bulletin of the American Meteorological Society*, *97*(5), 735–754.

Otto-Bliesner, B. L., Jahn, A., Feng, R., Brady, E. C., Hu, A., & Löfverström, M. (2017). Amplified North Atlantic warming in the late Pliocene by changes in Arctic gateways. *Geophysical Research Letters*. https://doi.org/10.1002/2016GL071805

Overland, J. E., & Wang, M. (2007). Future regional Arctic sea ice declines. *Geophysical Research Letters*, *34*(17).

Overland, J. E., & Wang, M. (2013). When will the summer Arctic be nearly sea ice free? *Geophysical Research Letters*, *40*(10), 2097–2101.

Pandey, D. K., Clift, P. D., Kulhanek, D. K., Andò, S., Bendle, J. A. P., Bratenkov, S., et al. (2016). Expedition 355 summary, *355*(August). https://doi.org/10.14379/iodp.proc.355.101.2016

Pant, G. B., & Parthasarathy, S. B. (1981). Some aspects of an association between the southern oscillation and Indian summer monsoon. *Archives for Meteorology, Geophysics, and Bioclimatology, Series B*, *29*(3), 245–252.

Peralta-Ferriz, C., & Woodgate, R. A. (2015). Seasonal and interannual variability of pan-Arctic surface mixed layer properties from 1979 to 2012 from hydrographic data, and the dominance of stratification for multiyear mixed layer depth shoaling. *Progress in Oceanography*.

https://doi.org/10.1016/j.pocean.2014.12.005

Perovich, D. K., Richter-Menge, J. A., Jones, K. F., Light, B., Elder, B. C., Polashenski, C., et al. (2011). Arctic sea-ice melt in 2008 and the role of solar heating. *Annals of Glaciology*, *52*(57 PART 2), 355–359. https://doi.org/10.3189/172756411795931714

Petit, J.-R., Jouzel, J., Raynaud, D., Barkov, N. I., Barnola, J.-M., Basile, I., et al. (1999). Climate and atmospheric history of the past 420,000 years from the Vostok ice core, Antarctica. *Nature*, *399*(6735), 429–436.

Philander, S. G. H., Gu, D., Lambert, G., Li, T., Halpern, D., Lau, N. C., & Pacanowski, R. C. (1996). Why the ITCZ is mostly north of the equator. *Journal of Climate*, *9*(12), 2958–2972.

Pichevin, L., Bard, E., Martinez, P., & Billy, I. (2007). Evidence of ventilation changes in the Arabian Sea during the late Quaternary: Implication for denitrification and nitrous oxide emission. *Global Biogeochemical Cycles*, 21(4).

Pnyushkov, A. V., Polyakov, I. V., Ivanov, V. V., Aksenov, Y., Coward, A. C., Janout, M., & Rabe, B. (2015). Structure and variability of the boundary current in the Eurasian Basin of the Arctic Ocean. *Deep-Sea Research Part I: Oceanographic Research Papers*. https://doi.org/10.1016/j.dsr.2015.03.001

Pollard, D., & DeConto, R. M. (2009). Modelling West Antarctic ice sheet growth and collapse through the past five million years. *Nature*, *458*(7236), 329–332.

Polyak, L., Alley, R. B., Andrews, J. T., Brigham-Grette, J., Cronin, T. M., Darby, D. A., et al. (2010). History of sea ice in the Arctic. *Quaternary Science Reviews*, *29*(15–16), 1757–1778.

Polyakov, I. V., Pnyushkov, A. V., Alkire, M. B., Ashik, I. M., Baumann, T. M., Carmack, E. C., et al. (2017). Greater role for Atlantic inflows on sea-ice loss in the Eurasian Basin of the Arctic Ocean. *Science*, *356*(6335), 285–291. https://doi.org/10.1126/science.aai8204

Prell, W. L., & Kutzbach, J. E. (1997). The impact of Tibet-Himalayan elevation on the sensitivity of the monsoon climate system to changes in solar radiation. In *Tectonic uplift and climate change* (pp. 171–201). Springer.

Premuzic, E. T., Benkovitz, C. M., Gaffney, J. S., & Walsh, J. J. (1982). The nature and distribution of organic matter in the surface sediments of world oceans and seas. *Organic Geochemistry*, *4*(2), 63–77.

Prescott, C. L., Haywood, A. M., Dolan, A. M., Hunter, S. J., & Tindall, J. C. (2019). Indian monsoon variability in response to orbital forcing during the late Pliocene. *Global and Planetary Change*, *173*(December 2018), 33–46. https://doi.org/10.1016/j.gloplacha.2018.12.002

Quade, J., Cerling, T. E., & Bowman, J. R. (1989). Development of Asian monsoon revealed by marked ecological shift during the latest Miocene in northern Pakistan. *Nature*, *342*(6246), 163–166.

Rahaman, W., Smik, L., Köseoğlu, D., N, L., Tarique, M., Thamban, M., et al. (2020). Reduced Arctic sea ice extent during the mid-Pliocene Warm Period concurrent with increased Atlantic-climate regime. *Earth and Planetary Science Letters*, *550*. https://doi.org/10.1016/j.epsl.2020.116535

Ramage CS (1971): Monsoon Meteorology. Int. Geophys. Ser., San Diego, CA: Academic, 15, pp. 296.

Randelhoff, A., Sundfjord, A., & Reigstad, M. (2015). Seasonal variability and fluxes of nitrate in the surface waters over the Arctic shelf slope. *Geophysical Research Letters*, *42*(9), 3442–3449. https://doi.org/10.1002/2015GL063655

Rao, Y. P. (1976). Southwest Monsoon. Meteor. Monogr. *Synoptic Meteorology*, *1*, 1976.

Rasmusson, E. M., & Carpenter, T. H. (1983). The relationship between eastern equatorial Pacific sea surface temperatures and rainfall over India and Sri Lanka. *Monthly Weather Review*, *111*(3), 517–528.

Ravelo, A. C., & Andreasen, D. H. (2000). Enhanced circulation during a warm period. *Geophysical Research Letters*, *27*(7), 1001–1004. https://doi.org/10.1029/1999GL007000

Raymo, M E, Grant, B., Horowitz, M., & Rau, G. H. (1996). Mid-Pliocene warmth: stronger greenhouse and stronger conveyor. *Marine Micropaleontology*, *27*(1–4), 313–326.

Raymo, Maurenn E. (1994). The initiation of Northern Hemisphere glaciation. *Annual Review of Earth and Planetary Sciences*, *22*(1), 353–383.

Rea, D. K. (1994). The paleoclimatic record provided by eolian deposition in the deep sea: The geologic history of wind. *Reviews of Geophysics*, *32*(2), 159–195.

Redfield, Alfred C. (1958). The biological control of chemical factors in the environment. *American Scientist*, *46*(3), 230A–221.

Redfield, Alfred Clarence. (1934). *On the proportions of organic derivatives in sea water and their relation to the composition of plankton* (Vol. 1). university press of liverpool Liverpool.

Regenberg, M., Steph, S., Nürnberg, D., Tiedemann, R., & Garbe-Schönberg, D. (2009). Calibrating Mg/Ca ratios of multiple planktonic foraminiferal species with δ18O-calcification temperatures: Paleothermometry for the upper water column. *Earth and Planetary Science Letters*, *278*(3–4), 324–336.

Rennermalm, A. K., Wood, E. F., Weaver, A. J., Eby, M., & Déry, S. J. (2007). Relative sensitivity of the Atlantic meridional overturning circulation to river discharge into Hudson Bay and the Arctic Ocean. *Journal of Geophysical Research: Biogeosciences*, *112*(4), 1–12. https://doi.org/10.1029/2006JG000330

Risebrobakken, B., Dokken, T., & Jansen, E. (2005). Extent and variability of the meridional atlantic circulation in the eastern nordic seas during marine isotope stage 5 and its influence on the inception of the last glacial. *Geophysical Monograph Series*, *158*, 323–339. https://doi.org/10.1029/158GM20

Robertson, A., & Vitart, F. (2018). *Sub-seasonal to seasonal prediction: the gap between weather and climate forecasting*. Elsevier.

Robinson, M. M. (2009). New quantitative evidence of extreme warmth in the Pliocene Arctic. *Stratigraphy*, *6*(4), 265–276.

Robinson, R. S., Kienast, M., Luiza Albuquerque, A., Altabet, M., Contreras, S., De Pol Holz, R., et al. (2012). A review of nitrogen isotopic alteration in marine sediments. *Paleoceanography*, *27*(4). https://doi.org/10.1029/2012PA002321

Rohling, E. J., Foster, G. L., Grant, K. M., Marino, G., Roberts, A. P., Tamisiea, M. E., & Williams, F. (2014). Sea-level and deep-sea-temperature variability over the past 5.3 million years. *Nature*. https://doi.org/10.1038/nature13230

Rohling, E. J., & Pälike, H. (2005). Centennial-scale climate cooling with a sudden cold event around 8,200 years ago. *nature*, *434*(7036), 975-979.

Routledge, C. M., Kulhanek, D. K., Tauxe, L., Scardia, G., Singh, A. D., Steinke, S., et al. (2019). A revised chronostratigraphic framework for International Ocean Discovery Program Expedition 355 sites in Laxmi Basin, eastern Arabian Sea. *Geological Magazine*. https://doi.org/10.1017/S0016756819000104

Rovere, A., Raymo, M. E., Vacchi, M., Lorscheid, T., Stocchi, P., Gomez-Pujol, L., et al. (2016). The analysis of Last Interglacial (MIS 5e) relative sea-level indicators: Reconstructing sea-level in a warmer world. *Earth-Science Reviews*, *159*, 404–427.

Roxy, M. K., Ritika, K., Terray, P., Murtugudde, R., Ashok, K., & Goswami, B. N. (2015). Drying of Indian subcontinent by rapid Indian ocean warming and a weakening land-sea thermal gradient. *Nature Communications*, *6*(May). https://doi.org/10.1038/ncomms8423

Ruddiman, W F, Prell, W. L., & Raymo, M. E. (1989). Late Cenozoic uplift in southern Asia and the American West: Rationale for general circulation modeling experiments. *Journal of Geophysical Research: Atmospheres*, *94*(D15), 18379–18391.

Ruddiman, W. F., & Kutzbach, J. E. (1989). Forcing of late Cenozoic northern hemisphere climate by plateau uplift in southern Asia and the American West. *Journal of Geophysical Research: Atmospheres*, *94*(D15), 18409–

18427.

Rudels, Bert. (2015). Arctic Ocean circulation, processes and water masses: A description of observations and ideas with focus on the period prior to the International Polar Year 2007-2009. *Progress in Oceanography*, *132*, 22–67. https://doi.org/10.1016/j.pocean.2013.11.006

Rudels, Burt, Larsson, A., Sehlstedt, P., Larsson, B. R. A., & Sehlstedt, P. (1991). Stratification and water mass formation in the Arctic Ocean : some implications for the nutrient distribution Stratification and water mass formation in the Arctic Ocean : some implications for the nutrient distribution. *Polar Research*, *10*(1), 19–32. https://doi.org/10.3402/polar.v10i1.6724

Ruttenberg, K. C., & Goñi, M. A. (1997). Phosphorus distribution, C:N:P ratios, and δ13C(OC) in arctic, temperate, and tropical coastal sediments: Tools for characterizing bulk sedimentary organic matter. *Marine Geology*, *139*(1–4), 123–145. https://doi.org/10.1016/S0025-3227(96)00107-7

Sarathchandraprasad, T., Tiwari, M., & Behera, P. (2021). South Asian Summer Monsoon precipitation variability during late Pliocene: Role of Indonesian Throughflow. *Palaeogeography, Palaeoclimatology, Palaeoecology*, *574*, 110447. https://doi.org/https://doi.org/10.1016/j.palaeo.2021.110447

Sato, T., & Kameo, K. (1996). Pliocene to Quaternary Calcareous Nannofossil Biostratigraphy of the Arctic Ocean, with Reference to Late Pliocene Glaciation. In *Proceedings of the Ocean Drilling Program, 151 Scientific Results*. https://doi.org/10.2973/odp.proc.sr.151.112.1996

De Schepper, S., Groeneveld, J., Naafs, B. D. A., Van Renterghem, C., Hennissen, J., Head, M. J., et al. (2013). Northern Hemisphere Glaciation during the globally warm early late Pliocene. *PLoS ONE*, *8*(12). https://doi.org/10.1371/journal.pone.0081508

Schneider, S. H., & Dickinson, R. E. (1974). Climate modeling. *Reviews of Geophysics*, *12*(3), 447–493.

Schneider, T., Bischoff, T., & Haug, G. H. (2014). Migrations and dynamics of the intertropical convergence zone. *Nature*, *513*(7516), 45–53. https://doi.org/10.1038/nature13636

Schubert, C. J., & Calvert, S. E. (2001). Nitrogen and carbon isotopic composition of marine and terrestrial organic matter in Arctic Ocean sediments: Implications for nutrient utilization and organic matter composition. *Deep-Sea Research Part I: Oceanographic Research Papers*, *48*(3), 789–810. https://doi.org/10.1016/S0967-0637(00)00069-8

Schubert, C. J., Stein, R., & Calvert, S. E. (2001). Tracking nutrient and productivity variations over the last deglaciation in the Arctic Ocean. *Paleoceanography*, *16*(2), 199–211. https://doi.org/10.1029/2000PA000503

Schulz, H., von Rad, U., & Erlenkeuser, H. (1998). Correlation between Arabian

Sea and Greenland climate oscillations of the past 110,000 years. *Nature*, *393*(6680), 54–57.

Seidenkrantz, M. S., Ebbesen, H., Aagaard-Sørensen, S., Moros, M., Lloyd, J. M., Olsen, J., et al. (2013). Early Holocene large-scale meltwater discharge from Greenland documented by foraminifera and sediment parameters. *Palaeogeography, Palaeoclimatology, Palaeoecology*, *391*, 71–81. https://doi.org/10.1016/j.palaeo.2012.04.006

Seki, O., Foster, G. L., Schmidt, D. N., Mackensen, A., Kawamura, K., & Pancost, R. D. (2010). Alkenone and boron-based Pliocene pCO2 records. *Earth and Planetary Science Letters*. https://doi.org/10.1016/j.epsl.2010.01.037

Serreze, M. C., & Barry, R. G. (2011). Processes and impacts of Arctic amplification: A research synthesis. *Global and Planetary Change*, *77*(1–2), 85–96. https://doi.org/10.1016/j.gloplacha.2011.03.004

Sévellec, F., Fedorov, A. V., & Liu, W. (2017). Arctic sea-ice decline weakens the Atlantic Meridional Overturning Circulation. *Nature Climate Change*. https://doi.org/10.1038/NCLIMATE3353

Shackleton, N. J. (1974). Attainment of isotopic equilibrium between ocean water and the benthonic foraminifera genus Uvigerina: isotopic changes in the ocean during the last glacial.

Sigman, D., Karsh, K., & Casciotti, K. (2009). Ocean Process Tracers: Nitrogen Isotopes in the Ocean. *Encyclopedia of Ocean Sciences*. https://doi.org/10.1006/rwos.2001.0172

Sigman, D. M., & Boyle, E. A. (2000). Glacial/interglacial variations in atmospheric carbon dioxide. *Nature*, *407*(6806), 859–869.

Singh, A. D., Jung, S. J. A., Darling, K., Ganeshram, R., Ivanochko, T., & Kroon, D. (2011). Productivity collapses in the Arabian Sea during glacial cold phases. *Paleoceanography*, *26*(3).

Smik, L., Cabedo-Sanz, P., & Belt, S. T. (2016). Semi-quantitative estimates of paleo Arctic sea ice concentration based on source-specific highly branched isoprenoid alkenes: A further development of the PIP25 index. *Organic Geochemistry*, *92*, 63–69. https://doi.org/10.1016/j.orggeochem.2015.12.007

Smith, D. E., Harrison, S., Firth, C. R., & Jordan, J. T. (2011). The early Holocene sea level rise. *Quaternary Science Reviews*, *30*(15–16), 1846–1860.

Spratt, R. M., & Lisiecki, L. E. (2016). A Late Pleistocene sea level stack. *Climate of the Past*, *12*(4), 1079–1092. https://doi.org/10.5194/cp-12-1079-2016

Srivastava, A. K., Rajeevan, M., & Kulkarni, R. (2002). Teleconnection of OLR and SST anomalies over Atlantic Ocean with Indian summer monsoon.

Geophysical Research Letters, *29*(8), 121–125.

Stan, C., Straus, D. M., Frederiksen, J. S., Lin, H., Maloney, E. D., & Schumacher, C. (2017). Review of tropical-extratropical teleconnections on intraseasonal time scales. *Reviews of Geophysics*, *55*(4), 902–937.

de Steur, L., Hansen, E., Gerdes, R., Karcher, M., Fahrbach, E., & Holfort, J. (2009). Freshwater fluxes in the East Greenland Current: A decade of observations. *Geophysical Research Letters*. https://doi.org/10.1029/2009GL041278

Stroeve, J. C., Maslanik, J., Serreze, M. C., Rigor, I., Meier, W., & Fowler, C. (2011). Sea ice response to an extreme negative phase of the Arctic Oscillation during winter 2009/2010. *Geophysical Research Letters*, *38*(2).

Stuiver, M., & Reimer, P. J. (1993). Extended ^{14}C data base and revised Calib 3.0 ^{14}C age calibration program. *Radiocarbon*, *35*(1), 215–230.

Suthhof, A., Ittekkot, V., & Gaye-Haake, B. (2001). Millenial-scale oscillation of denitrification intensity in the Arabian Sea during late Quaternary and its potential influence on atmospheric N2O and global climate. *Global Biogeochemical Cycles*, *15*(3), 637–649. https://doi.org/10.1029/2000GB001337

Swift, J. H. (1986). The Arctic Waters. *The Nordic Seas*, 129–154. https://doi.org/10.1007/978-1-4615-8035-5_5

Tan, N., Ramstein, G., Dumas, C., Contoux, C., Ladant, J. B., Sepulchre, P., et al. (2017). Exploring the MIS M2 glaciation occurring during a warm and high atmospheric CO2 Pliocene background climate. *Earth and Planetary Science Letters*, *472*, 266–276. https://doi.org/10.1016/j.epsl.2017.04.050

Telesiński, M. M., Bauch, H. A., Spielhagen, R. F., & Kandiano, E. S. (2015). Evolution of the central Nordic Seas over the last 20 thousand years. *Quaternary Science Reviews*, *121*, 98–109. https://doi.org/10.1016/j.quascirev.2015.05.013

Thibodeau, B., Bauch, H. A., & Pedersen, T. F. (2017). Stratification-induced variations in nutrient utilization in the Polar North Atlantic during past interglacials. *Earth and Planetary Science Letters*, *457*, 127–135. https://doi.org/10.1016/j.epsl.2016.09.060

Thirumalai, K., Quinn, T. M., & Marino, G. (2016). Constraining past seawater δ18O and temperature records developed from foraminiferal geochemistry. *Paleoceanography*, *31*(10), 1409–1422. https://doi.org/10.1002/2016PA002970

Thomson, J. R., Holden, P. B., Anand, P., Edwards, N. R., Porchier, C. A., & Harris, N. B. W. (2021). Tectonic and climatic drivers of Asian monsoon evolution. *Nature Communications*, *12*(1), 1–10.

Tiwari, M., Ramesh, R., Yadava, M. G., Somayajulu, B. L. K., Jull, A. J. T., & Burr, G. S. (2006). Is there a persistent control of monsoon winds by precipitation during the late Holocene? *Geochemistry, Geophysics, Geosystems*, *7*(3), 1–7. https://doi.org/10.1029/2005GC001095

Tiwari, M., Nagoji, S. S., & Ganeshram, R. S. (2015). Multi-centennial scale SST and Indian summer monsoon precipitation variability since the mid-Holocene and its nonlinear response to solar activity. *The Holocene*, *25*(9), 1415–1424.

Tiwari, M., Kumar, V., Nagoji, S., & Mohan, R. (2021). A 145 kyr record of upstream changes in Indian monsoon circulation and its link to southern high-latitude climate. *Polar Science*, *30*(September), 100739. https://doi.org/10.1016/j.polar.2021.100739

Torres-Valdés, S., Tsubouchi, T., Bacon, S., Naveira-Garabato, A. C., Sanders, R., McLaughlin, F. A., et al. (2013). Export of nutrients from the Arctic Ocean. *Journal of Geophysical Research: Oceans*, *118*(4), 1625–1644. https://doi.org/10.1002/jgrc.20063

Tripathi, S., Tiwari, M., Lee, J., Khim, B. K., Pandey, D. K., Clift, P. D., et al. (2017). First evidence of denitrification vis-à-vis monsoon in the Arabian Sea since Late Miocene. *Scientific Reports*, *7*, 1–7. https://doi.org/10.1038/srep43056

Turney, C. S. M., & Jones, R. T. (2010). Does the Agulhas Current amplify global temperatures during super‐interglacials? *Journal of Quaternary Science*, *25*(6), 839–843.

Vidya, P. J., Ravichandran, M., Subeesh, M. P., Chatterjee, S., & Nuncio, M. (2020). Author Correction: Global warming hiatus contributed weakening of the Mascarene High in the Southern Indian Ocean (Scientific Reports, (2020), 10, 1, (3255), 10.1038/s41598-020-59964-7). *Scientific Reports*, *10*(1), 16–19. https://doi.org/10.1038/s41598-020-62006-x

Vihma, T. (2014). Effects of Arctic sea ice decline on weather and climate: A review. *Surveys in Geophysics*, *35*(5), 1175–1214.

Waliser, D. E., & Gautier, C. (1993). A satellite-derived climatology of the ITCZ. *Journal of Climate*, *6*(11), 2162–2174.

Walker, J. M., Bordoni, S., & Schneider, T. (2015). Interannual variability in the large-scale dynamics of the South Asian summer monsoon. *Journal of Climate*, *28*(9), 3731–3750.

Wang, M., & Overland, J. E. (2009). A sea ice free summer Arctic within 30 years? *Geophysical Research Letters*, *36*(7), 2–6. https://doi.org/10.1029/2009GL037820

Wang, Y.-J., Cheng, H., Edwards, R. L., An, Z. S., Wu, J. Y., Shen, C.-C., & Dorale, J. A. (2001). A high-resolution absolute-dated late Pleistocene monsoon record from Hulu Cave, China. *Science*, *294*(5550), 2345–2348.

Wang, Y., Cheng, H., Edwards, R. L., Kong, X., Shao, X., Chen, S., et al. (2008). Millennial-and orbital-scale changes in the East Asian monsoon over the past 224,000 years. *Nature*, *451*(7182), 1090–1093.

Wara, M. W., Ravelo, A. C., & Delaney, M. L. (2005). Permanent El Niño-like conditions during the Pliocene warm period. *Science*, *309*(5735), 758–761.

Webster PJ (1987). The elementary monsoon. In Monsoons, Ed. JS Fein, PL Stephens, New York: Wiley, pp. 3-32.

Werner, K., Spielhagen, R. F., Bauch, D., Hass, H. C., & Kandiano, E. (2013). Atlantic Water advection versus sea-ice advances in the eastern Fram Strait during the last 9 ka: Multiproxy evidence for a two-phase Holocene. *Paleoceanography*, *28*(2), 283–295. https://doi.org/10.1002/palo.20028

Zhang, Y. G., Ji, J., Balsam, W., Liu, L., & Chen, J. (2009). Mid-Pliocene Asian monsoon intensification and the onset of Northern Hemisphere glaciation. *Geology*, *37*(7), 599–602. https://doi.org/10.1130/G25670A.1

Zhang, Z., Li, X., Guo, C., Otterå, O. H., Nisancioglu, K., Tan, N., et al. (2020). Mid-Pliocene Atlantic Meridional Overturning Circulation simulated in PlioMIP2. *Climate of the Past Discussions*. https://doi.org/10.5194/cp-2020-120

Ziegler, M., Tuenter, E., & Lourens, L. J. (2010). The precession phase of the boreal summer monsoon as viewed from the eastern Mediterranean (ODP Site 968). *Quaternary Science Reviews*, *29*(11-12), 1481-1490.